

Copyright
by
Alexander James Carpenter
2012

**The Dissertation Committee for Alexander James Carpenter Certifies that this is
the approved version of the following dissertation:**

**Physics-Based Material Constitutive Models for the Simulation of High-
Temperature Forming of Magnesium Alloy AZ31**

Committee:

Eric M. Taleff, Supervisor

David L. Bourell

Desiderio Kovar

Carolyn C. Seepersad

Michael D. Engelhardt

**Physics-Based Material Constitutive Models for the Simulation of High-
Temperature Forming of Magnesium Alloy AZ31**

by

Alexander James Carpenter, B.S.M.E., M.S.E.

Dissertation

Presented to the Faculty of the Graduate School of

The University of Texas at Austin

in Partial Fulfillment

of the Requirements

for the Degree of

Doctor of Philosophy

The University of Texas at Austin

August 2012

Dedication

To my wife

Stacey Lynn Carpenter

And our unborn child

As we move forward with our lives

Acknowledgements

I would like to thank my advisor, Dr. Eric M. Taleff, for his guidance and support during my graduate studies. I have learned a lot from him, and I hope that his teachings are evident in the quality of this dissertation.

I would like to acknowledge General Motors Research & Development, especially Jon T. Carter and Louis G. Hector, Jr., and the Texas Advanced Research Program for their financial and technical support.

I would also like to thank Aravindhya Antoniswamy for providing me with additional gas-pressure bulge test data from the General Motors apparatus. His contributions provided an additional rigorous test of my material constitutive models, and I wish him luck in his studies of high-temperature magnesium forming.

Finally, I would like to acknowledge my fellow research group members, including Jakub Jodlowski, Nicholas Pedrazas, Daniel Worthington, John Lee, Philip Noell, and Trevor Watt. I have become friends with each of you, and I wish you all the best in your future endeavors.

Physics-Based Material Constitutive Models for the Simulation of High-Temperature Forming of Magnesium Alloy AZ31

Alexander James Carpenter, Ph.D.

The University of Texas at Austin, 2012

Supervisor: Eric M. Taleff

Magnesium sheet alloys, such as wrought AZ31, have material properties that make them an attractive option for use in automotive and aircraft components. However, the low ductility of magnesium alloys at room temperature necessitates the use of high-temperature forming to manufacture complex components. Finite-element-method (FEM) simulations can assist in determining the optimum processing parameters for high-temperature forming, but only if an accurate material constitutive model is used. New material constitutive models describing the deformation behavior of AZ31 sheet at 450°C are proposed. These models account for both active deformation mechanisms at this temperature: grain-boundary-sliding creep and five-power dislocation-climb creep. Phenomena affecting these deformation mechanisms, such as material anisotropy and grain growth, are also investigated. This physics-based approach represents an improvement over previous material models, which require nonphysical parameters and can only predict forming for a limited range of conditions. Tensile tests are conducted to obtain data used in fitting constitutive models. New models are used in FEM simulations of both tensile tests and biaxial gas-pressure bulge tests. Simulation results are compared to experimental data for validation and determination of model accuracy.

Table of Contents

List of Tables	x
List of Figures	xiv
Chapter 1: Introduction	1
Chapter 2: Literature Review	4
2.1. Advantages of Magnesium Alloys	4
2.2. High-Temperature Forming	7
2.3. Material Constitutive Models	12
Chapter 3: Objectives and Methodology	23
3.1. Research Objectives	23
3.2. General Methodology	24
Chapter 4: Experimental Procedures	29
4.1. Material Description	29
4.2. Tensile Tests	30
4.2.1. Tensile Test Procedure	30
4.2.2. Tensile Specimen Measurements	33
4.3. Gas-Pressure Bulge Tests	37
4.3.1. The University of Texas Bulge Test Procedure	37
4.3.2. General Motors Bulge Test Procedure	40
Chapter 5: Static and Dynamic Grain Growth	42
5.1. Grain Growth Laws	42
5.1.1. Static Grain Growth	42
5.1.2. Dynamic Grain Growth	43
5.2. Grain Size Measurements	45
5.2.1. Summary of Results	45
5.2.2. Static Grain Growth	47
5.2.3. Dynamic Grain Growth	50

5.3. A Grain-Size Dependent Material Model	54
Chapter 6: Plastic Anisotropy	60
6.1. Two-Mechanism Theory	60
6.2. Experimental R-value Measurements	62
6.3. Effects of Anisotropy and Stress State on Deformation	68
6.4. An Anisotropic Modification to the GDTD and SDTD Models	72
6.5. Anisotropy and Crystallographic Texture	73
Chapter 7: Finite-Element-Method Simulations	76
7.1. User-Defined Functions	76
7.2. Simulation Descriptions	77
7.2.1. Tensile Simulations	77
7.2.2. Biaxial Bulge Forming Simulations	79
Chapter 8: Results and Discussion	82
8.1. Measures of Error	82
8.2. Variability and Repeatability	84
8.2. Tensile Results	89
8.2.1. True Stress-True Strain Curves	89
8.2.2. R-value Data	92
8.3. Biaxial Bulge Forming Results	94
8.3.1. University of Texas Geometry	94
8.3.2. General Motors Geometry	97
8.3.3. Effects of Preheat Time	100
8.3.4. Effects of Initial Grain Size	104
Chapter 9: Conclusions and Future Work	108
9.1. Conclusions	108
9.2. Future Work	110

Appendix A: Effects of Specimen Geometry on R-value.....	113
Appendix B: User-Defined Code for Material Constitutive Models	116
GDTDAM Material Constitutive Model	116
SDTDAM Material Constitutive Model	120
Appendix C: Abaqus Input Files.....	125
Example Tensile Input File	125
Example University of Texas Bulge Forming Input File.....	135
Example General Motors Bulge Forming Input File	141
References	150
Vita	158

List of Tables

Table 2.1:	Mass ratios were calculated for Mg alloy AZ31 and Al alloy AA5182 relative to steel. The mass ratios were calculated assuming equal bending strength (Equation 3) and equal bending stiffness (Equation 4), with thickness as a free variable. The material properties used to calculate the mass ratios are also provided. Data are from Ref. 17. ...6
Table 2.2:	The parameters describing the SDTD material constitutive model are presented [42]. The material model is described by the form of Equation 20. A_{GBS} and n_{GBS} are described as functions of true strain, ϵ , while A_{DC} and n_{DC} are described as constants.....21
Table 4.1:	The Mg AZ31 sheet material composition is shown in wt%.29
Table 5.1:	Grain size and true strain measurements, along with their respective uncertainties, are presented for each tensile specimen examined. Specimens designated with a * developed some abnormal grains in the gage region.46
Table 5.2:	The parameters obtained from fitting the static grain growth models to experimental data are provided. The value of d_o was assumed to be 8.7 μm , which was the smallest grain size measured in the grip regions of the tensile specimens.....49
Table 5.3:	The values of α obtained from fitting the dynamic grain growth models to experimental data are provided. The value of d_o was assumed to be 8.7 μm , which was the smallest grain size measured in the grip region of the tensile specimens.....51

Table 5.4:	The parameters resulting from fits to tensile data of AZ31 sheet at 450°C are presented. Data from true-strain rates ranging from 10^{-4} to $3 \times 10^{-3} \text{ s}^{-1}$ followed the Voce strain-hardening law (Equation 49). At true-strain rates ranging from 10^{-4} to $3 \times 10^{-3} \text{ s}^{-1}$, the flow stress exhibited a nearly constant value of σ_m for strains ranging from 0 to 0.6. The values in the table are from Ref. 42.	56
Table 5.5:	The RMS errors on the base 10 logarithms of true-strain rate are presented for four material constitutive models. Each material model was created using one of the investigated dynamic grain growth models. All material models are given by the form of Equation 48.....	57
Table 5.6:	The parameters describing the final grain size model are presented. The grain size model is described by the form of Equation 50.....	57
Table 5.7:	The parameters describing the GDTD material constitutive model are presented. The material model is described by the form of Equation 48.	58
Table 6.1:	R-value and true strain measurements, along with their respective uncertainties, are presented for each tested tensile specimen. The fraction of dislocation-climb creep strain that each specimen experienced, which was estimated using the GDTD material model, is also shown.....	64
Table 8.1:	The RMS errors on true stresses for the SDTD, SDTDM1, SDTDAM, and GDTDAM material constitutive models are presented. All values are in MPa.	90

Table 8.2:	The MPD errors on true stresses for the SDTD, SDTDM1, SDTDAM, and GDTDAM material constitutive models are presented. All values are percentages.....	91
Table 8.3:	The RMS errors on dome heights for the SDTD, SDTDM1, SDTDAM, and GDTDAM material constitutive models are presented. Experiments and simulations were conducted using the University of Texas geometry. All values are in mm.	95
Table 8.4:	The MPD errors on dome heights for the SDTD, SDTDM1, SDTDAM, and GDTDAM material constitutive models are presented. Experiments and simulations use the University of Texas geometry. All values are percentages.....	96
Table 8.5:	The RMS errors on dome heights for the SDTD, SDTDM1, SDTDAM, and GDTDAM material constitutive models are presented. Experiments and simulations use the General Motors geometry. All values are in mm.	98
Table 8.6:	The MPD errors on dome heights for the SDTD, SDTDM1, SDTDAM, and GDTDAM material constitutive models are presented. Experiments and simulations use the General Motors geometry. All values are percentages.....	98
Table 8.7:	The RMS errors on pole thicknesses for the SDTD, SDTDM1, SDTDAM, and GDTDAM material constitutive models are presented. Experiments and simulations use the General Motors geometry. All values are in mm.	98

Table 8.8:	The MPD errors on pole thicknesses for the SDTD, SDTDm1, SDTDAM, and GDTDAM material constitutive models are presented. Experiments and simulations use the General Motors geometry. All values are percentages.....	99
Table 8.9:	The RMS and MPD errors on dome heights are presented for the GDTDAM material model at 450°C and 830 kPa. Experiments and simulations use the University of Texas geometry, and only preheat time was varied.	104
Table 8.10:	The RMS and MPD errors on both dome heights and pole thicknesses are presented for the GDTDAM material model at 450°C. Experiments and simulations use the General Motors geometry, and only initial grain size was varied.	106

List of Figures

Figure 1.1: A magnesium-alloy AZ31 trunk inner panel is shown. The component was formed using gas-pressure at high temperature ($>450^{\circ}\text{C}$). The figure is from Ref. 15.	2
Figure 2.1: AZ31 tensile elongation-to-rupture is plotted against temperature. Data are from Ref. 13 and 14.	8
Figure 2.2: An HCP unit cell is shown along with examples of basal, prismatic, and pyramidal planes.	10
Figure 2.3: Critical resolved shear stress (CRSS) is plotted against temperature for basal slip, prismatic slip, pyramidal slip, and twinning in magnesium. Data are from Ref. 24 through 29. Figure is from Ref. 23.	10
Figure 2.4: The logarithm of true-strain rate is plotted against the logarithm of true stress for AZ31 tensile specimens tested at temperatures ranging from 350 to 500°C . Markers represent tensile data, while lines represent the 1.3 sigma material model (Equation 17) fit to the data. The figure is from Ref. 41.	18
Figure 2.5: The logarithm of true-strain rate is plotted against the logarithm of true stress for AZ31 tensile specimens tested at 450°C . Markers represent tensile data, while lines represent the SDTD sigma material model (Equation 20) fit to the data. The figure is from Ref. 42.	20
Figure 3.1: The methodology used in this investigation to create and validate new material constitutive models describing sheet metal deformation behavior is shown as a flowchart.	25

Figure 3.2:	A biaxial gas-pressure bulge forming specimen is shown. AZ31 sheet was formed into a circular die with a diameter of 100 mm. The specimen was formed at 450°C and a gas pressure of 75 psi.....	27
Figure 4.1:	Photomicrographs of (a) the as-received AZ31 sheet microstructure and (b) the microstructure after annealing at 450°C in salt for 80 s are shown.	29
Figure 4.2:	An untested AZ31 tensile coupon is shown.....	30
Figure 4.3:	The apparatus used in tensile testing of the AZ31 sheet is shown....	32
Figure 4.4:	The shoulder-loading grips used during tensile testing are shown. ...	32
Figure 4.5:	Metallographic samples were sectioned from (A) the grip and (B) the gage region of each tensile specimen. The short-transverse direction (SD) of the specimen is perpendicular to the sheet. The tensile direction (TD) is also the rolling direction (RD) of the sheet.	37
Figure 4.6:	A photograph of the University of Texas bulge testing apparatus is shown. The photograph is from Ref. 69.	38
Figure 4.7:	An example specimen blank used in bulge testing (left) and dome formed from the University of Texas apparatus (right) are presented.	39
Figure 4.8:	The furnace and die used in biaxial gas-pressure bulge tests at General Motors are shown.....	41
Figure 5.1:	A photomicrograph containing an example of an abnormally large grain is shown. This abnormal grain was observed in the gage region of the tensile specimen tested at $3 \times 10^{-2} \text{ s}^{-1}$ to a final true strain of 0.39....	47

- Figure 5.2: The average grain size in the undeformed grip region, d_s , is plotted against time, t , for tensile specimens tested at 450°C and constant true-strain rates ranging from 10^{-4} to $3 \times 10^{-2} \text{ s}^{-1}$. Experimental data are shown as open circles, while fits to the data using Equations 36 and 37 are shown as curves. The closed circles are grain size measurements from specimens annealed in salt at 450°C.49
- Figure 5.3: The difference in average grain size between the gage region and grip region after tensile deformation, $d - d_s$, is plotted against true strain, ϵ . The experimental measurements, which are shown as markers, were obtained from tensile specimens tested at 450°C and constant true-strain rates ranging from 10^{-4} to $3 \times 10^{-2} \text{ s}^{-1}$. Fits to the data using the Wilkinson-Cáceres and Kim *et al.* models are shown as curves.51
- Figure 5.4: The ratio of average grain size between the gage region and grip region after tensile deformation, d/d_s , is plotted against true strain, ϵ . The experimental measurements, which are shown as markers, were obtained from tensile specimens tested at 450°C and constant true-strain rates ranging from 10^{-4} to $3 \times 10^{-2} \text{ s}^{-1}$. Fits to the data using the Seidensticker-Mayo and Sato *et al.* models are shown as curves.....53
- Figure 5.5: The logarithm of true-strain rate is plotted against the logarithm of true stress for AZ31 tensile specimens tested at 450°C. Markers represent tensile data, while curves represent the GDTD material model (Equation 48) fit to the data.59
- Figure 6.1: A volume of Mg AZ31 sheet is subject to a tensile stress from uniaxial loading in the z-direction. The plane of the sheet is perpendicular to the x-direction, and the tensile axis is along the z-direction.62

Figure 6.2: Effective R-value, r_{eff} , is plotted against the fraction of true strain from dislocation-climb creep, f_{DC} . Experimental data are plotted as markers. R-values expected from theory (Equation 55) are plotted as a solid line. Values of f_{DC} for experimental data were determined using the GDTD material model.	65
Figure 6.3: Effective R-value, r_{eff} , is plotted against final true strain, ϵ_f . Experimental data are plotted as markers. R-values expected from theory (Equation 55) are plotted as a solid line.	67
Figure 6.4: Pole figures obtained from EBSD of the AZ31 sheet are shown. The sheet was recrystallized at 150°C for 20 minutes prior to EBSD. Texture intensities are displayed using a times-random scale. The pole figures were obtained by Aravindha Antoniswamy.....	74
Figure 7.1: The mesh used in Abaqus tensile simulations is shown. The mesh elements are 1 mm on a side with an initial thickness of 2 mm. The X indicates the element for which stresses and strains are output during simulations. The figure is from Ref. 23.	79
Figure 7.2: The mesh used in Abaqus gas-pressure bulge forming simulations of the University of Texas geometry is shown. The nodes of the axisymmetric sheet blank and forming die meshes are shown as red markers, while the axisymmetric elements are shown as red lines. The axisymmetric mesh is revolved 180° around the axis of symmetry to provide a better visualization of the blank and die. The AZ31 blank is shown in blue, while the forming die is shown in gray.....	81

Figure 8.1:	True stress (a) data and (b) the corresponding Voce law fits are plotted against true strain for tensile tests at 450°C and 10^{-3} s^{-1} . Solid curves represent data from this study, while dashed curves represent data from a previous study [42].	85
Figure 8.2:	True stress is plotted against true strain for tensile tests at 450°C and 10^{-1} s^{-1} . Solid curves represent data from this study, while dashed curves represent data from a previous study [42].	86
Figure 8.3:	Dome height is plotted against forming time for bulge tests run using the University of Texas apparatus at 450°C and 830 kPa. Solid curves represent data from this study, while dashed curves represent data from a previous study [23].	87
Figure 8.4:	Dome height is plotted against forming time for bulge tests run using the University of Texas apparatus at 450°C and (a) 550 kPa or (b) 1100 kPa. Solid curves represent data from this study, while dashed curves represent data from a previous study [23].	88
Figure 8.5:	True stress is plotted against true strain at 450°C for constant true-strain rates of (a) 10^{-4} , (b) 3×10^{-4} , (c) 10^{-2} , and (d) $3 \times 10^{-2} \text{ s}^{-1}$. Experimental data are from Ref. 42. For all strain rates, the SDTD simulation results are identical to the SDTDAM results.	90
Figure 8.6:	Effective R-values, r_{eff} , are plotted against true strain for constant true-strain rates of 10^{-4} , 3×10^{-4} , 10^{-2} , and $3 \times 10^{-2} \text{ s}^{-1}$. Experimental data are plotted as markers. SDTD and SDTDM1 simulation results are plotted as a dashed line for all strain rates. SDTDAM and GDTDAM simulation results are plotted as solid curves for each strain rate.	93

Figure 8.7: Dome height is plotted against forming time at 450°C for gas pressures of (a) 550, (b) 830, and (c) 1100 kPa. Experiments and simulations use the University of Texas geometry.....	95
Figure 8.8: (a) Dome height and (b) pole thickness are plotted versus forming time at 450°C and 280 kPa. Experiments and simulations use the General Motors geometry.....	97
Figure 8.9: (a) Dome height and (b) pole thickness are plotted versus forming time at 450°C and 520 kPa. Experiments and simulations use the General Motors geometry.....	98
Figure 8.10: Dome height is plotted against forming time for biaxial gas-pressure bulge tests for which only preheat time varied. The experiments use the University of Texas apparatus at 450°C and 830 kPa.	101
Figure 8.11: Dome height is plotted against forming time for biaxial gas-pressure bulge simulations using the GDTDAM model. All simulations use the University of Texas geometry at 450°C and 830 kPa with only preheat time varying.	102
Figure 8.12: Dome height is plotted against forming time at 450°C and 830 kPa for preheat times of (a) 30, (b) 120, and (c) 960 s. Experiments use the University of Texas apparatus, and simulations were conducted using the GDTDAM material model.	103
Figure 8.13: (a) Dome height and (b) pole thickness are plotted versus forming time at 450°C and 280 kPa. Experiments use the General Motors apparatus, and simulations were conducted using the GDTDAM material model.	105

Figure 8.14: (a) Dome height and (b) pole thickness are plotted versus forming time at 450°C and 520 kPa. Experiments use the General Motors apparatus, and simulations were conducted using the GDTDAM material model.106

Figure A.1: R-values are plotted against the distance from the end of the tensile mesh, which represents the distance from the grip in an actual tensile test. Simulations were conducted using the SDTD and SDTDAM material models at 10^{-3} s^{-1} to a final true strain of 0.6.115

Chapter 1: Introduction

In the automotive and aircraft industries, weight reduction is an effective method of increasing both the fuel efficiency and performance of a vehicle [1-5]. For example, a 45 kg reduction in the weight of a 1,450 kg automobile can lead to a 0.6 miles-per-gallon improvement [5]. Therefore, lightweight magnesium alloys may be preferred over heavier materials, such as steels and aluminum alloys, for some applications. Magnesium is an attractive choice because of its lower density compared to steel or aluminum [6-11]. It is approximately two-thirds as dense as aluminum and over 75% less dense than steel. There is substantial interest in forming automotive components from wrought magnesium sheet alloys to achieve a reduction in vehicle weight. One particular alloy of interest, AZ31, is the most widely available commercial wrought magnesium alloy, due to its combination of strength, ductility, and corrosion resistance [12].

Although magnesium alloys such as AZ31 possess desirable properties, forming automotive parts from magnesium can be challenging. Magnesium alloys exhibit insufficient ductility at room temperature for forming the complex shapes required for many applications. For example, AZ31 exhibits tensile elongations of approximately 15% at room temperature [13]. To obtain sufficient ductility for the manufacture of complex parts, forming can be performed at high temperatures. At 450°C, AZ31 exhibits tensile elongations in excess of 250% [14]. High-temperature gas-pressure forming technologies

have already been used to produce demonstration automotive panels from AZ31 sheet [15], such as the trunk inner panel shown in Figure 1.1.

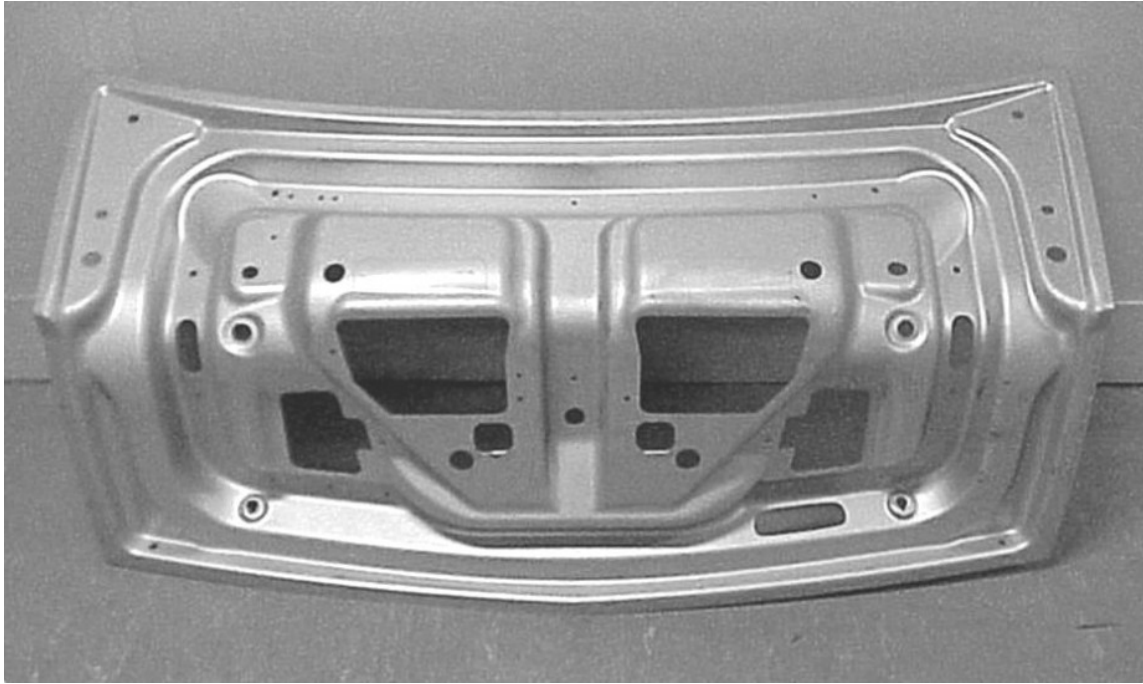


Figure 1.1: A magnesium-alloy AZ31 trunk inner panel is shown. The component was formed using gas-pressure at high temperature ($>450^{\circ}\text{C}$). The figure is from Ref. 15.

Finite-element-method (FEM) simulations can assist in determining the processing parameters (temperature, gas pressure) necessary for high-temperature forming of complex components. During FEM simulations, the deformation response of a workpiece material is described mathematically through a constitutive model relating stresses within the material to the resulting strains. Simulation results can be used to obtain useful predictions, such as the time required to form a component for particular

processing parameters. However, these predictions will only be accurate if an accurate material constitutive model is used.

Some material constitutive models may contain artificial modifications to obtain accurate predictions of forming behavior under specific conditions. However, if the physical basis behind such modifications is not understood, it is difficult to predict behavior beyond these specific processing conditions. A physics-based material model is one where all components of the model have a physical basis. An understanding of the physics behind a material model makes it easier to evaluate the advantages and disadvantages of that model. The model can then, ideally, be modified to accurately account for the physical mechanisms that affect deformation across a broad range of conditions. Such a model allows for accurate forming behavior predictions described by only the most important process and material variables.

The purpose of this dissertation is to construct physics-based material constitutive models capable of accurately predicting the forming behavior of AZ31 sheet at 450°C. Tensile test data are used to construct material models describing the mechanisms controlling deformation at 450°C. These material models are used in FEM simulations, from which results are compared to data from tensile tests and biaxial gas-pressure forming experiments. The goal of this research is for the new material models to represent an improvement over AZ31 material models currently found in the literature.

Chapter 2: Literature Review

2.1. ADVANTAGES OF MAGNESIUM ALLOYS

During the design process, it is often desirable to minimize or maximize a parameter while subject to some constraint. For example, automotive body panels are primarily subject to bending loads. These panels should be as lightweight as possible to maximize fuel efficiency. Thus, the objective is to minimize the mass of the panel. Panel mass can be reduced by decreasing the thickness of the sheet used to manufacture the part. However, the panels must remain thick enough to carry the required loads without exceeding the yield strength of the material or excessively deflecting. Thus, the sheet material should be chosen to minimize panel weight while maintaining the required bending strength and stiffness, which are constraints on the design of the panel.

One method of determining the optimal material for an application is through the use of structural performance indices [16]. A performance index, M , is calculated using a combination of material properties related to the function of a component. Materials with a large performance index will better minimize or maximize the parameter of interest while meeting the constraints on the design. Consider an automotive component subject to bending loads. The component can be modified by changing material or sheet thickness. If strength is the limiting constraint, the appropriate structural performance index is

$$M = \frac{\sigma_y^{1/2}}{\rho} \quad (1)$$

where σ_y is the yield strength of the material and ρ is density [1, 16]. If stiffness is the limiting constraint, the appropriate structural performance index is

$$M = \frac{E^{1/3}}{\rho} \quad (2)$$

where E is the elastic modulus of the material and ρ is density [1, 16]. These performance indices are appropriate for bending and in-plane biaxial buckling when thickness is a free variable. Note that the sole goal in this analysis is to minimize the weight of the component irrespective of cost.

Luo [17] used structural performance indices to demonstrate that magnesium components can be made lighter than corresponding aluminum and steel components while retaining the same bending stiffness and strength. The performance indices given by Equations 1 and 2 are inversely proportional to the mass required in a part of a particular material. Thus, the mass ratio of components manufactured from two different materials, each with the same bending strength, is

$$\frac{m_2}{m_1} = \left(\frac{\sigma_{y,1}}{\sigma_{y,2}} \right)^{1/2} \frac{\rho_2}{\rho_1} \quad (3)$$

where m is the mass of a component, σ_y is the yield strength of a material, ρ is the density of a material, and the subscripts 1 and 2 refer to the two materials. Similarly, the mass ratio of components manufactured from two different materials, each with the same bending stiffness, is

$$\frac{m_2}{m_1} = \left(\frac{E_1}{E_2} \right)^{1/3} \frac{\rho_2}{\rho_1} \quad (4)$$

where m is the mass of a component, E is the elastic modulus of a material, ρ is the density of a material, and the subscripts 1 and 2 refer to the two materials. Luo calculated these mass ratios for various aluminum and magnesium alloys with respect to steel. The mass ratios for magnesium alloy AZ31, aluminum alloy AA5182, and steel, along with the relevant material properties, are presented in Table 2.1.

Table 2.1: Mass ratios were calculated for Mg alloy AZ31 and Al alloy AA5182 relative to steel. The mass ratios were calculated assuming equal bending strength (Equation 3) and equal bending stiffness (Equation 4), with thickness as a free variable. The material properties used to calculate the mass ratios are also provided. Data are from Ref. 17.

Material	Density (g/cm ³)	Yield Strength (MPa)	Elastic Modulus (GPa)	Mass Ratio (equal bending strength)	Mass Ratio (equal bending stiffness)
Mg AZ31	1.77	220	45	0.22	0.38
Al AA5182	2.68	235	70	0.32	0.50
Steel	7.80	200	210	1	1

The results of Luo's analysis confirm that the use of magnesium alloys can provide a significant weight savings relative to both steel and aluminum alloys. For example, an Mg AZ31 component will be 62% lighter than a corresponding steel component while maintaining an equivalent bending stiffness and superior bending strength. Similarly, the Mg AZ31 component will be 24% lighter than a corresponding Al AA5182 component while maintaining an equivalent bending stiffness and superior bending strength. These examples demonstrate the advantages offered by magnesium's low density. Although magnesium alloys have a lower elastic modulus and similar yield strength to many steel and aluminum alloys, the lower density of magnesium allows for parts to be formed from thicker sheet while still retaining less mass than corresponding

steel or aluminum parts. These thicker magnesium parts can equal or exceed the bending stiffness and strength of the thinner steel or aluminum parts. For these reasons, magnesium alloys are being investigated as potential replacements for steel and aluminum alloys in automotive components such as body panels and instrument housings [6-11]. It should be noted that Luo does not specify a particular steel alloy in his analysis, and many steels have yield strengths much greater than 200 MPa, which would reduce the advantage of magnesium in this analysis. Note also that magnesium alloys are more expensive than steel and aluminum alloys both per unit weight and per unit volume [17]. The mass savings represented by magnesium may or may not be worth the increased cost depending on the particular application.

2.2. HIGH-TEMPERATURE FORMING

Although magnesium alloys possess advantageous material properties, they also present challenges with respect to forming complex sheet metal components. Magnesium alloys are often excellent choices for manufacturing processes such as machining and casting [12]. However, automotive body panels are typically manufactured from sheet materials using traditional deformation processes such as die stamping [18-20]. Magnesium alloys, including AZ31, do not exhibit sufficient ductility for the formation of complex components at room temperature. Figure 2.1 shows the tensile elongation-to-rupture behavior of AZ31 as a function of temperature. At room temperature, the elongation-to-rupture of AZ31 is approximately 15% [13], which is significantly less than both steel and aluminum [17, 21]. However, the ductility of magnesium can be increased

significantly by forming at elevated temperatures. At 450°C, the elongation-to-rupture of AZ31 is greater than 400% [14]. This suggests that high-temperature forming can be used to manufacture the complex magnesium sheet metal components required for automotive applications.

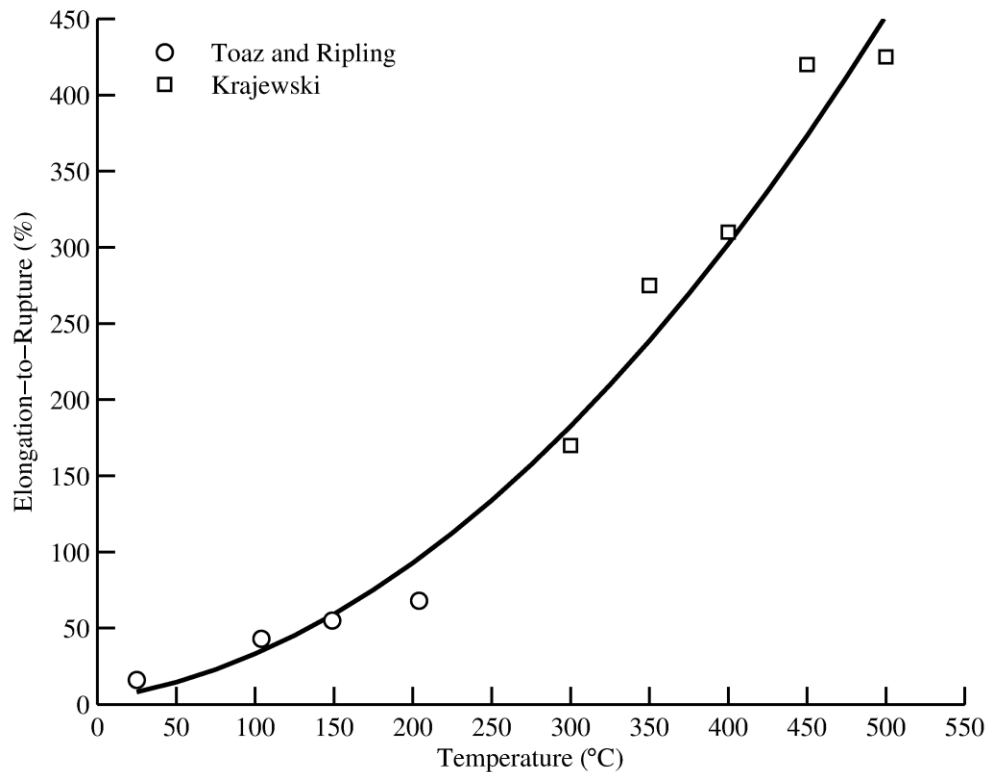


Figure 2.1: AZ31 tensile elongation-to-rupture is plotted against temperature. Data are from Ref. 13 and 14.

The plastic behavior of magnesium results from its hexagonal close-packed (HCP) crystal structure, which is shown in Figure 2.2. HCP materials can deform through dislocation slip on basal, prismatic, or pyramidal planes, or by twinning. Five independent active slip systems are required for a polycrystalline material to exhibit

ductile behavior [22]. A slip system is only active if the resolved shear stress is greater than the critical resolved shear stress (CRSS) required for slip. Figure 2.3 [23] presents the CRSS for basal slip, prismatic slip, pyramidal slip, and twinning as a function of temperature [24-29]. At room temperature, only basal slip is active, which provides only two independent slip systems. The other slip systems must be provided by prismatic slip, pyramidal slip, or twinning. Prismatic slip and pyramidal slip require a much larger CRSS than basal slip, which makes them largely inactive at room temperature. Twinning can provide additional slip systems, but the formation of twins reorients the crystal structure of the material in locations and increases the area of interfaces between grains. These interfaces constrain the movement of dislocations, which leads to an increase in the CRSSs required for slip. Generally, there are too few active slip systems at room temperature for magnesium alloys to exhibit significant ductility. As temperature increases, the CRSSs for prismatic and pyramidal slip decrease significantly, and these additional slip systems become active [30]. The increase in the number of active slip systems with increasing temperature results in a corresponding increase in the ductility of magnesium alloys, such as is shown for AZ31 in Figure 2.1. High-temperature forming technologies are therefore effective for forming wrought magnesium sheet alloys into the complex shapes required for many applications.

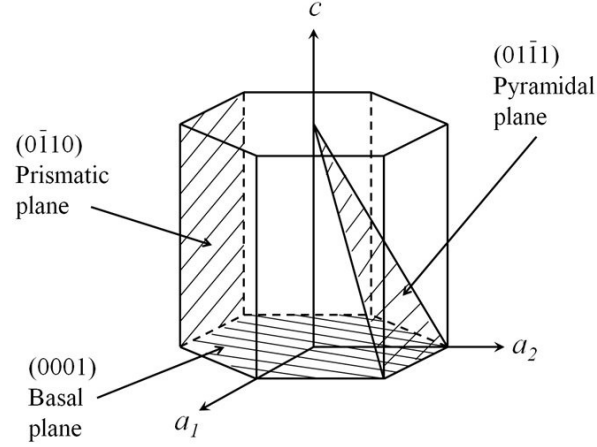


Figure 2.2: An HCP unit cell is shown along with examples of basal, prismatic, and pyramidal planes.

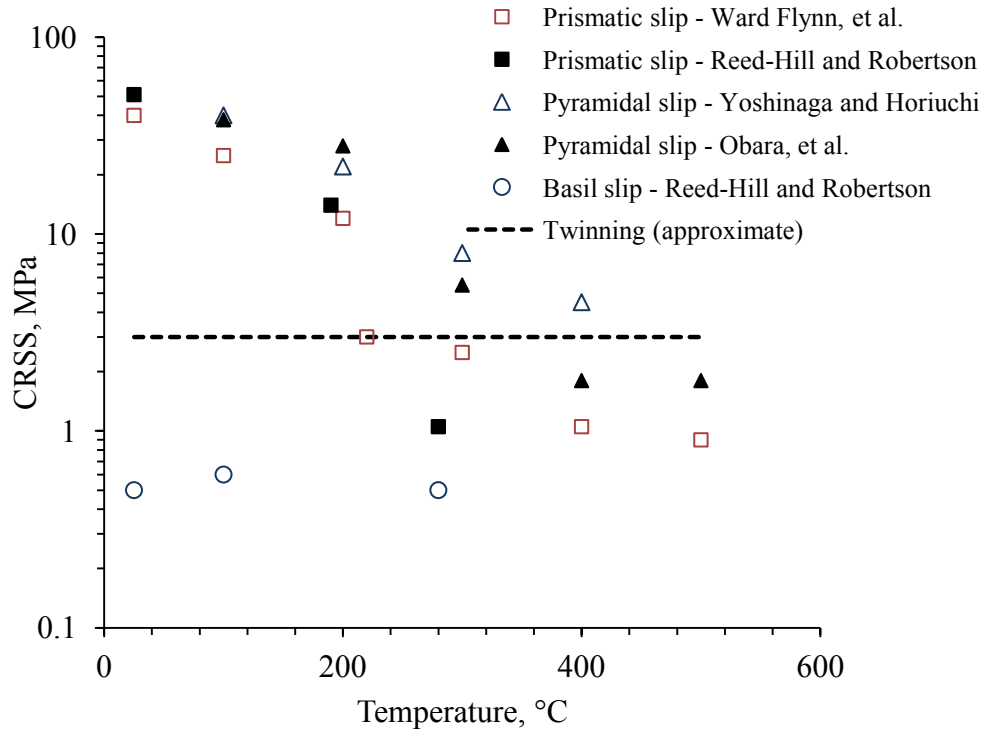


Figure 2.3: Critical resolved shear stress (CRSS) is plotted against temperature for basal slip, prismatic slip, pyramidal slip, and twinning in magnesium. Data are from Ref. 24 through 29. Figure is from Ref. 23.

One high-temperature forming process used to create complex automotive and aerospace components is superplastic forming (SPF) [31-34]. SPF of aluminum and magnesium alloys is characterized by deformation at high temperatures, typically above 500°C, and slow strain rates less than 10^{-3} s^{-1} . For materials with a fine grain size, typically less than 10 μm , deformation results primarily from grain-boundary-sliding (GBS) creep. GBS creep is associated with a high strain-rate sensitivity, m , of approximately 0.5. Creep mechanisms active at lower temperatures and faster strain rates, such as five-power dislocation-climb creep, typically have values of m of approximately 0.2 [32]. An increase in m reduces the rate of neck growth during deformation, which significantly increases the tensile elongation that can be achieved prior to rupture. Tensile elongations of up to 1000% can be achieved prior to rupture during SPF [33]. Thus, SPF can be used to form the complex components required for automotive and aerospace applications. However, SPF has limitations which make it unsuitable for some applications. Superplasticity can only be maintained in materials with a fine grain size. The high temperatures required for superplasticity can lead to grain growth in many alloys, which eliminates the advantages of SPF. Grain growth must therefore be reduced or eliminated through the use of two-phase alloys or alloys with fine second-phase particles that pin grain boundaries. These alloys may be cost prohibitive for many applications. Also, the slow strain rates required to maintain GBS creep result in a process that can require several minutes to form one component. For these reasons, SPF is an expensive process that is often unsuitable for high-volume applications.

The limitations of the SPF process led to the development of quick plastic forming (QPF), which is characterized by lower temperatures ($\sim 450^{\circ}\text{C}$) and faster strain rates ($>10^{-3} \text{ s}^{-1}$) than SPF [35-37]. GBS creep is no longer the primary active creep mechanism under these conditions. Instead, QPF is characterized by creep mechanisms with moderate values of strain-rate sensitivity. For example, many aluminum alloys deform primarily by solute drag creep at the temperatures and strain rates characteristic of QPF [38-39]. The value of m for solute drag creep is approximately 0.3, which falls in between the values for GBS creep and dislocation-climb creep. Magnesium alloy AZ31 deforms by both GBS creep and dislocation-climb creep at the temperatures and strain rates characteristic of QPF [40-42]. Both GBS creep and dislocation creep have been shown to occur in AZ31 at 450°C through the use of marker lines and scanning electron microscopy [40]. The combination of the two creep mechanisms also results in a value of m between the expected individual values for GBS creep and dislocation-climb creep. Although less ductility is typically obtained from QPF than from SPF, QPF is still a viable method of manufacturing complex components. In addition, QPF is associated with faster strain rates than SPF, which leads to faster part forming.

2.3. MATERIAL CONSTITUTIVE MODELS

Various material constitutive models describing the high-temperature deformation behavior of AZ31 are available in the literature. Most of these models are fits of simple single-term creep laws to tensile data. These creep laws are constitutive relationships

relating true stress, σ , and true-strain rate, $\dot{\epsilon}$. One relationship commonly used to describe AZ31 tensile flow behavior at high temperature [43-45] is

$$\dot{\epsilon} = A \left(\frac{\sigma}{E} \right)^n \exp \left(-\frac{Q}{RT} \right) \quad (5)$$

where A and n are constants describing the active creep mechanism, E is the elastic modulus of AZ31 for a particular temperature, T , Q is the activation energy for the active creep mechanism, and R is the ideal gas constant. Another relationship used to describe high-temperature forming of AZ31 [44-47] is

$$\dot{\epsilon} = A \sinh \left(\alpha \frac{\sigma}{E} \right)^n \exp \left(-\frac{Q}{RT} \right) \quad (6)$$

where α is a fitting parameter. The hyperbolic sine term allows Equation 6 to describe deformation behavior at faster strain rates for which power-law breakdown begins to occur, i.e. Equation 5 is no longer valid. If flow behavior is investigated at a single temperature, then Equations 5 and 6 simplify to

$$\dot{\epsilon} = A' \sigma^n \quad (7)$$

$$\dot{\epsilon} = A' \sinh(\alpha' \sigma)^n \quad (8)$$

respectively, where A' and α' are constants describing the active creep mechanism. A third relationship used to describe high-temperature forming of AZ31 is

$$\sigma = K \epsilon^{n'} \dot{\epsilon}^m \quad (9)$$

where K is a constant describing the active creep mechanism, ϵ is true strain, n' is the strain hardening exponent, and m is the strain-rate sensitivity [47]. Equation 9 can account for strain hardening during creep. The accuracies of the material constitutive

models described by Equations 5 through 9 are often checked only against experimental data from tensile tests [43-47].

Of particular note are the material constitutive models created by Khraisheh and Abu-Farha. Khraisheh *et al.* [48] and Abu-Farha *et al.* [49] proposed a material model,

$$\dot{\varepsilon} = \frac{k}{d^p} \left[\frac{\sigma}{1-f_a} \right]^{\frac{1}{m}} \quad (10)$$

where k is a material constant, d is average grain size, p is the grain size exponent, and f_a is the area fraction of voids. This model can account for the effects of cavitation and grain size on deformation behavior. In Equation 10, d and f_a are calculated using

$$d = d_o + C\varepsilon \quad (11)$$

$$f_a = f_{ao} \exp(\psi\varepsilon) \quad (12)$$

respectively, where d_o is the initial grain size, C is a grain growth material parameter, f_{ao} is the initial fraction of voids, and ψ is a void growth material parameter. Equation 10 accurately describes the tensile deformation behavior of AZ31 at 400°C and strain rates from 5×10^{-5} to 10^{-3} s^{-1} . Abu-Farha *et al.* also proposed a generalized material constitutive model,

$$D^p_{ij} = \left[\frac{C_I (J - (K_o + R))^{\frac{1}{m}}}{d^p} + C_{II} J^n \right] \frac{\partial J}{\partial \sigma_{ij}} \quad (13)$$

which is appropriate for multiaxial stress states and can account for anisotropic deformation [50-51]. In Equation 13, D^p_{ij} is a component of the deformation tensor, J is an appropriate anisotropic yield function, $K_o + R$ is a reference stress (R accounts for

hardening), C_I and C_{II} are material constants, and σ_{ij} is a component of the stress tensor. However, the accuracy of Equation 13 was only investigated under uniaxial loading conditions, and it was assumed that deformation is isotropic and only subject to hardening by grain growth. Under these conditions, Equation 13 reduces to Equation 10. In addition, Abu-Farha and Khraisheh [52] investigated the effects of AZ31 sheet orientation on deformation at 375 and 400°C. Tensile tests were conducted at orientations of 0°, 45°, and 90°, and it was determined that sheet orientation has little effect on tensile stress-strain behavior. This indicates that AZ31 does not exhibit planar anisotropy under these conditions. Note that this does not preclude the existence of plastic anisotropy normal to the plane of the AZ31 sheet.

There has also been some investigation of AZ31 high-temperature deformation behavior due to biaxial stress. It is thought that a biaxial stress state may be more characteristic of the stress states occurring during forming of complex automotive components. Palumbo *et al.* [53] and El Morsy *et al.* [54] used AZ31 gas-pressure biaxial bulge forming experiments to determine appropriate fitting parameters for Equation 7. Giuliano and Franchitti [55] performed similar experiments to determine appropriate fitting parameters for Equation 9. Both Palumbo *et al.* and Giuliano and Franchitti examined AZ31 deformation behavior at 520°C, while El Morsy *et al.* examined AZ31 deformation behavior at 370, 400, and 430°C. Palumbo *et al.* [53] compared results from FEM simulations to experimental bulge profile measurements through the use of an objective function. They modified the fitting constants in Equation 7 to minimize the value of the objective function. By this method, the values of A' and n in Equation 7 were

optimized. Giuliano and Franchitti [54] also used objective functions to determine K and n' in Equation 9, although m was calculated separately using

$$m = \frac{\ln(p_1/p_2)}{\ln(t_1/t_2)} \quad (14)$$

where p_1 and p_2 are the gas pressures required to reach a particular dome height in times t_1 and t_2 , respectively. El Morsy *et al.* [55] calculated an effective stress, σ_e , and effective strain, ε_e , using

$$\sigma_e = \frac{p}{4t_f} \left(\frac{h^2 + R^2}{h} \right) \quad (15)$$

$$\varepsilon_e = \left| \ln \left(\frac{t_f}{t_i} \right) \right| \quad (16)$$

where p is gas pressure, h is dome height, R is the radius of the die cavity, t_f is final thickness at the pole, and t_i is initial thickness at the pole. The parameters in Equation 7 were then fit to these values of σ_e and ε_e .

The material constitutive models described above are all designed to predict forming behavior when a single creep mechanism controls deformation. However, recent studies suggest that the high-temperature forming behavior of AZ31 is controlled by two creep mechanisms. Taleff *et al.* [41] conducted AZ31 strain-rate-change tensile tests at temperatures from 350 to 500°C and strain rates from 10^{-4} to $3 \times 10^{-2} \text{ s}^{-1}$. Figure 2.4 shows the logarithm of true-strain rate plotted against the logarithm of true stress for these experiments. These experiments indicate that AZ31 forming behavior under these conditions is controlled by two independent creep mechanisms. The slope of the data in

Figure 2.4 corresponds to the stress exponent of the active mechanism [56-57]. At high temperatures and slow strain rates, the slopes of the data are less than 2, indicating that GBS creep controls deformation for these conditions. At lower temperatures and faster strain rates, the slopes of the data increase to approximately 5, indicating that five-power dislocation-climb (DC) creep controls deformation for these conditions. Taleff *et al.* fit a material model of the form

$$\dot{\epsilon} = A_{GBS} \left(\frac{\sigma}{E} \right)^{n_{GBS}} \exp \left(-\frac{Q_{GBS}}{RT} \right) + A_{DC} \left(\frac{\sigma}{E} \right)^{n_{DC}} \exp \left(-\frac{Q_{DC}}{RT} \right) \quad (17)$$

where $\dot{\epsilon}$ is true-strain rate, σ is true stress, E is the elastic modulus of magnesium, R is the ideal gas constant, T is temperature, A_{GBS} , n_{GBS} , and Q_{GBS} are constants that describe GBS creep in AZ31, and A_{DC} , n_{DC} , and Q_{DC} are constants that describe DC creep in AZ31. The first term in Equation 17 represents the true-strain rate due to GBS creep, and the second term in Equation 17 represents the true-strain rate due to dislocation-climb creep. For independent creep mechanisms, these two terms are added together to calculate the total true-strain rate, after the manner described by Sherby and Burke [56]. A second material model, referred to as the 1.3 sigma model, was created by dividing σ in Equation 17 by 1.3 to account for differences between tensile tests and biaxial gas-pressure forming experiments. The 1.3 sigma model provided successful predictions of dome height and pole thickness as a function of time when used in simulations of biaxial gas-pressure bulge forming at 450 and 900 kPa. Note that Figure 2.4 indicates that flow stress increases with strain at slow strain rates and high temperatures, which indicates that GBS

creep in AZ31 is strain-dependent. This strain-dependent behavior is not accounted for by the 1.3 sigma model.

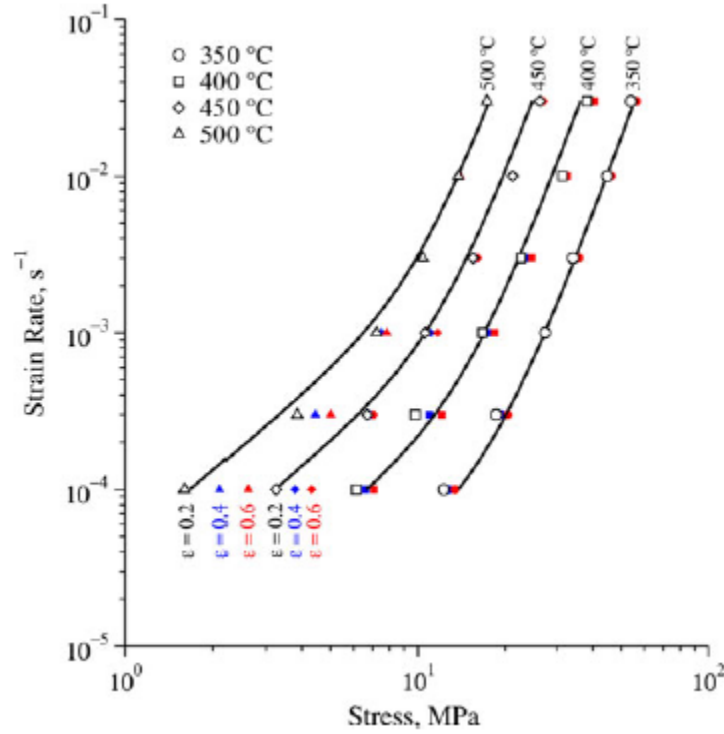


Figure 2.4: The logarithm of true-strain rate is plotted against the logarithm of true stress for AZ31 tensile specimens tested at temperatures ranging from 350 to 500°C. Markers represent tensile data, while lines represent the 1.3 sigma material model (Equation 17) fit to the data. The figure is from Ref. 41.

To account for the strain dependence of GBS creep in AZ31, a strain-dependent tensile data (SDTD) material model was created [42]. Figure 2.5 presents data from AZ31 tensile tests at 450°C and strain rates from 10^{-4} to 10^{-1} s^{-1} . The logarithm of true strain rate is plotted against the logarithm of true stress. Just as with the 1.3 sigma model data, Figure 2.5 indicates that the deformation behavior of AZ31 at 450°C is controlled by two independent creep mechanisms, GBS creep and DC creep. Flow stress increases

as strain increases for a constant slow strain rate less than 10^{-2} s^{-1} . This is an expected result of grain growth during deformation. For a constant temperature, the strain rate for GBS creep, $\dot{\epsilon}_{GBS}$, is

$$\dot{\epsilon}_{GBS} = \frac{A_{GBS}}{d^p} \sigma^{n_{GBS}} \quad (18)$$

where A_{GBS} and n_{GBS} are constants that describe GBS creep in AZ31, d is either the average grain diameter or lineal-intercept grain size, p is the grain size exponent (typically 2-3 for GBS creep), and σ is true stress [56-57]. Grain size is expected to increase through grain growth during deformation at 450°C. As grain size increases with strain and time at temperature, the flow stress required to maintain a particular strain rate for GBS creep will increase according to Equation 18. Thus, flow stress increases with strain for slow strain rates at which GBS creep dominates, see Figure 2.5. At fast strain rates, dislocation-climb creep dominates deformation at 450°C. DC creep does not depend on grain size, so little strain hardening is expected at fast strain rates. Thus, the strain rate for DC creep, $\dot{\epsilon}_{DC}$, is

$$\dot{\epsilon}_{DC} = A_{DC} \sigma^{n_{DC}} \quad (19)$$

where A_{DC} and n_{DC} are constants that describe DC creep in AZ31 and σ is true stress [56-57]. The AZ31 sheet was tested at orientations of 0°, 45°, and 90°, and it was shown that the material does not exhibit planar anisotropy. This agrees with the conclusions of Abu-Fahra and Khraisheh [52].

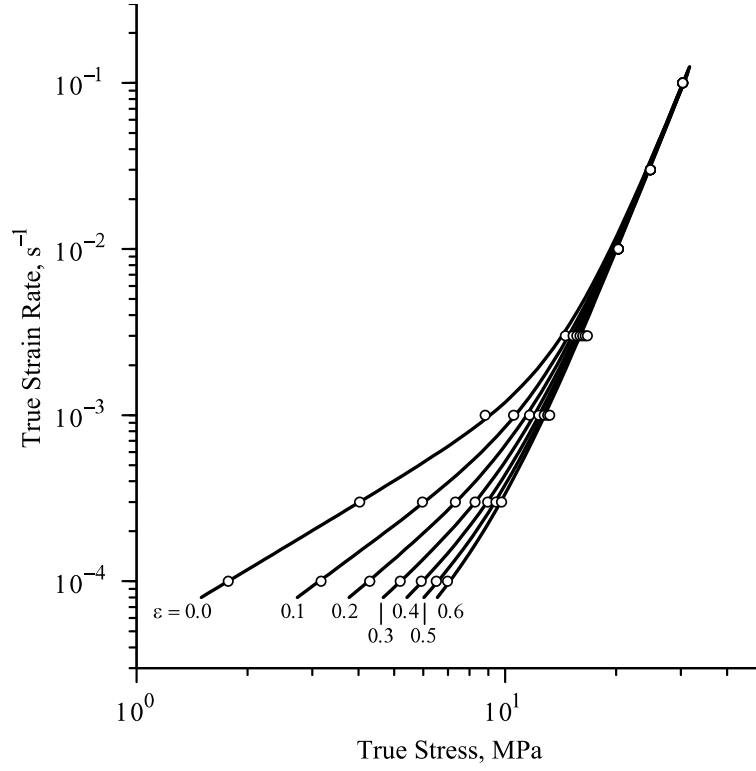


Figure 2.5: The logarithm of true-strain rate is plotted against the logarithm of true stress for AZ31 tensile specimens tested at 450°C. Markers represent tensile data, while lines represent the SDTD sigma material model (Equation 20) fit to the data. The figure is from Ref. 42.

The tensile data shown in Figure 2.5 were used to fit the SDTD material model, which is of the form

$$\dot{\varepsilon} = A_{GBS}(\varepsilon)\sigma^{n_{GBS}(\varepsilon)} + A_{DC}\sigma^{n_{DC}} \quad (20)$$

where $\dot{\varepsilon}$ is the strain rate due to both creep mechanisms, σ is flow stress, A_{GBS} and n_{GBS} are functions of strain, ε , that describe GBS creep, and A_{DC} and n_{DC} are constants that describe DC creep. A_{GBS} and n_{GBS} are described as functions to account for the strain hardening observed at slow strain rates, see Figure 2.5. No hardening is observed at fast

strain rates, so A_{DC} and n_{DC} are constants. Values for A_{GBS} , n_{GBS} , A_{DC} , and n_{DC} are provided in Table 2.2.

Table 2.2: The parameters describing the SDTD material constitutive model are presented [42]. The material model is described by the form of Equation 20. A_{GBS} and n_{GBS} are described as functions of true strain, ε , while A_{DC} and n_{DC} are described as constants.

Parameter	SDTD Material Model
$A_{GBS} \text{ (s}^{-1} \text{ MPa}^{-n_{GBS}})$	$\exp(-9.98 - 12.59\varepsilon + 17.85\varepsilon^2 - 11.1\varepsilon^3)$
n_{GBS}	$1.333 + 0.667\tanh(4.63 \varepsilon)$
$A_{DC} \text{ (s}^{-1} \text{ MPa}^{-n_{DC}})$	5.9×10^{-10}
n_{DC}	5.54

Sherek evaluated the accuracy of the SDTD material model by running simulations of tensile tests and biaxial gas-pressure bulge forming and comparing the results to experimental measurements [23, 42]. During the biaxial bulge forming experiments, gas pressure was used to form an AZ31 blank into the shape of a dome using a cylindrical die. The SDTD material model accurately reproduces tensile data at all strain rates tested (10^{-4} to 10^{-1} s^{-1}) and predicts biaxial bulge forming at low pressures. However, the SDTD material model predicts faster biaxial bulge forming at high pressures than is experimentally observed. To correct for this discrepancy, the flow stress in the dislocation-climb creep term was divided by 1.3, a modification inspired by the 1.3 sigma model, to create a modified material model of the form

$$\dot{\varepsilon} = A_{GBS}(\varepsilon)\sigma^{n_{GBS}(\varepsilon)} + A_{DC}\left(\frac{\sigma}{1.3}\right)^{n_{DC}} \quad (21)$$

which is designated the SDTDM1 (SDTD modification #1) material model. A_{GBS} , n_{GBS} , A_{DC} , and n_{DC} retain their values from the SDTD model. The SDTDM1 material model

predicts biaxial bulge forming behavior at both low and high pressures, but it no longer reproduces the tensile data used to create it. The 1.3 modification is clearly too crude to allow for one material model to accurately predict forming under multiple stress states. An additional weakness of the SDTD material model is revealed by experiments for which only preheat time prior to forming is varied. Sherek observed that the forming rate of the AZ31 blank decreases as preheat time increases, which is consistent with the occurrence of static grain growth during preheating. The SDTD material model cannot account for the effects of preheat time because it is purely a strain-dependent model. This suggests that grain growth in AZ31, and the resulting hardening during GBS creep, may depend on time at temperature as well as strain.

Chapter 3: Objectives and Methodology

3.1. RESEARCH OBJECTIVES

The goal of this study is to create improved material constitutive models capable of accurately predicting the forming behavior of AZ31 sheet at 450°C. This temperature is of interest because it is the temperature at which General Motors forms vehicle closure panels using the QPF process [37]. The current study will address the two weaknesses of the SDTD and SDTDM1 models described in the previous section. To address these weaknesses, a better physical understanding of both GBS creep and DC creep in AZ31 is required. First, grain growth and its relationship to GBS creep are studied. A better physical understanding of the process variables that affect grain growth allows for GBS creep to be modeled more accurately. Second, the differences between tensile forming behavior and biaxial forming behavior at fast rates are investigated. An understanding of the physical mechanism that slows biaxial forming relative to tensile forming during DC creep is necessary to create a material model that describes AZ31 forming behavior for all stress states. It is hypothesized that anisotropic deformation is responsible for the observed differences between tensile and biaxial forming. Material models created during the study are implemented in finite-element-method (FEM) software. The accuracies of simulation predictions using these models are evaluated through comparisons with experimental data.

Ideally, the final result of the study should be a material constitutive model that accurately describes AZ31 forming behavior during all experiments conducted for this

study. Specifically, the material model should accurately reproduce the tensile data used to create it. It should also successfully predict forming due to other stress states, such as those which occur in gas-pressure bulge forming. A material model that can predict forming under multiple stress states (e.g. both uniaxial and balanced biaxial tension) is required to predict the forming of complex components for real-world applications, which may experience different stress states in different regions and at different times during forming. The final material model should also account for the effects of both strain and time on microstructure evolution and the resulting deformation behavior. If microstructure evolution is correctly modeled, effects such as hardening due to preheating can be simulated and accounted for.

3.2. GENERAL METHODOLOGY

The methodology used to create and validate a new material constitutive model is summarized in Figure 3.1. This methodology requires an integrated approach combining theory, experiments, and simulations. A physical understanding of the mechanisms controlling deformation is needed to determine the form of an appropriate material model. Data from AZ31 forming experiments are used to fit the model parameters. In addition, the results of both forming experiments and FEM simulations are required to verify the accuracy of the new material model.

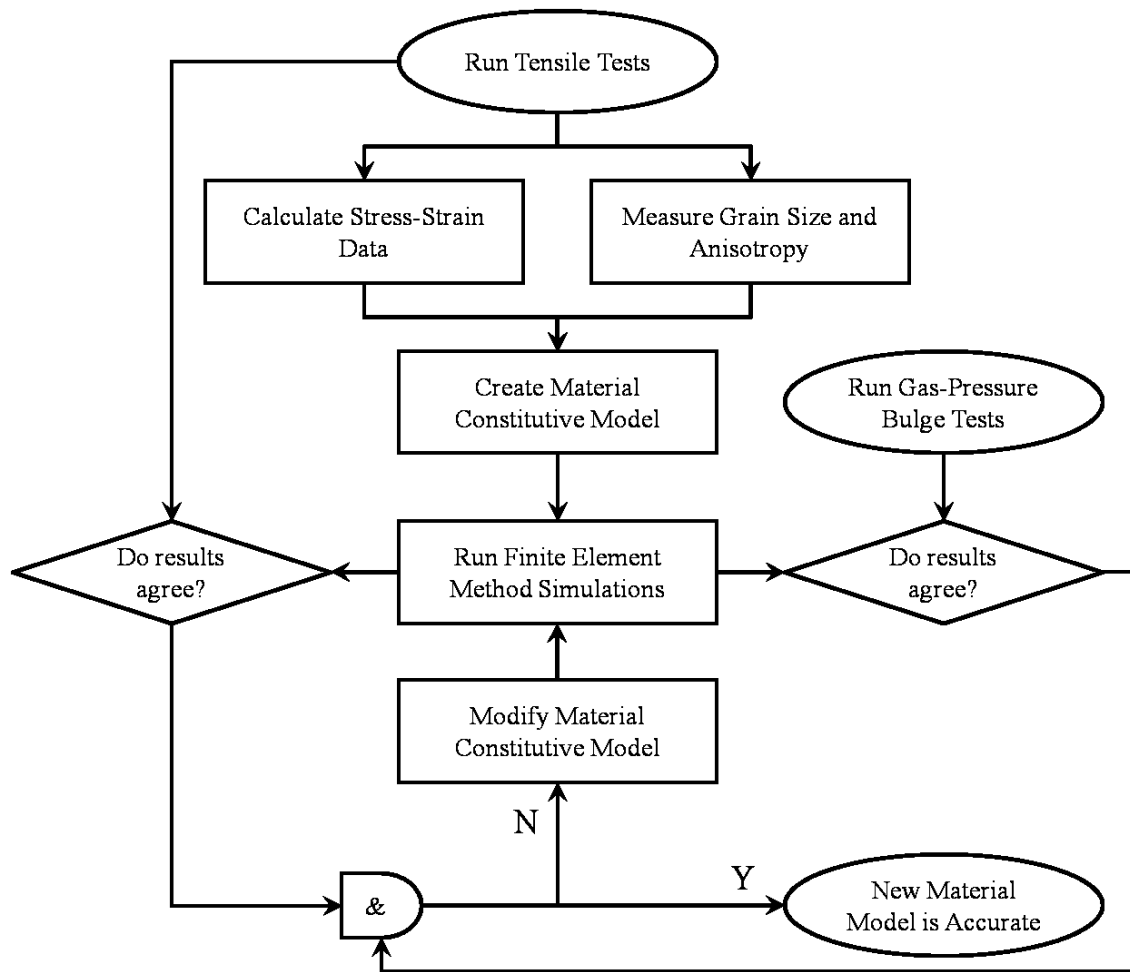


Figure 3.1: The methodology used in this investigation to create and validate new material constitutive models describing sheet metal deformation behavior is shown as a flowchart.

Material constitutive models were constructed primarily using data from tensile tests at 450°C. Tensile tests are useful for creating material models because stress-strain data can be obtained directly from load and displacement measurements. Note that the tensile data from Figure 2.5 continues to be useful when creating new material models. Additional tensile tests were conducted using a computer-controlled, servohydraulic test

frame. Specimens were tested in tension at 450°C and a variety of constant true-strain rates ranging from 10^{-4} to 10^{-1} s^{-1} . These strain rates are characteristic of those experienced by the sheet material during QPF [37]. After the completion of deformation, tensile specimens were quenched in water to arrest further microstructure evolution. Metallography was performed on selected tensile specimens to reveal microstructural characteristics, such as grain size. Anisotropic deformation was quantified through measurement of specimen geometry after deformation. Stress-strain data, geometrical measurements, and microstructural observations were used in construction of new material models that describe AZ31 deformation behavior at 450°C.

Once a material model is created, it must be validated using data from additional experiments. Biaxial gas-pressure forming experiments were used to validate the material models created from tensile data. During biaxial gas-pressure bulge forming, gas pressure is applied to one face of a flat sheet material blank. This pressure causes the blank to form into a cylindrical die, creating a dome such as the one shown in Figure 3.2. During deformation, a biaxial stress state exists near the dome peak. The dome forms freely into the die cavity, and contact between the blank and die is limited to the edge of the specimen. Thus, there is little effect of friction on the experimental results, and deformation is due solely to the material constitutive behavior. Specimen height or thickness was measured at a particular location after forming. It was also possible to measure specimen height *in situ* using a digital micrometer, which provides multiple measurements at a variety of forming times, in an available biaxial gas-pressure bulge forming apparatus. Assuming that material models can be constructed solely from tensile

data, the gas-pressure bulge forming experiments represent an independent check on the accuracy of the material models.

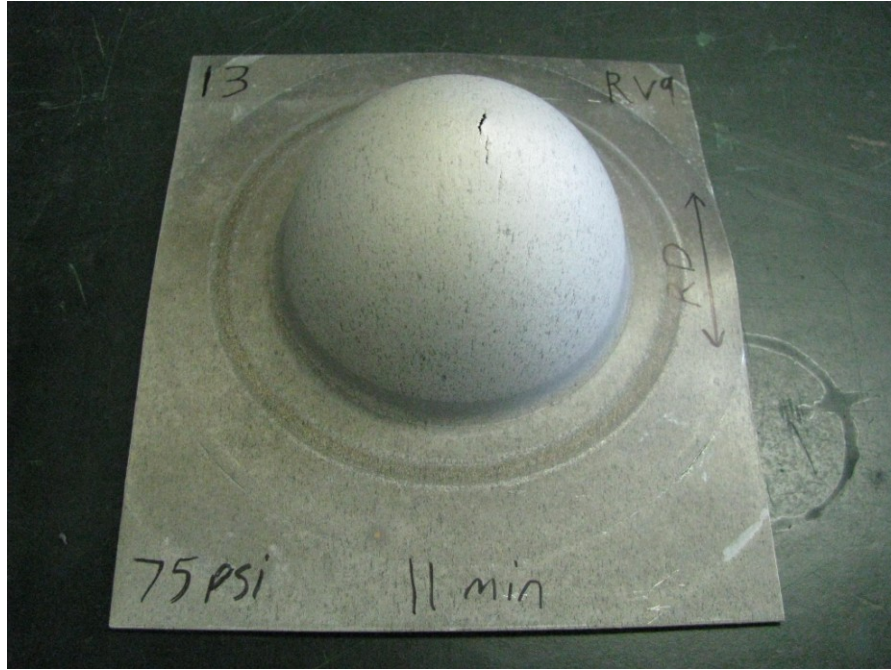


Figure 3.2: A biaxial gas-pressure bulge forming specimen is shown. AZ31 sheet was formed into a circular die with a diameter of 100 mm. The specimen was formed at 450°C and a gas pressure of 75 psi.

Measurements from tensile tests and gas-pressure bulge forming experiments were compared to FEM simulation results to validate material constitutive models. Simulations were conducted using the finite element analysis software AbaqusTM [58]. The AZ31 sheet and die (for simulations of gas-pressure forming experiments) were modeled using discrete elements in an input file, and the stress-strain constitutive behavior of the sheet elements was described by the user-defined material model. Simulation results, such as stress-strain behavior for tensile tests and dome heights for gas-pressure bulge tests, were compared to both tensile test and gas-pressure bulge

forming data to determine the accuracy of material models under various stress states and forming rates. If needed, the material model was modified, and simulations were re-run to check for improved accuracy.

Chapter 4: Experimental Procedures

4.1. MATERIAL DESCRIPTION

The material investigated in this study is a commercial Mg AZ31 rolled sheet supplied in the H24 temper [59]. The as-received thickness of the sheet material is 2 mm, and its composition is provided in Table 4.1. The H24 temper results in the partially-recrystallized microstructure shown in Figure 4.1(a), from which it is difficult to measure an average initial grain size. However, the microstructure finishes recrystallization quickly at 450°C. Figure 4.1(b) shows the microstructure after a static anneal in salt at 450°C for only 80 s. Thus, the AZ31 sheet material is treated as a fully recrystallized microstructure during deformation in subsequent analyses.

Table 4.1: The Mg AZ31 sheet material composition is shown in wt%.

Al	Zn	Mn	Fe	Cu	Ni	Si	Ca	Be	Sr	Ce	Mg
3.1	1.0	0.42	0.006	0.003	<0.003	<0.1	<0.01	<0.005	<0.005	<0.01	bal.

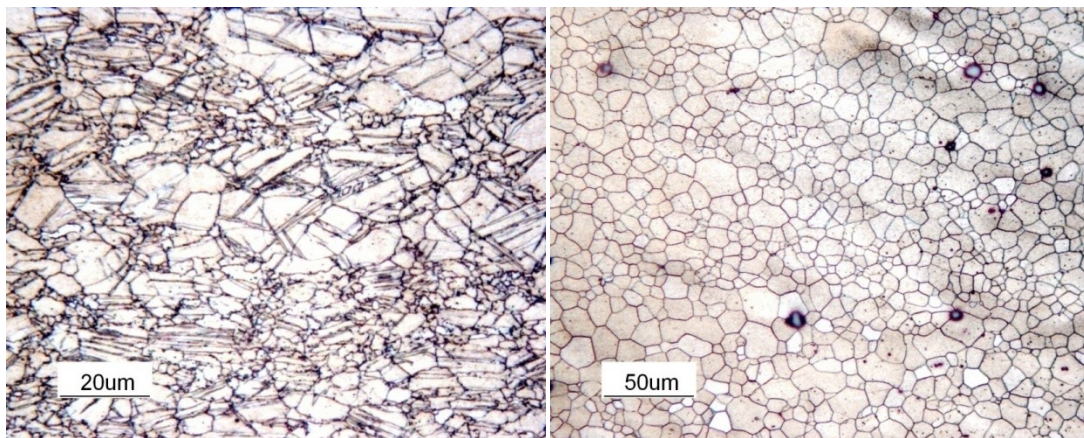


Figure 4.1: Photomicrographs of (a) the as-received AZ31 sheet microstructure and (b) the microstructure after annealing at 450°C in salt for 80 s are shown.

4.2. TENSILE TESTS

4.2.1. Tensile Test Procedure

Dog-bone-shaped tensile coupons were machined by electrical discharge machining from the Mg AZ31 sheet with a (straight) gage length of 25 mm, a gage width of 6 mm, a shoulder radius of 3 mm, and a thickness equal to the as-received sheet thickness of 2 mm. All coupons were produced with the tensile direction (TD) parallel to the rolling direction (RD) of the sheet. Figure 4.2 shows an example of an untested tensile coupon. A finite-element-method analysis, described in Appendix A, was performed to confirm that accurate R-values can be measured from this specimen geometry.

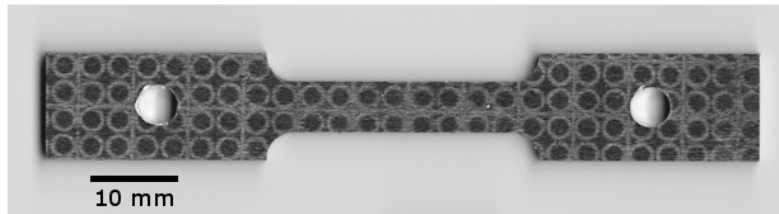


Figure 4.2: An untested AZ31 tensile coupon is shown.

The tensile tests of the AZ31 sheet material were conducted using a computer-controlled servohydraulic test frame with an attached three-zone resistance furnace. A photograph of this apparatus is shown as Figure 4.3. The furnace was preheated to 450°C, the test temperature for all specimens, prior to testing. Before each test, the initial width, w_o , and thickness, t_o , of the tensile coupon's gage region was measured using calipers. The uncertainty of these measurements was taken to be half of the caliper's smallest scale division, or 0.0005 inches. The tensile coupon was engraved with a unique specimen

designation, and shoulder-loading grips were attached to each end, as in Figure 4.4. These grips are designed so the tensile specimen can be removed quickly from the furnace after deformation. The coupon was then inserted into the furnace and allowed to reach 450°C. This process typically took approximately 20 minutes. Specimen temperature was measured using type-K thermocouples inserted into the grips to contact the specimen at both ends. After reaching 450°C, each tensile coupon was tested in tension at a constant true-strain rate ranging from 10^{-4} to 10^{-1} s^{-1} . Crosshead velocity was increased throughout each test to maintain this true-strain rate. Force and displacement were measured during each test using a load cell and a linear variable differential transformer, respectively. Deformation was imposed until a final true strain, ϵ_f , ranging from 0.14 to 0.59 was achieved. Upon completion of the test, the tensile coupon was quickly removed from the furnace and quenched in water to arrest any further microstructure evolution.

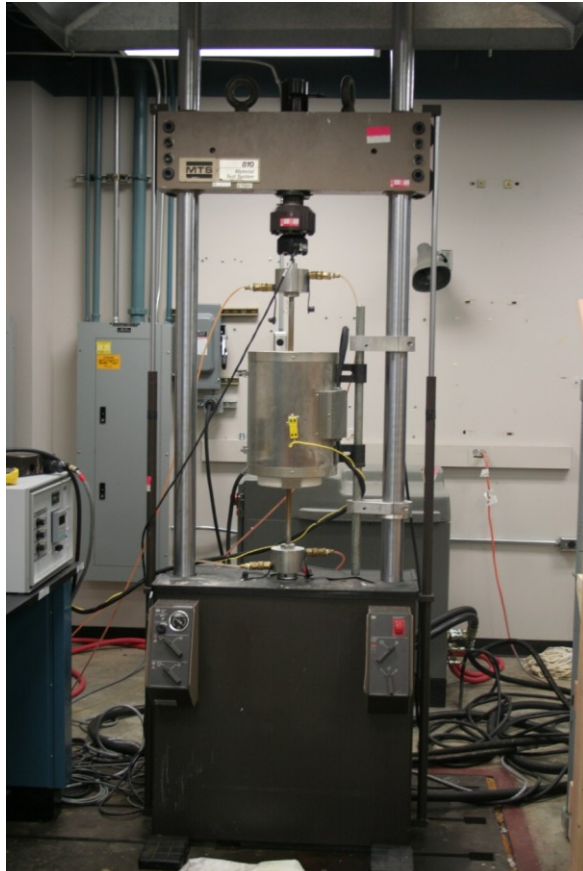


Figure 4.3: The apparatus used in tensile testing of the AZ31 sheet is shown.



Figure 4.4: The shoulder-loading grips used during tensile testing are shown.

4.2.2. Tensile Specimen Measurements

The force and displacement measurements obtained during tensile testing were used to calculate true stress, σ , and true strain, ε , throughout each test using

$$\sigma_e = \frac{F}{w_o t_o} \quad (22)$$

$$\varepsilon_e = \frac{\Delta l}{l_o} \quad (23)$$

$$\sigma = \sigma_e (1 + \varepsilon_e) \quad (24)$$

$$\varepsilon = \ln(1 + \varepsilon_e) \quad (25)$$

where σ_e is engineering stress, ε_e is engineering strain, F is force, Δl is displacement, and l_o is the initial gage length of the specimen [60]. These calculations assume conservation of volume and uniform deformation in the gage region of each specimen. These assumptions are no longer accurate after the initiation of cavitation and flow localization, which typically occurs after the AZ31 sheet material reaches a true strain of 0.6 [42]. Tensile data obtained at true strains greater than 0.6 were therefore unused in the creation of material constitutive models. Also, the stress-strain data were corrected to remove errors due to machine compliance by enforcing the known elastic modulus of Mg at 450°C, 32 GPa [61-62].

The final gage width, w_f , and thickness, t_f , were measured at five different locations along each tested specimen using a micrometer with 0.0001 inch graduations and a blade anvil. The uncertainty of any individual measurement is estimated to be ± 0.0002 inch, which is the accuracy limit that can reasonably be expected from a

micrometer with a vernier scale [63]. The results of the FEM simulations in Appendix A suggest that accurate R-values can be measured at locations further than 6 mm from the grips. Thus, no measurements were obtained within 6 mm of the grips. The final true strain in the gage region, ε_f , was calculated from area reduction using

$$\varepsilon_f = \ln \left(\frac{w_o t_o}{w_f t_f} \right) \quad (26)$$

where $w_o t_o$ is the initial cross-sectional area of the gage region prior to deformation and $w_f t_f$ is the cross-sectional area of the gage region after deformation. An average true strain was calculated from the five ε_f measurements along each specimen. At each of the five locations, anisotropy was quantified through use of the Lankford coefficient, or R-value [64]. The effective R-value, r_{eff} , was calculated using

$$r_{eff} = \frac{\varepsilon_{LD}}{\varepsilon_{SD}} = \frac{\ln \left(\frac{w_o}{w_f} \right)}{\ln \left(\frac{t_o}{t_f} \right)} \quad (27)$$

where ε_{LD} is the true strain in the long-transverse direction (across the width of the specimen) and ε_{SD} is the true strain in the short-transverse direction (through the thickness of the specimen). This method of calculating R-values differs from the standard test method, ASTM E517 [65], provided by ASTM International for measuring R-values. ASTM E517 requires an extensometer, which cannot be used for the high-temperature testing of this study. As with the true strain measurements, an average r_{eff} was calculated from the five individual r_{eff} values for each specimen. The uncertainties of true strain, $\Delta\varepsilon_f$,

and effective R-value, Δr_{eff} , were calculated using a standard formula for propagation of uncertainty,

$$\Delta y = \sqrt{\sum \left(\frac{\partial y}{\partial x_i} \Delta x_i \right)^2} \quad (28)$$

where x_i are the variables used to calculate the parameter of interest, y , and Δx and Δy are the uncertainties of x and y , respectively [66]. $\Delta \varepsilon_f$ and Δr_{eff} are

$$\Delta \varepsilon_f = \sqrt{\left(\frac{\Delta w_o}{w_o} \right)^2 + \left(\frac{\Delta t_o}{t_o} \right)^2 + \left(\frac{\Delta w_f}{w_f} \right)^2 + \left(\frac{\Delta t_f}{t_f} \right)^2} \quad (29)$$

$$\Delta r_{eff} = \sqrt{\frac{\left(\frac{\Delta w_o}{w_o} \right)^2 + \left(\frac{\Delta w_f}{w_f} \right)^2}{\left[\ln \left(\frac{t_o}{t_f} \right) \right]^2} + \frac{\left[\ln \left(\frac{w_o}{w_f} \right) \right]^2 \left[\left(\frac{\Delta t_o}{t_o} \right)^2 + \left(\frac{\Delta t_f}{t_f} \right)^2 \right]}{\left[\ln \left(\frac{t_o}{t_f} \right) \right]^4}} \quad (30)$$

using this approach.

Samples for metallographic examination were excised from the tensile specimens to study grain growth prior to and during deformation. From each tensile specimen, the samples were sectioned from the locations shown in Figure 4.5 using a precision cut-off machine with a diamond saw blade. The samples from each specimen were then mounted in epoxy, ground using silicon carbide paper, and polished using diamond suspensions. After a final polish with colloidal silica, the grain boundaries of the samples were revealed through a brief immersion in an acetic-picral etchant (35 mL ethanol, 5 mL H₂O, 5 mL acetic acid, and 2.1 g picric acid). Three optical photomicrographs were acquired from each sample to obtain grain size measurements. On each photomicrograph, lines

were drawn in both the horizontal and vertical directions in the image processing program ImageJ [67]. The distances between individual grain boundaries were measured along these lines. Arithmetic means of these measurements were calculated to obtain the average grain sizes, d , in the rolling (tensile), long-transverse, and short-transverse directions. The uncertainty of the grain size measurements, Δd , was determined by calculating the 95% confidence limit from the standard error of the mean, SE , using the relationship

$$\Delta d = 2 \times SE = 2 \frac{s}{\sqrt{n}} \quad (22)$$

where s is the standard deviation of the sample grain size measurements and n is the number of acquired measurements [61]. The AZ31 grains within the tensile specimen are equiaxed. Thus, a simple arithmetic average of the individual grain sizes is sufficient to characterize the microstructure. However, it is expected that the AZ31 grains are no longer equiaxed after deformation, and the directional measurements are therefore required to characterize the grain morphology in the gage region. An effective grain size, \bar{d} , was calculated by taking the geometric mean of the average grain size measurements in the rolling (tensile) (d_{RD}), long-transverse (d_{LD}), and short-transverse (d_{SD}) directions, as recommended by ASTM standard E112 [68]. The uncertainty of this effective grain size was calculated from the uncertainties of the individual grain size measurements using Equation 28. $\Delta \bar{d}$ is

$$\Delta \bar{d} = \sqrt{\frac{d_{LD}^2 d_{SD}^2 \Delta d_{RD}^2 + d_{RD}^2 d_{SD}^2 \Delta d_{LD}^2 + d_{RD}^2 d_{LD}^2 \Delta d_{SD}^2}{9(d_{RD} d_{LD} d_{SD})^{4/3}}} \quad (32)$$

using this method.

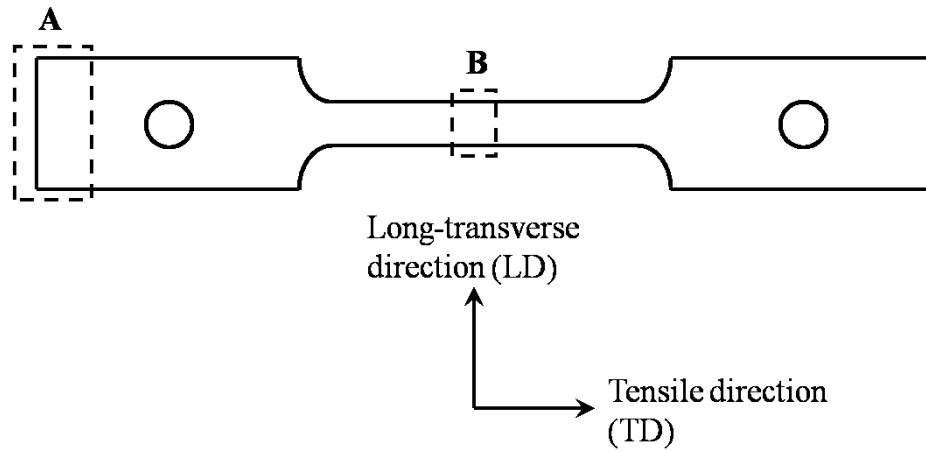


Figure 4.5: Metallographic samples were sectioned from (A) the grip and (B) the gage region of each tensile specimen. The short-transverse direction (SD) of the specimen is perpendicular to the sheet. The tensile direction (TD) is also the rolling direction (RD) of the sheet.

4.3. GAS-PRESSURE BULGE TESTS

4.3.1. The University of Texas Bulge Test Procedure

Many of the biaxial gas-pressure bulge specimens of this study were formed in a bulge testing apparatus located at The University of Texas at Austin. This apparatus was designed to acquire *in situ* measurements of dome height during deformation [69]. A photograph of the University of Texas bulge testing apparatus is shown as Figure 4.6.

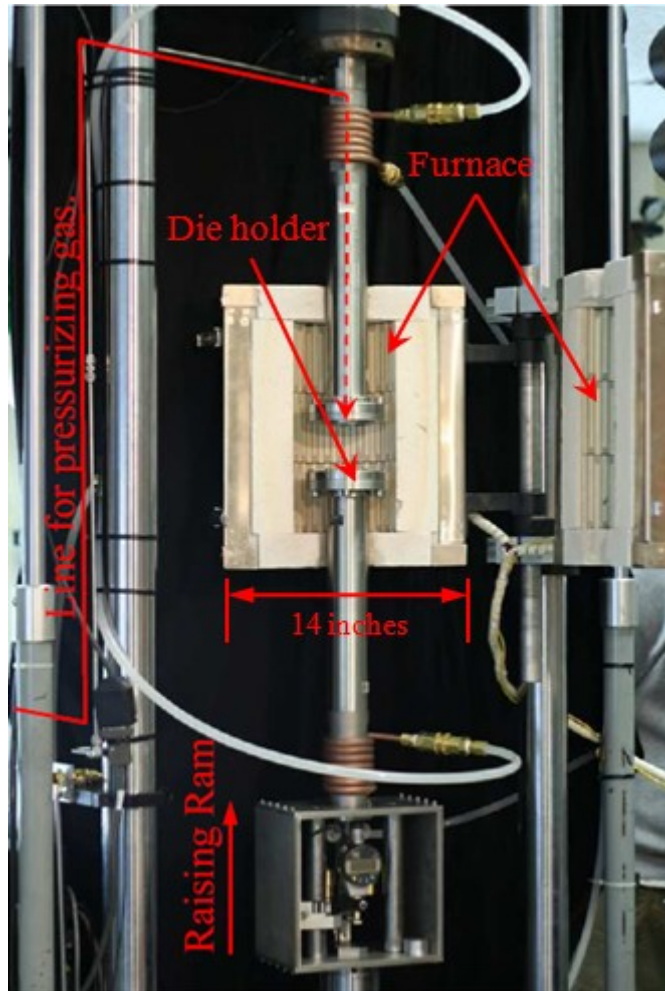


Figure 4.6: A photograph of the University of Texas bulge testing apparatus is shown. The photograph is from Ref. 69.

Specimen blanks were machined from the Mg AZ31 sheet with a diameter of 90 mm and the as-received sheet thickness of 2 mm. An example blank is shown on the left side of Figure 4.7. The bulge tester's furnace was preheated to 450°C prior to testing. A K-type thermocouple placed near the die holder monitored the temperature during testing. Before each test, SAF-T-EZE[®] anti-seize coating was applied to the upper and lower die contact regions of an AZ31 blank, and the blank was placed in the die holder. The

loading ram was then raised to clamp the upper and lower dies together with a force of approximately 3000 lbs. After clamping, the blank was preheated for a time ranging from 0 to 960 s. A constant gas pressure ranging from 550 to 1100 kPa was then applied to the top of the blank. This gas pressure caused the blank to form downward into the lower die, which is a cylinder with an inner diameter of 55.4 mm and an entry radius of 1.5 mm. As the blank formed into a dome shape, it displaced a rod attached to a digital micrometer. The digital micrometer connects to a computer, and captures approximately five dome height measurements per second. The maximum height measurable in the bulge tester is approximately 25 mm. Once the bulge specimen reached this height, the loading ram was lowered and the specimen was removed and allowed to air cool. An example formed specimen is shown on the right side of Figure 4.7. Further information about the test procedure is provided in Ref. 69.



Figure 4.7: An example specimen blank used in bulge testing (left) and dome formed from the University of Texas apparatus (right) are presented.

4.3.2. General Motors Bulge Test Procedure

Additional gas-pressure bulge specimens were formed in a bulge tester located at the General Motors Technical Center. This apparatus contains a cylindrical die with an inner diameter of 100 mm and an entry radius of 5 mm. A photograph of this die is shown in Figure 4.8. AZ31 specimen blanks were produced using a sheet metal shear for use in these biaxial gas-pressure bulge tests. The blanks were squares with sides of approximately 200 mm. Before testing, the furnace was preheated to 450°C. A K-type thermocouple inserted into a port on the upper die monitored temperature during testing. Prior to each test, a specimen blank was inserted between the upper and lower dies. The dies were then clamped together using gas pressure to form a tight seal, and the blank was preheated for a time ranging from 0 to 660 seconds. Upon the completion of preheating, a constant gas pressure ranging from 280 to 520 kPa was applied to the bottom of the specimen blank, causing it to form into the upper die. After forming for a set time, the dies were unclamped and the formed dome was removed and allowed to air cool. After cooling, the dome height and pole thickness of the specimen were measured. Dome heights were obtained using a stand specially built by General Motors for that purpose, while pole thicknesses were measured using a magnetic thickness gauge.



Figure 4.8: The furnace and die used in biaxial gas-pressure bulge tests at General Motors are shown.

Further experiments were performed to study the effects of initial grain size on the deformation behavior of the AZ31 sheet material. These experiments were conducted by Aravindhya Antoniswamy. First, the as-received sheet was statically annealed at 350°C for 15 minutes. This annealing treatment resulted in a fully recrystallized microstructure with an average grain size of 6.68 μm . Second, the thickness of the annealed sheet was reduced by 3% through cold rolling, resulting in a final thickness of 1.94 mm. The rolled sheet was further annealed at 350°C for 15 minutes, which resulted in an average grain size of 19.7 μm . Sheets with these two new initial grain sizes were then tested in the General Motors bulge tester at 280 and 520 kPa.

Chapter 5: Static and Dynamic Grain Growth

5.1. GRAIN GROWTH LAWS

5.1.1. Static Grain Growth

The mobility of grain boundaries within a material is highly temperature-dependent [70]. At high temperatures, enhanced grain boundary mobility can produce grain growth, which reduces the overall energy in a material through a reduction in the number of atoms adjacent to a grain boundary. These atoms have higher energies than atoms within the lattice of an individual grain. Static grain growth therefore leads to an increase in the average grain size.

Burke and Turnbull [71] modeled the kinetics of static grain growth by assuming that the curvature of a grain boundary, $1/R$, where R is the radius of curvature, is proportional to the driving pressure, P , on the boundary, such that

$$P = \frac{\alpha\gamma_b}{R} \quad (34)$$

where α is a proportionality constant and γ_b is the energy of the boundary. If this driving pressure is proportional to the boundary velocity, $\frac{dR}{dt}$, and the average radius of curvature is equal to the average grain size due to static grain growth, d_s , then it follows that

$$d_s^2 - d_o^2 = Ct \quad (35)$$

where d_o is the initial grain size of the material, C is constant for a particular material and temperature, and t is the time at temperature. The grain size exponent, N , for many

materials is often larger than the value of 2 shown in Equation 35 [72]. Thus, a more general static grain growth law can be written as

$$d_s = \left(d_o^N + Ct\right)^{1/N} \quad (36)$$

Equation 36 reduces to

$$d_s = Ct^{1/N} \quad (37)$$

if d_s is much larger than d_o . Thus, for a particular material at a constant temperature, d_s can be approximated solely as a function of time at temperature, t .

5.1.2. Dynamic Grain Growth

During high-temperature deformation, the grain size of a material may increase beyond that of a material statically annealed for the same time at the same temperature. This phenomenon is termed dynamic, or strain-enhanced, grain growth. There are some models describing dynamic grain growth in the literature, particularly for superplastic materials. Typically, these models treat static and dynamic grain growth as independent mechanisms, and they assume that the dynamic grain growth rate is proportional to the strain rate during deformation. Thus, the increase in grain size due to dynamic grain growth is typically assumed to be a function of strain.

Wilkinson and Cáceres [73-74] investigated the effects of superplastic deformation on grain growth for a variety of alloys. They observed that the increase in grain size due to dynamic grain growth is often proportional to the applied strain over a range of true-strain rates. They proposed a relationship where the dynamic grain growth

rate, \dot{d}_ε , normalized by the initial grain size, d_o , is proportional to true-strain rate, $\dot{\varepsilon}$, such that

$$\dot{d}_\varepsilon = \alpha d_o \dot{\varepsilon} \quad (38)$$

where α is a proportionality parameter. This relationship can be integrated to obtain

$$d = d_s + \alpha d_o \varepsilon \quad (39)$$

where d is the final average grain size after deformation and d_s is the grain size solely due to static annealing, which can be calculated from Equation 36 or 37.

Seidensticker and Mayo [75] proposed a similar model to the one developed by Wilkinson and Cáceres. However, they normalized the dynamic grain growth rate by the final grain size, d , rather than by the initial grain size, d_o , as they believed that d is a more accurate estimate of the average grain size during deformation than d_o . Thus, the model investigated by Seidensticker and Mayo is

$$\frac{d - d_s}{d} = \alpha \varepsilon \quad (40)$$

Equation 40 can be rearranged to obtain a model for d of the form

$$d = \frac{d_s}{1 - \alpha \varepsilon} \quad (41)$$

Again, d_s can be calculated from Equation 36 or 37.

Sato *et al.* [76] and Kim *et al.* [77] developed a model with the assumption that the contributions from static and dynamic grain growth can be added together to estimate the final grain size. Assuming a constant true-strain rate, they concluded that the final grain size after deformation, d , is described by

$$d^N + \frac{C}{N\alpha\dot{\epsilon}} = \left(d_o^N + \frac{C}{N\alpha\dot{\epsilon}} \right) \exp(\alpha N \epsilon) \quad (42)$$

where d_o , C , and N are the same as in Equation 35 and α is a constant describing dynamic grain growth. Sato *et al.* proposed an approximation to Equation 42,

$$d = d_s \exp(\alpha \epsilon) \quad (43)$$

while Kim *et al.* proposed the approximation

$$d = d_s + d_o [\exp(\alpha \epsilon) - 1] \quad (44)$$

In Equations 43 and 44, d_s is the grain size expected solely from static grain growth.

5.2. GRAIN SIZE MEASUREMENTS

5.2.1. Summary of Results

The grain size measurements from each of the tensile specimens are summarized in Table 5.1. For each specimen, the average grain size in the gage region was larger than the average grain size in the grip region. This indicates that the gage regions of all specimens experienced dynamic grain growth during deformation. The observed dynamic grain growth was typically normal, i.e. all grains generally grew at similar rates. However, abnormally large grains were observed in the gage region of two specimens tested at the fastest strain rate of $3 \times 10^{-2} \text{ s}^{-1}$. An example of one of these abnormal grains is shown in Figure 5.1. At $3 \times 10^{-2} \text{ s}^{-1}$, DC creep is expected to almost completely control deformation, as indicated by Figure 2.5. Because DC creep is not affected by grain size [56], abnormal grain growth is not expected to significantly affect the deformation behavior of the AZ31 sheet. Thus, the growth of abnormal grains was ignored in the

subsequent analysis, and the gage region grain sizes in Table 5.1 only represent the effects of dynamic normal grain growth.

Table 5.1: Grain size and true strain measurements, along with their respective uncertainties, are presented for each tensile specimen examined. Specimens designated with a * developed some abnormal grains in the gage region.

True-Strain Rate (s^{-1})	Specimen Designation	True Strain, ϵ_f	Grip region grain size, d_s (μm)	Gage region grain size, d (μm)
10^{-4}	GM28	0.14 ± 0.01	10.6 ± 0.7	11.2 ± 0.7
	GM22	0.30 ± 0.01	12.6 ± 0.9	14.4 ± 0.9
	GM25	0.47 ± 0.01	12.7 ± 0.9	17.5 ± 1.2
3×10^{-4}	GM29	0.15 ± 0.01	10.5 ± 0.8	11.0 ± 0.7
	GM31	0.32 ± 0.01	12.7 ± 1.0	13.7 ± 1.0
	GM24	0.49 ± 0.01	12.1 ± 0.9	16.6 ± 1.2
10^{-2}	GM26	0.17 ± 0.01	9.9 ± 0.6	10.1 ± 0.5
	GM33	0.37 ± 0.01	10.4 ± 0.9	12.3 ± 0.8
	GM27	0.57 ± 0.01	10.2 ± 0.6	12.5 ± 0.7
3×10^{-2}	GM30	0.18 ± 0.01	8.7 ± 0.6	10.8 ± 0.6
	GM23*	0.39 ± 0.01	9.2 ± 0.5	11.0 ± 0.6
	GM32*	0.59 ± 0.01	10.7 ± 0.8	16.0 ± 2.4

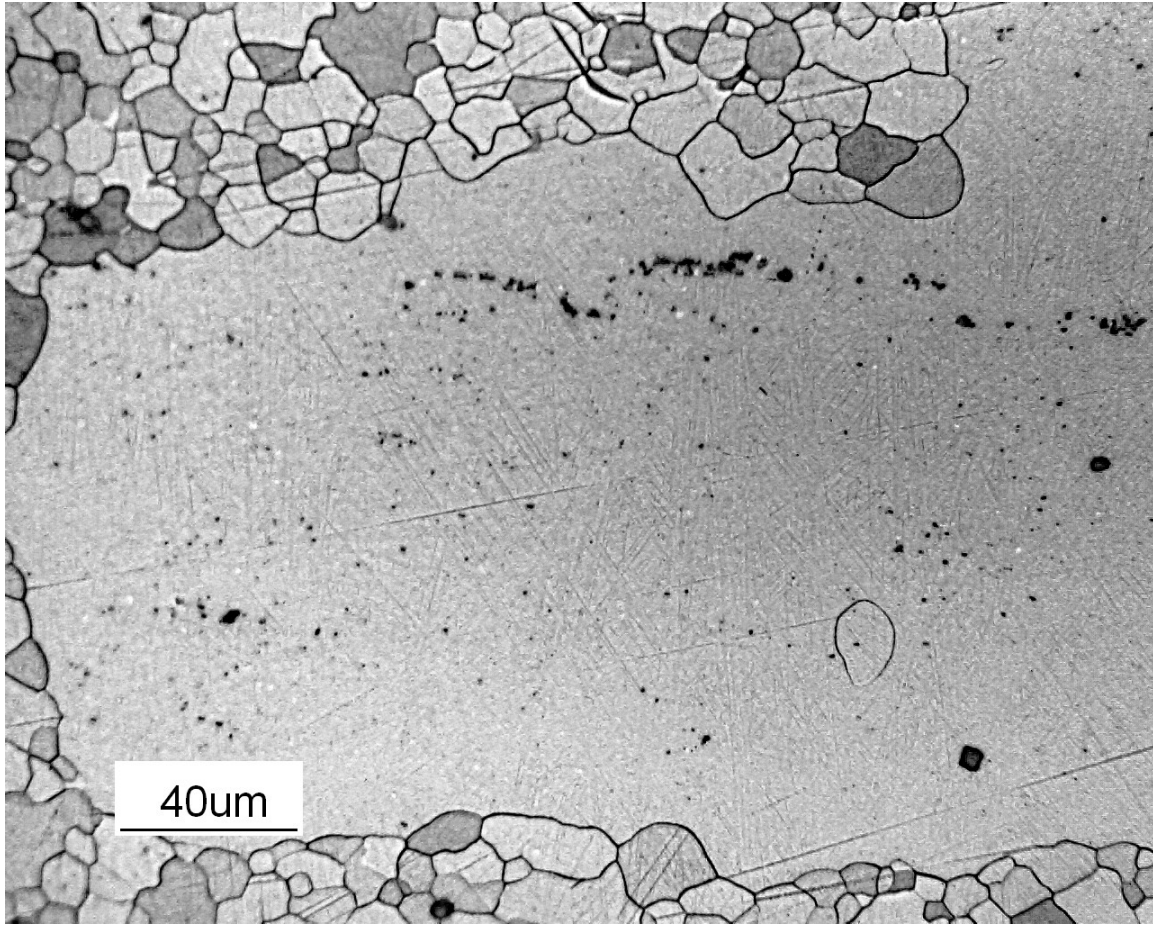


Figure 5.1: A photomicrograph containing an example of an abnormally large grain is shown. This abnormal grain was observed in the gage region of the tensile specimen tested at $3 \times 10^{-2} \text{ s}^{-1}$ to a final true strain of 0.39.

5.2.2. Static Grain Growth

Grain sizes, d_s , in the undeformed grip region were plotted against time, t , for each test condition. These measurements, shown as open circles in Figure 5.2, illustrate the effects of time at temperature on static grain growth of the AZ31 sheet. The error bars on d_s represent the uncertainties calculated from the standard errors on the average grain size measurements. Equations 36 and 37 were fit to the experimental open circles shown

in Figure 5.2 using the NonlinearModelFit routine in the computational software program Mathematica[®] [78]. The fitting parameters C and N were chosen to minimize the sum of the squares of the differences between the fitted equation and the experimental data. Note that the initial grain size of the AZ31 sheet (d_o in Equation 35) cannot be directly measured. This is because the as-received sheet is provided in a partially-annealed, unrecrystallized condition. However, the material recrystallizes to equiaxed grains quickly at 450°C. The tensile specimen tested at $3 \times 10^{-2} \text{ s}^{-1}$ to a true strain of 0.18, which represents the fastest tensile test conducted for this study, recrystallized equiaxed grains with an average size of 8.7 μm in the grip region. This grain size was used as an estimate of the “initial” grain size of the AZ31 sheet after recrystallization, d_o , in Equation 36. Values of C and N obtained from the fits of Equations 36 and 37 are shown in Table 5.2. The fits themselves are plotted as curves in Figure 5.2. Equations 36 and 37 both provide reasonable agreement with the grain size data. However, Equation 37 predicts that $d_s = 0$ for $t = 0$. A grain-size dependent material model, describing the strain-rate due to GBS creep using Equation 18, would therefore predict an infinitely large value of $\dot{\epsilon}_{GBS}$ as forming begins, which is clearly nonphysical. Therefore, Equation 36 is used to model static grain growth in subsequent analyses. Figure 5.2 also shows the average grain size measured from AZ31 specimens annealed in salt at 450°C for various times. These data are presented as closed circles. Although these additional data were not used in fitting, they confirm that the grip grain sizes are consistent with exposure to 450°C for the specified times.

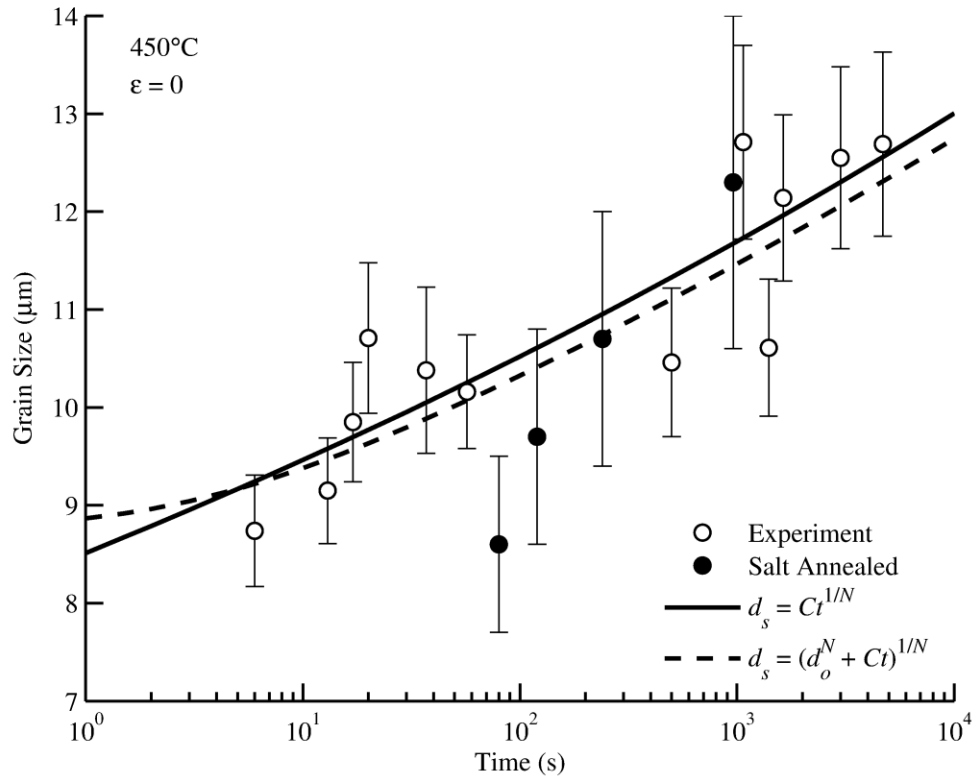


Figure 5.2: The average grain size in the undeformed grip region, d_s , is plotted against time, t , for tensile specimens tested at 450°C and constant true-strain rates ranging from 10^{-4} to $3 \times 10^{-2} \text{ s}^{-1}$. Experimental data are shown as open circles, while fits to the data using Equations 36 and 37 are shown as curves. The closed circles are grain size measurements from specimens annealed in salt at 450°C.

Table 5.2: The parameters obtained from fitting the static grain growth models to experimental data are provided. The value of d_o was assumed to be 8.7 μm, which was the smallest grain size measured in the grip regions of the tensile specimens.

Fitting Parameter	$d_s = Ct^{1/N}$	$d_s = (d_o^N + Ct)^{1/N}$
$C (\mu\text{m s}^{-N})$	8.5	1.1×10^{20}
N	22	22

5.2.3. Dynamic Grain Growth

The grain size, d , in the deformed gage region measured from the tensile specimens represents the combined effects of both static and dynamic grain growth. The four models for dynamic grain growth can be divided into two types. The models proposed by Wilkinson and Cáceres (Equation 39) and Kim *et al.* (Equation 44) suggest that the *difference* between d and the grip region grain size, d_s , is a function of true strain, ε . The models proposed by Seidensticker and Mayo (Equation 41) and Sato *et al.* (Equation 43) suggest that the *ratio* between d and the grip region grain size, d_s , is a function of true strain, ε .

Figure 5.3 shows the measurements of $d - d_s$ from the tensile specimens plotted as markers against ε . The error bars were calculated from the individual uncertainties Δd and Δd_s on d and d_s , respectively. The uncertainty $\Delta(d - d_s)$ is given by Equation 28 [66], such that

$$\Delta(d - d_s) = \sqrt{(\Delta d)^2 + (\Delta d_s)^2} \quad (45)$$

The Wilkinson-Cáceres and Kim *et al.* models were fit to the experimental data shown in Figure 5.3 using the NonlinearModelFit routine in the computational software program Mathematica[®] [78]. The fitting parameter α was chosen to minimize the sum of the squares of the differences between the fitted equation and the experimental data, and d_o was again assumed to be 8.7 μm . The fitted values of α are provided in Table 5.3. The Wilkinson-Cáceres and Kim *et al.* fits are plotted as curves in Figure 5.3.

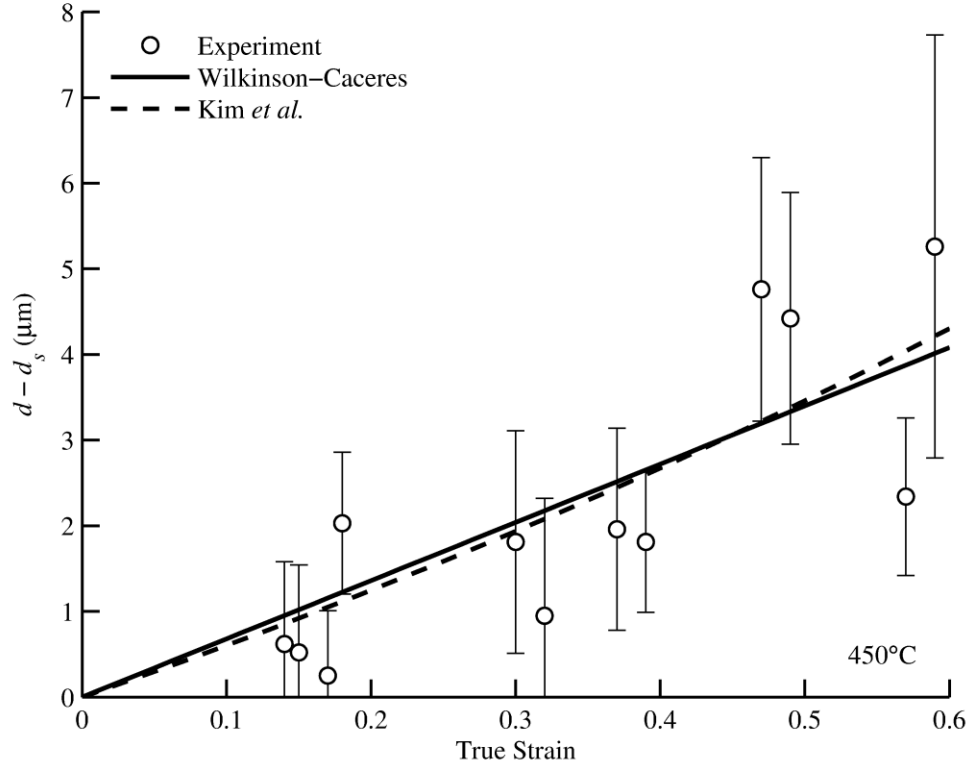


Figure 5.3: The difference in average grain size between the gage region and grip region after tensile deformation, $d - d_s$, is plotted against true strain, ϵ . The experimental measurements, which are shown as markers, were obtained from tensile specimens tested at 450°C and constant true-strain rates ranging from 10^{-4} to $3 \times 10^{-2} \text{ s}^{-1}$. Fits to the data using the Wilkinson-Cáceres and Kim *et al.* models are shown as curves.

Table 5.3: The values of α obtained from fitting the dynamic grain growth models to experimental data are provided. The value of d_o was assumed to be 8.7 μm , which was the smallest grain size measured in the grip region of the tensile specimens.

Model	α
Wilkinson-Cáceres	0.78
Kim <i>et al.</i>	0.67
Seidensticker-Mayo	0.48
Sato <i>et al.</i>	0.54

Figure 5.4 shows the measurements of d/d_s from the tensile specimens plotted as markers against ε . Again, the error bars were calculated from the individual uncertainties Δd and Δd_s on d and d_s , respectively. The uncertainty $\Delta(d/d_s)$ is given by Equation 28 [66], such that

$$\Delta\left(\frac{d}{d_s}\right) = \sqrt{\left(\frac{\Delta d}{d}\right)^2 + \left(\frac{\Delta d_s}{d_s}\right)^2} \quad (46)$$

The Seidensticker-Mayo and Sato *et al.* models were fit to the experimental data shown in Figure 5.4 using the NonlinearModelFit routine in the computational software program Mathematica[®] [78]. Again, the fitting parameter α was chosen to minimize the sum of the squares of the differences between the fitted equation and the experimental data. The fitted values of α are also provided in Table 5.3. The Seidensticker-Mayo and Sato *et al.* fits are plotted as curves in Figure 5.4.

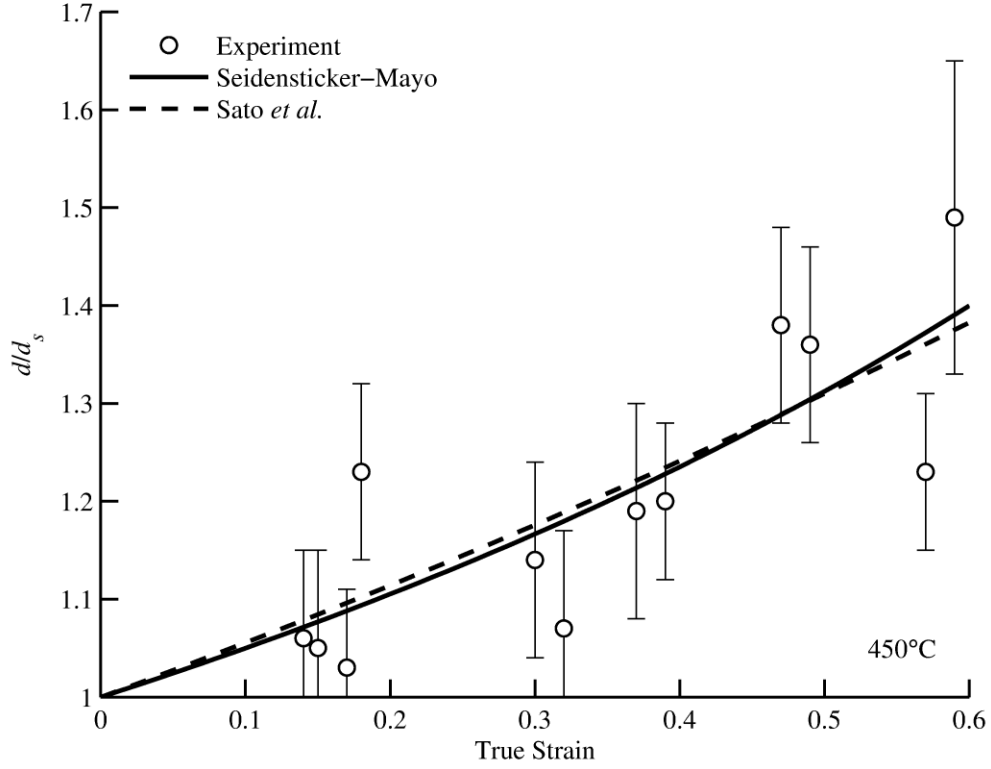


Figure 5.4: The ratio of average grain size between the gage region and grip region after tensile deformation, d/d_s , is plotted against true strain, ϵ . The experimental measurements, which are shown as markers, were obtained from tensile specimens tested at 450°C and constant true-strain rates ranging from 10^{-4} to $3 \times 10^{-2} \text{ s}^{-1}$. Fits to the data using the Seidensticker-Mayo and Sato *et al.* models are shown as curves.

Figures 5.3 and 5.4 indicate that all four dynamic grain growth models provide reasonable agreement with the experimental grain size measurements. Although it is difficult to quantitatively compare the models in Figure 5.3 to those in Figure 5.4, the two models within each figure can be compared to each other by calculating the root-mean-square (RMS) error, x_{RMS} , given by

$$x_{RMS} = \sqrt{\frac{1}{n} \sum_{i=1}^n (x_{\text{exp}} - x_{\text{mod}})^2} \quad (47)$$

where n is the number of experimental measurements, x_{exp} is an experimentally-determined measurement (in this case the difference $(d - d_s)$ or ratio (d/d_s) between the gage region and grip region grain size), and x_{mod} is the corresponding value predicted by a mathematical model. The RMS error for the Wilkinson-Cáceres model is 1.00 μm , while the RMS error for the Kim *et al.* model is 0.97 μm . This indicates that the Wilkinson-Cáceres and Kim *et al.* models have similar accuracies. The RMS error for the Seidensticker-Mayo model is 0.081, while the RMS error for the Sato *et al.* model is 0.082, which indicates that the Seidensticker-Mayo and Sato *et al.* models also have similar accuracies. These RMS errors, along with a qualitative comparison of Figures 5.3 and 5.4, suggest that all four dynamic grain growth models provide similar utility. Thus, all four models were considered in the subsequent analysis.

5.3. A GRAIN-SIZE DEPENDENT MATERIAL MODEL

A static grain growth model, such as Equation 36, can be combined with a dynamic grain growth model to create a model for grain size, d , that is a function of both time, t , and strain, ε . Recall that GBS creep depends on grain size as described by Equation 18, while DC creep is independent of grain size as described by Equation 19 [56-57]. Because GBS creep and DC creep are the two independent mechanisms governing deformation, the relationship between true-strain rate, $\dot{\varepsilon}$, and true stress, σ , is therefore given by the sum of Equations 18 and 19,

$$\dot{\varepsilon} = \frac{A_{GBS}}{d(\varepsilon, t)^p} \sigma^{n_{GBS}} + A_{DC} \sigma^{n_{DC}} \quad (48)$$

where A_{GBS} , n_{GBS} , and p are parameters that describe GBS creep; A_{DC} and n_{DC} are parameters that describe DC creep; and d is the average grain size, which is calculated using Equation 36 and one of the dynamic grain growth models.

For all four dynamic grain growth models, Equation 48 was fit to the same tensile data used to create the SDTD material constitutive model. During that investigation [42], it was determined that the experimental data could be modeled by a Voce-type strain-hardening law [79],

$$\sigma = \sigma_o + a(1 - \exp(-c\varepsilon)) \quad (49)$$

for each true-strain rate ranging from 10^{-4} to $3 \times 10^{-3} \text{ s}^{-1}$ and true strains ranging from 0 to 0.6. In Equation 49, σ represents the flow stress at a particular strain ε , σ_o represents the expected flow stress due to plastic deformation at $\varepsilon = 0$, and a and c are constants for a particular temperature and strain rate. For true-strain rates ranging from 10^{-2} to 10^{-1} s^{-1} , σ was approximately constant for true strains ranging from 0 to 0.6. The Voce law parameters for strain rates from 10^{-4} to $3 \times 10^{-3} \text{ s}^{-1}$ and the mean flow stress σ_m for strain rates from 10^{-2} to 10^{-1} s^{-1} are listed in Table 5.4. The values in Table 5.4 are average parameters determined from tensile tests at orientations of 0, 45, and 90° relative to the rolling direction. The average parameters are sufficient because the stress-strain behavior is nearly identical between specimen orientations at all strain rates [42]. At 10^{-2} s^{-1} and faster, σ is constant, which suggests no hardening from grain growth, implying that deformation is almost completely due to DC creep. Values for A_{DC} and n_{DC} were therefore determined by fitting Equation 19 to the data obtained at 10^{-2} s^{-1} and faster to minimize the sum of the squares of the differences between the fitted equation and the

experimental data. Next, the flow stress, σ , was calculated using Equation 49 (10^{-4} to $3 \times 10^{-3} \text{ s}^{-1}$) or assumed to be constant (10^{-2} to 10^{-1} s^{-1}) for each of the seven tested true-strain rates and true strains from 0 to 0.6 in increments of 0.1. For each of these 49 values, d was then calculated from Equation 36 and one of the dynamic grain growth models, where $t = \varepsilon / \dot{\varepsilon}$ for a constant true-strain rate test. Equation 48 was then fit to the data using the NonlinearModelFit routine in the computational software program Mathematica[®] [78]. Values of A_{GBS} , n_{GBS} , and p were chosen to minimize the sum of the squares of the differences between the fitted equation and the experimental data. The RMS errors of each of the four resulting material models were then calculated on the base 10 logarithm of true-strain rate using Equation 47.

Table 5.4: The parameters resulting from fits to tensile data of AZ31 sheet at 450°C are presented. Data from true-strain rates ranging from 10^{-4} to $3 \times 10^{-3} \text{ s}^{-1}$ followed the Voce strain-hardening law (Equation 49). At true-strain rates ranging from 10^{-4} to $3 \times 10^{-3} \text{ s}^{-1}$, the flow stress exhibited a nearly constant value of σ_m for strains ranging from 0 to 0.6. The values in the table are from Ref. 42.

True-strain rate, (s^{-1})	σ_o (MPa)	a (MPa)	c	σ_m (MPa)
10^{-4}	1.77	7.18	2.18	-
3×10^{-4}	4.03	6.58	3.49	-
10^{-3}	8.82	4.69	4.60	-
3×10^{-3}	14.4	1.99	6.47	-
10^{-2}	-	-	-	20.3
3×10^{-2}	-	-	-	24.8
10^{-1}	-	-	-	30.3

The resulting RMS errors are summarized in Table 5.5. The material constitutive model created using the Seidensticker-Mayo dynamic grain growth model has the lowest RMS error, which indicates that it best describes the experimental tensile data. However,

the Seidensticker-Mayo model has a singularity at $\varepsilon = 2.1$. At this strain, d becomes infinite, and the model predicts a negative grain size for larger strains, which is clearly unphysical. The material constitutive model created using the Sato *et al.* dynamic grain growth model has the next lowest RMS error, which is identical to that of the Seidensticker-Mayo model for all practical purposes. Thus, the Sato *et al.* model is chosen for use in the resulting grain-size dependent tensile data (GDTD) material constitutive model. The final grain size model, created by combining Equations 36 and 43, is

$$d = \left(d_o^N + Ct \right)^{1/N} \exp(\alpha \varepsilon) \quad (50)$$

The parameters d_o , C , N , and α are summarized in Table 5.6.

Table 5.5: The RMS errors on the base 10 logarithms of true-strain rate are presented for four material constitutive models. Each material model was created using one of the investigated dynamic grain growth models. All material models are given by the form of Equation 48.

Dynamic Grain Growth Model	Corresponding Material Model RMS Error
Wilkinson-Cáceres	0.038
Kim <i>et al.</i>	0.037
Seidensticker-Mayo	0.035
Sato <i>et al.</i>	0.036

Table 5.6: The parameters describing the final grain size model are presented. The grain size model is described by the form of Equation 50.

Parameter	Final Grain Size Model
d_o (μm)	8.7
C ($\mu\text{m s}^{-N}$)	1.1×10^{20}
N	22
α	0.54

The parameters describing the GDTD material constitutive model are presented in Table 5.7. Figure 5.5 compares the GDTD model against the experimentally-determined tensile data used in fitting. The logarithm of true strain rate is plotted against the logarithm of true stress for both the experimental data, shown as markers, and the GDTD model, shown as curves for true strains ranging from 0 to 0.6. The figure indicates that the GDTD model accurately describes the tensile data. Unlike previous material models, such as the SDTD model, the GDTD model has a physical basis behind all of the terms within the model. The GDTD model accurately describes the experimental tensile data, which suggests that the model accounts for the most important mechanisms controlling deformation. The GDTD model also relates the deformation behavior of the AZ31 sheet to the average grain size within the material, which provides further evidence that GBS creep is responsible for deformation at slow strain rates.

Table 5.7: The parameters describing the GDTD material constitutive model are presented. The material model is described by the form of Equation 48.

Parameter	GDTD Material Model
$A_{GBS} (\text{s}^{-1} \text{MPa}^{-n_{GBS}} \mu\text{m}^p)$	0.048
n_{GBS}	1.3
p	3.1
$A_{DC} (\text{s}^{-1} \text{MPa}^{-n_{DC}})$	3.1×10^{-10}
n_{DC}	5.7

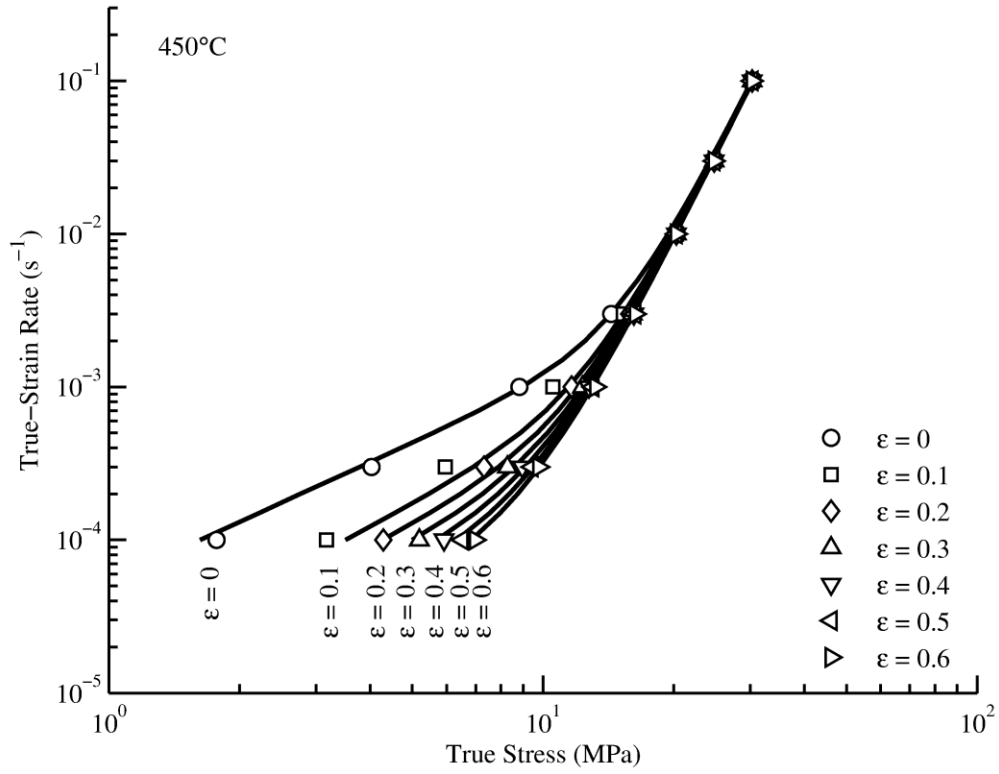


Figure 5.5: The logarithm of true-strain rate is plotted against the logarithm of true stress for AZ31 tensile specimens tested at 450°C. Markers represent tensile data, while curves represent the GDTD material model (Equation 48) fit to the data.

Chapter 6: Plastic Anisotropy

6.1. TWO-MECHANISM THEORY

It is theorized that plastic anisotropy is responsible for the observed differences between tensile and biaxial forming of AZ31 sheet [23, 41-42]. This anisotropy can be quantified using the R-values measured from tensile specimens. Note that the rolled Mg AZ31 sheet of this investigation deforms by two independent creep mechanisms at 450°C: GBS creep and DC creep. The SDTDM1 material model requires modification of the DC creep term to predict biaxial deformation. However, no such modification is required of the GBS creep term. This suggests that GBS creep is isotropic, while DC creep is anisotropic. If the two creep mechanisms independently exhibit differing amounts of normal plastic anisotropy, the effective R-value, r_{eff} , measured after deformation is expected to be a function of the individual R-values for GBS creep, r_{GBS} , and DC creep, r_{DC} . Consider the volume of AZ31 sheet material in Figure 6.1 subject to a normal stress from uniaxial loading along the z -direction such that plastic deformation occurs. This material volume is oriented such that the x -direction is normal to the plane of the sheet, in reference to a tensile coupon from the Mg AZ31 sheet material. The y -direction is along the long-transverse direction of the tensile coupon. During tensile deformation, the material will experience tensile strain along the z -direction from both GBS creep, ϵ_{GBS} , and DC creep, ϵ_{DC} . The total true strain along the z -direction, ϵ_z , is

$$\epsilon_z = \epsilon_{GBS} + \epsilon_{DC} \quad (51)$$

As ε_z increases, the material will experience negative strains along the x - and y -directions such that volume is conserved, i.e., $\varepsilon_x + \varepsilon_y + \varepsilon_z = 0$, assuming no cavitation. If GBS creep and DC creep are independent deformation mechanisms, then the true strains along the x -direction, ε_x , and y -direction, ε_y , are

$$\varepsilon_x = -\frac{1}{1+r_{GBS}}\varepsilon_{GBS} - \frac{1}{1+r_{DC}}\varepsilon_{DC} \quad (52)$$

$$\varepsilon_y = -\frac{r_{GBS}}{1+r_{GBS}}\varepsilon_{GBS} - \frac{r_{DC}}{1+r_{DC}}\varepsilon_{DC} \quad (53)$$

for constant values of r_{GBS} and r_{DC} . Thus, the material will exhibit an effective R-value, r_{eff} , of

$$r_{eff} = \frac{\varepsilon_y}{\varepsilon_x} = \frac{\frac{r_{GBS}}{1+r_{GBS}}\varepsilon_{GBS} + \frac{r_{DC}}{1+r_{DC}}\varepsilon_{DC}}{\frac{1}{1+r_{GBS}}\varepsilon_{GBS} + \frac{1}{1+r_{DC}}\varepsilon_{DC}} \quad (54)$$

which is the R-value that is measured from a tensile specimen after deformation.

Equation 54 can be simplified to

$$r_{eff} = \frac{r_{GBS}(1+r_{DC})(1-f_{DC}) + r_{DC}(1+r_{GBS})f_{DC}}{(1+r_{DC})(1-f_{DC}) + (1+r_{GBS})f_{DC}} \quad (55)$$

where f_{DC} , the fraction of DC creep strain relative to the total true strain, is

$$f_{DC} = \frac{\varepsilon_{DC}}{\varepsilon_{GBS} + \varepsilon_{DC}} \quad (56)$$

Thus, the effective R-value in a Mg AZ31 tensile specimen is expected to be a function solely of f_{DC} , assuming constant values for both r_{GBS} and r_{DC} . A similar result was obtained by Barnett *et al.* [80] for AZ31 deformation at temperatures from 25 to 250°C.

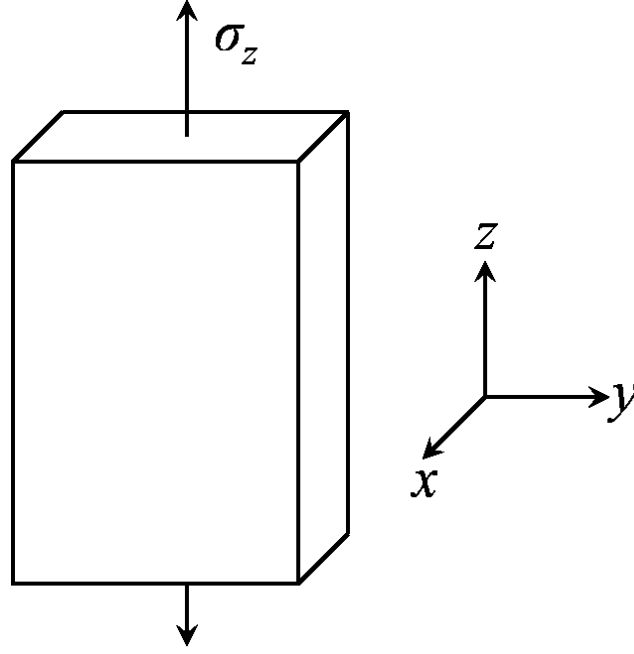


Figure 6.1: A volume of Mg AZ31 sheet is subject to a tensile stress from uniaxial loading in the z -direction. The plane of the sheet is perpendicular to the x -direction, and the tensile axis is along the z -direction.

6.2. EXPERIMENTAL R-VALUE MEASUREMENTS

The R-value and true strain measurements from the AZ31 tensile specimens, along with their uncertainties, are presented in Table 6.1. The true-strain measurements can be used to estimate the DC creep strain fraction, f_{DC} , for each specimen using the GDTD material model developed in the previous chapter. The form of the GDTD model (see Equation 48 and Table 5.7) indicates that the true-strain rates due to GBS creep, $\dot{\epsilon}_{GBS}$, and dislocation-climb creep, $\dot{\epsilon}_{DC}$, are

$$\dot{\epsilon}_{GBS} = \frac{A_{GBS}}{\left[\left(d_o^N + Ct \right)^{1/N} + \alpha d_o \epsilon \right]^p} \sigma^{n_{GBS}} \quad (57)$$

$$\dot{\varepsilon}_{DC} = A_{DC} \sigma^{n_{DC}} \quad (58)$$

For a specimen tested at a constant true-strain rate, $t = \varepsilon / \dot{\varepsilon}$. Thus, the true strains due to GBS creep, ε_{GBS} , and dislocation-climb creep, ε_{DC} , can be estimated by integrating Equations 57 and 58, respectively, to obtain

$$\varepsilon_{GBS} = \int_0^{\varepsilon_f} \frac{A_{GBS}}{\left[\left(d_o^N + Ct \right)^{1/N} + \alpha d_o \varepsilon \right]^p} \sigma^{n_{GBS}} d\varepsilon \quad (59)$$

$$\varepsilon_{DC} = \int_0^{\varepsilon_f} A_{DC} \sigma^{n_{DC}} d\varepsilon \quad (60)$$

where ε_f is the final true strain in the specimen after deformation. For each tensile specimen, ε_{GBS} and ε_{DC} were numerically calculated from Equations 59 and 60 using the trapezoidal rule with 100 equally-spaced intervals. At each integration point, σ was calculated such that the total true-strain rate, $\dot{\varepsilon}$, is equal to the true-strain rate of the tensile test. After calculating ε_{GBS} and ε_{DC} , f_{DC} was determined using Equation 56. The results of these calculations are also shown in Table 6.1.

Table 6.1: R-value and true strain measurements, along with their respective uncertainties, are presented for each tested tensile specimen. The fraction of dislocation-climb creep strain that each specimen experienced, which was estimated using the GDTD material model, is also shown.

True-Strain Rate (s^{-1})	Specimen Designation	True Strain, ϵ_f	R-value, r_{eff}	Dislocation-climb creep fraction, f_{DC}
10^{-4}	GM28	0.14 ± 0.01	1.02 ± 0.10	0.003
	GM22	0.30 ± 0.01	1.06 ± 0.05	0.010
	GM25	0.47 ± 0.01	1.08 ± 0.04	0.026
3×10^{-4}	GM29	0.15 ± 0.01	1.04 ± 0.10	0.055
	GM31	0.32 ± 0.01	1.09 ± 0.05	0.122
	GM24	0.49 ± 0.01	1.16 ± 0.04	0.192
10^{-2}	GM26	0.17 ± 0.01	1.58 ± 0.17	0.822
	GM33	0.37 ± 0.01	1.73 ± 0.09	0.859
	GM27	0.57 ± 0.01	1.69 ± 0.06	0.882
3×10^{-2}	GM30	0.18 ± 0.01	1.69 ± 0.17	0.917
	GM23	0.39 ± 0.01	1.79 ± 0.09	0.934
	GM32	0.59 ± 0.01	1.86 ± 0.06	0.945

Figure 6.2 shows r_{eff} plotted against f_{DC} . These data reveal that r_{eff} is a strong function of f_{DC} and that this dependence agrees well with Equation 55. To determine values of r_{GBS} and r_{DC} , Equation 55 was fit to the experimental data shown in Figure 6.2 using the NonlinearModelFit routine in the computational software program Mathematica[®] [78]. The values of r_{GBS} and r_{DC} were chosen to minimize the sum of the squares of the differences between the fitted equation and the experimental data. From fitting, it was determined that $r_{GBS} = 1.03 \pm 0.04$ and $r_{DC} = 1.85 \pm 0.05$. The value of r_{GBS} is very close to 1.0, which confirms that GBS creep in Mg AZ31 is isotropic. Thus, Equation 55 was refit to the data in Figure 6.2 while constraining r_{GBS} to unity. From this second fit, it was determined that $r_{DC} = 1.86 \pm 0.05$. Figure 6.2 presents a comparison of Equation 55 to the experimental measurements of r_{eff} , assuming $r_{GBS} = 1.0$ and $r_{DC} = 1.86$. This figure demonstrates that the fitted Equation 55 accurately describes the R-values

measured after tensile deformation of Mg AZ31 at 450°C. From this point forward, all analyses assume $r_{GBS} = 1.0$ and $r_{DC} = 1.86$.

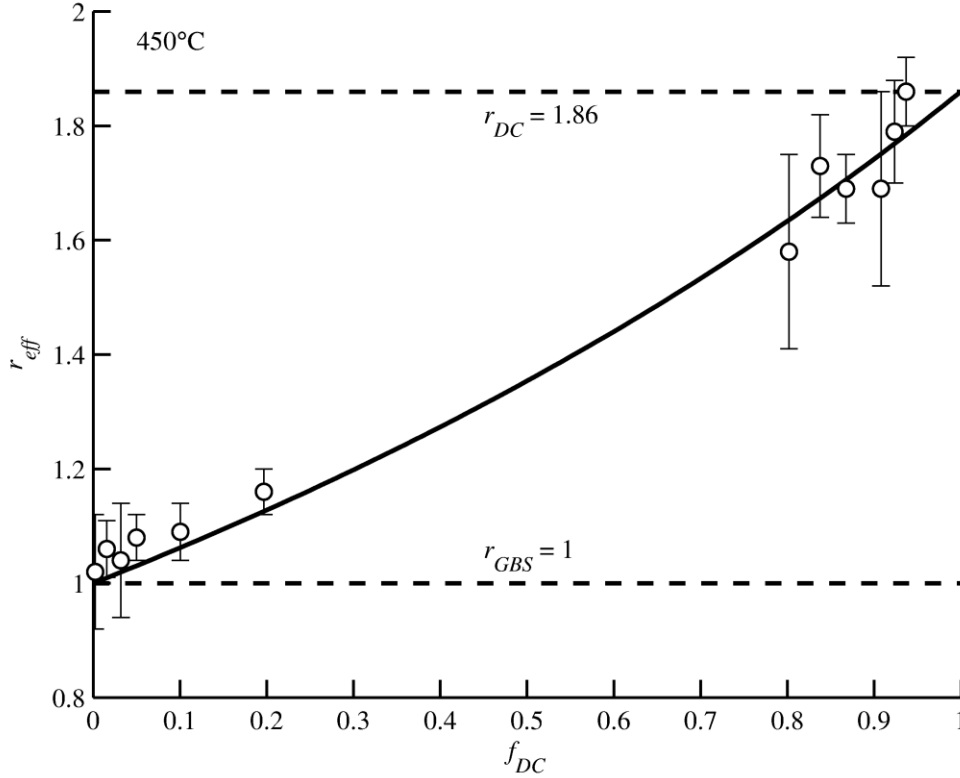


Figure 6.2: Effective R-value, r_{eff} , is plotted against the fraction of true strain from dislocation-climb creep, f_{DC} . Experimental data are plotted as markers. R-values expected from theory (Equation 55) are plotted as a solid line. Values of f_{DC} for experimental data were determined using the GDTD material model.

Figure 6.3 shows the effective R-value, r_{eff} , plotted as a function of local true strain, ϵ_f . Values of r_{eff} increase with both true-strain rate, $\dot{\epsilon}$, and local true strain, ϵ_f . This is consistent with the coexistence of two independent creep mechanisms, one isotropic and one anisotropic, controlling deformation in Mg AZ31. As $\dot{\epsilon}$ increases, the dominant deformation mechanism transitions from GBS creep to DC creep: DC creep is associated

with a larger R-value than GBS creep. Thus, r_{eff} is expected to increase with increasing $\dot{\epsilon}$, and the data of Figure 6.3 agree with this expectation. Grain size increases with increasing ϵ_f due to dynamic grain growth in AZ31 at 450°C, as shown in the previous chapter. As grain size increases with ϵ_f , the strain rate due to GBS creep rapidly decreases, and the contribution of DC creep (f_{DC}) to the overall strain rate, and to the total strain, increases. Because of this increasing importance of DC creep with increasing strain (ϵ_f) and the greater anisotropy of DC creep, r_{eff} is expected to increase with increasing ϵ_f . Again, the data of Figure 6.3 agree with this expectation. The SDTD material model was used to calculate f_{DC} for each of the four strain rates of tensile experiments over true strains from 0 to 0.6 using Equations 56, 59, and 60. Equation 55 was then used to determine the theoretical relationship between effective R-value, r_{eff} , and true strain, ϵ_f , which is shown by the curves in Figure 6.3. The values of r_{eff} predicted from theory agree reasonably well with the experimentally measured R-values.

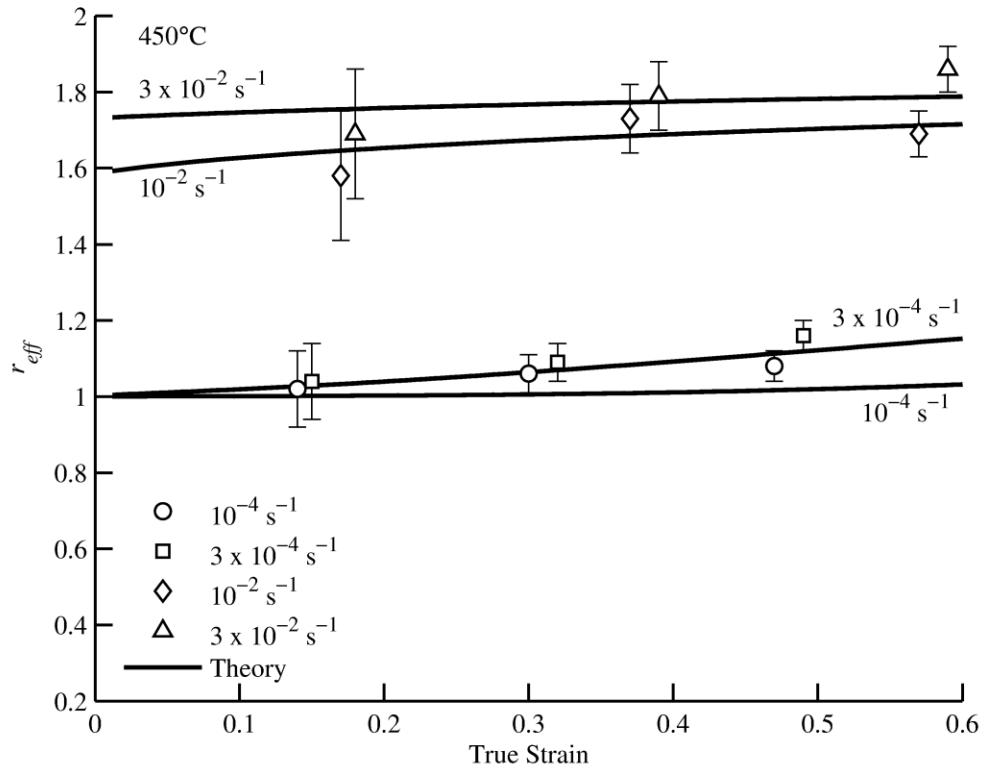


Figure 6.3: Effective R-value, r_{eff} , is plotted against final true strain, ϵ_f . Experimental data are plotted as markers. R-values expected from theory (Equation 55) are plotted as a solid line.

6.3. EFFECTS OF ANISOTROPY AND STRESS STATE ON DEFORMATION

Plastic anisotropy in AZ31 sheet at 450°C was quantified through measurements taken after tensile deformation. However, this anisotropy also affects deformation under other stress states. These effects are demonstrated through the investigation of equivalent tensile stresses, which are related to yield criteria. When generalized to any stress state, the stress variable, σ , in material models such as the 1.3 sigma model (Equation 17) and SDTD model (Equation 20) is an equivalent stress calculated from the stress tensor at the location of interest. One of the most commonly utilized equivalent stresses is the von Mises stress, σ_V ,

$$\sigma_V = \sqrt{\frac{(\sigma_{11} - \sigma_{22})^2 + (\sigma_{22} - \sigma_{33})^2 + (\sigma_{33} - \sigma_{11})^2 + 6(\sigma_{12}^2 + \sigma_{23}^2 + \sigma_{31}^2)}{2}} \quad (61)$$

where σ_{ij} are components of the stress tensor [81]. This is the equivalent stress used by the finite element software package AbaqusTM [58] for isotropic deformation during metal plasticity, and it is also the equivalent stress used in the 1.3 sigma, SDTD, and SDTDM1 material models. However, the von Mises stress is only appropriate if deformation is isotropic. For anisotropic deformation, a different equivalent stress is required. One anisotropic equivalent stress is the quadratic Hill stress, σ_H ,

$$\sigma_H = \sqrt{F(\sigma_{22} - \sigma_{33})^2 + G(\sigma_{33} - \sigma_{11})^2 + H(\sigma_{11} - \sigma_{22})^2 + 2L\sigma_{23}^2 + 2M\sigma_{31}^2 + 2N\sigma_{12}^2} \quad (62)$$

where F , G , H , L , M , and N are coefficients that describe plastic anisotropy [82]. This is the equivalent stress used by AbaqusTM for anisotropic deformation during metal plasticity. Note that other anisotropic equivalent stresses have been proposed in the literature [83-85]. However, these typically require additional parameters beyond those of

the Hill stress. Calculation of these parameters would require additional experimental data to determine these parameters independent of the data used for validation. Also, it is not clear that these more complex formulations offer any practical advantage over the Hill formulation for this application. Thus, the Hill stress is the anisotropic equivalent stress used in further analyses.

During deformation of a thin sheet, such as the 2-mm thick Mg AZ31 sheet of this investigation, σ_{33} , σ_{23} , and σ_{31} are negligibly small [86]; they are assumed to be zero here. Under this assumption, Equations 61 and 62 simplify to

$$\sigma_V = \sqrt{\frac{(\sigma_{11} - \sigma_{22})^2 + \sigma_{11}^2 + \sigma_{22}^2 + 6\sigma_{12}^2}{2}} \quad (63)$$

$$\sigma_H = \sqrt{F\sigma_{22}^2 + G\sigma_{11}^2 + H(\sigma_{11} - \sigma_{22})^2 + 2N\sigma_{12}^2} \quad (64)$$

The coefficients in Equation 64 can be calculated from R-values measured after tensile deformation. Recall that the AZ31 material of this investigation does not exhibit planar anisotropy [42], but only normal anisotropy. Thus, the anisotropy observed in the AZ31 tensile specimens must be solely normal to the sheet plane. Assuming only normal anisotropy, F , G , H , and N are

$$F = G = \frac{1}{1+r} \quad (65)$$

$$H = \frac{r}{1+r} \quad (66)$$

$$N = \frac{1+2r}{1+r} \quad (67)$$

where r is the R-value expected during tensile deformation [82, 87].

Equations 63 through 67 demonstrate how plastic anisotropy interacts with stress state during deformation. The normal plastic anisotropy observed during tensile deformation will affect deformation under other stress states and is a likely reason that the 1.3 stress factor was necessary in previous material models to accurately predict gas-pressure bulge forming. The relationship between the 1.3 factor and normal anisotropy during dislocation creep is revealed through calculations of the von Mises stress (Equation 63) and Hill stress (Equation 64) assuming normal anisotropy. First, consider the uniaxial stress state that occurs during a tensile test, where

$$\sigma_1 = \sigma \quad (68)$$

$$\sigma_2 = \sigma_3 = 0 \quad (69)$$

Assuming uniaxial stress,

$$\sigma_V = \sigma_H = \sigma \quad (70)$$

according to Equations 63 through 67. During uniaxial deformation, the von Mises and Hill stresses are identical. This is why the SDTD material model correctly predicts uniaxial stress-strain behavior at 450°C despite its incorrect assumption of isotropic deformation [23, 42]. Now consider the balanced-biaxial stress state that is characteristic of the dome pole during biaxial gas-pressure bulge forming, where

$$\sigma_1 = \sigma_2 = \sigma \quad (71)$$

$$\sigma_3 = 0 \quad (72)$$

Assuming balanced-biaxial stress,

$$\sigma_V = \sigma \quad (73)$$

$$\sigma_H = \sqrt{\frac{2}{1+r}} \sigma \quad (74)$$

according to Equations 63 through 67. The presence of normal anisotropy (with $r > 1$) results in a Hill stress that is some fraction of the corresponding von Mises stress, just as the 1.3 factor (see the 1.3 sigma and SDTDM1 material models) reduces the von Mises stress in the DC creep term. The 1.3 stress factor, therefore, acts as a crude method of converting the von Mises stress into the Hill stress for a balanced-biaxial stress state. Equation 74 suggests that the 1.3 factor corresponds to an R-value of 2.38, though this does not account for the effects of anisotropy on the resulting plastic strains.

The presence of normal anisotropy also affects the individual strain components produced during deformation. During deformation of a metallic material, these strains can be calculated using an associated flow rule,

$$d\varepsilon_{ij} = d\varepsilon \frac{\partial \sigma_{eff}}{\partial \sigma_{ij}} \quad (75)$$

where $d\varepsilon_{ij}$ are the increments in components of the strain tensor during a particular time step, $d\varepsilon$ is the uniaxial equivalent creep strain increment, calculated here by multiplying $\dot{\varepsilon}$ in Equation 48 by the time increment experienced during deformation, σ_{eff} is the appropriate effective stress (typically either the von Mises stress or Hill stress), and σ_{ij} are components of the stress tensor [88]. Equations 64 through 67 indicate that σ_{eff} is affected by the degree of normal anisotropy, which is quantified by r .

6.4. AN ANISOTROPIC MODIFICATION TO THE GDTD AND SDTD MODELS

Both the GDTD (Equation 48) and SDTD (Equation 20) material models can be modified to account for normal anisotropy by using the Hill stress in place of the von Mises stress, and using appropriate R-values to calculate the Hill stress for each of the two creep mechanisms controlling deformation. The new grain-size dependent material model, termed the GDTDAM (GDTD with anisotropy modification) model is

$$\dot{\varepsilon} = \frac{A_{GBS}}{d^p} \sigma_{GBS}^{n_{GBS}} + A_{DC} \sigma_{DC}^{n_{DC}} \quad (76)$$

where σ_{GBS} and σ_{DC} are Hill stresses calculated from the components of the stress tensor, see Equations 64 through 67. Specifically, σ_{GBS} is calculated with $r = r_{GBS} = 1.0$, and σ_{DC} is calculated with $r = r_{DC} = 1.86$. The remaining parameters in Equation 76 are the same as for the GDTD material model, see Table 5.7. Likewise, the new strain-dependent material model, termed the SDTDAM (SDTD with anisotropy modification) model is

$$\dot{\varepsilon} = A_{GBS}(\varepsilon) \sigma_{GBS}^{n_{GBS}(\varepsilon)} + A_{DC} \sigma_{DC}^{n_{DC}} \quad (77)$$

Both σ_{GBS} and σ_{DC} are calculated the same way as for the GDTDAM model. The remaining parameters in Equation 77 are the same as for the SDTD material model, see Table 2.2.

For both models, the resulting value of $\dot{\varepsilon}$ is multiplied by the incremental time during which deformation occurs to obtain $d\varepsilon$. Finally, the resulting components of the strain tensor are calculated using Equation 75, where σ_{eff} is associated with the effective R-value, r_{eff} , from Equation 55. The value of f_{DC} in Equation 55 can be calculated using the individual values for $\dot{\varepsilon}_{GBS}$ and $\dot{\varepsilon}_{DC}$ such that

$$f_{DC} = \frac{\dot{\epsilon}_{DC}}{\dot{\epsilon}_{GBS} + \dot{\epsilon}_{DC}} \quad (77)$$

Thus, the stress tensor is fully related to the resulting strain tensor in a material constitutive model describing the deformation behavior of AZ31 sheet at 450°C.

6.5. ANISOTROPY AND CRYSTALLOGRAPHIC TEXTURE

R-value measurements are used to quantify the anisotropic deformation of the AZ31 sheet. These measurements do not require any information as to the cause of the anisotropy. However, magnesium's HCP crystal structure suggests a likely reason for the normal anisotropy observed during this study. Recall that magnesium exhibits a range of critical resolved shear stresses (CRSS) for its various slip systems, as shown in Figure 2.3. The figure suggests that the CRSS for both pyramidal and prismatic slip are approximately 1 to 2 MPa at 450°C. For basal slip, the figure only provides data up to 280°C. However, the CRSS for basal slip is generally observed to be constant [89], and it is unlikely to increase with temperature. This suggests that the CRSS for basal slip is 0.5 MPa or less at 450°C. These values indicate that magnesium's HCP crystal structure remains anisotropic even at 450°C. A random orientation of the grains within the AZ31 sheet would cause the anisotropy of the individual grains to cancel out on the large length scale represented by the sheet, resulting in isotropic deformation. However, the AZ31 sheet may instead have a texture, such that the grains within the sheet have a preferred orientation. The textured sheet would exhibit similar anisotropy to that of the individual grains in their preferred orientation.

Many AZ31 sheet materials exhibit a strong basal texture [90-93], in which the basal planes of the grains (see Figure 2.2) tend to align with the plane of the sheet. Figure 6.4 contains pole figures obtained through electron backscatter diffraction (EBSD) of the AZ31 sheet used in this investigation. The sheet was annealed at 150°C for 20 minutes to recrystallize the microstructure prior to EBSD, which was performed by Aravindhya Antoniswamy. The pole figures show that there is a preferable orientation of the grains within the AZ31 sheet. The (0001) directions of the grain's crystal structures, shown in Figure 2.2, are oriented closely to the sheet normal. This confirms that the sheet contains a strong basal texture similar to that observed in other studies.

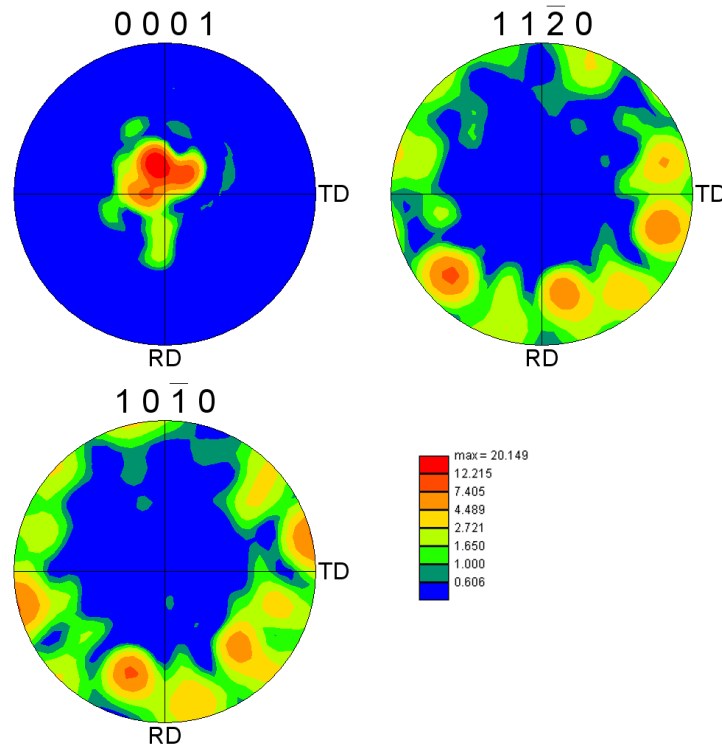


Figure 6.4: Pole figures obtained from EBSD of the AZ31 sheet are shown. The sheet was recrystallized at 150°C for 20 minutes prior to EBSD. Texture intensities are displayed using a times-random scale. The pole figures were obtained by Aravindhya Antoniswamy.

It is likely that the basal texture of the AZ31 sheet is responsible for anisotropic deformation during DC creep. DC creep occurs when crystallographic planes slip relative to one another through the movement of dislocations [56-57]. Figure 2.3 suggests that basal slip occurs more easily than non-basal slip, even at 450°C. For a material with a strong basal texture, this suggests that slip will occur more easily in the sheet plane than normal to the sheet. This results in the observed normal anisotropic deformation during DC creep. Note that GBS creep occurs when grain boundaries slide relative to one another [56-57]. This suggests that GBS creep does not depend on grain orientation, as deformation is confined primarily to grain boundaries. Thus, GBS creep is expected to be isotropic, as was observed in this study.

Chapter 7: Finite-Element-Method Simulations

7.1. USER-DEFINED FUNCTIONS

The GDTDAM and SDTDAM material constitutive models must be implemented into a finite-element-method (FEM) code if they are to be used in simulations. AbaqusTM [58], a suite of commercial FEM software, was used for simulations because it was also previously used to evaluate the SDTD and SDTDM1 material models [23, 42]. All of the two-term material constitutive models discussed in this work are too complicated to be described by the simple default creep models available in Abaqus. However, Abaqus allows the user to define more complicated material constitutive behavior in additional subroutines, which are written in the programming language Fortran [94]. The two-term material models are all implemented in a user-defined subroutine named CREEP.

The CREEP subroutine allows the user to define the uniaxial equivalent creep strain, $d\varepsilon$ (the product of $\dot{\varepsilon}$ and the current time increment dt), as a function of variables such as the equivalent strain, ε (calculated using Equation 33), forming time, t , and an equivalent stress. The equivalent stress is automatically calculated using either the von Mises stress or Hill stress formulations. This implementation is sufficient for the SDTD and SDTDM1 models, which assume that the equivalent stresses in the GBS and DC terms are identical [23, 42]. However, the GDTDAM and SDTDAM models are two-term (two-mechanism) creep models wherein each term (mechanism) produces a *different* plastic anisotropy. This subtlety requires calculation of a different equivalent stress for

each creep term (see Equation 76 and 77), which cannot be done using the CREEP subroutine alone. A second user subroutine, USDFLD, is needed to meet this requirement. The USDFLD subroutine allows the user to obtain values for individual variables at integration points, such as individual tensor components, and update user-defined variables. The stress tensor is obtained at each integration point using the USDFLD subroutine and used to calculate the mechanism-dependent equivalent stresses σ_{GBS} and σ_{DC} , which are stored in solution-dependent state variables. These state variables can then be accessed by CREEP and used to calculate $\dot{\epsilon}$ for the GDTDAM (Equation 76) or SDTDAM (Equation 77) material models. The CREEP subroutine also automatically calculates the individual strain tensor components using the associated flow rule, see Equation 75. This equation is only valid if σ_{eff} is the Hill stress calculated from the effective R-value, r_{eff} , expected from both GBS and DC creep. Thus, f_{DC} is calculated from Equation 77, and r_{eff} is calculated using Equation 55 and stored in a solution-dependent state variable.

The Fortran codes for the GDTDAM and SDTDAM material constitutive models are provided in Appendix B. Each model's code is typically stored in a computer file named creep.f, which can be included in an Abaqus FEM analysis.

7.2. SIMULATION DESCRIPTIONS

7.2.1. Tensile Simulations

In FEM simulations of tensile tests, the gage section of the tensile coupon was modeled with a mesh comprised of four-node quadrilateral membrane (M3D4) elements

measuring 1 mm on a side with an initial thickness of 2 mm. This mesh, shown in Figure 7.1, was used previously in tensile simulations of the SDTD and SDTDM1 material constitutive models [23, 42]. Membrane elements suffice because flow localization (necking) is neglected for the simulations. During simulations, one of the mesh boundaries was fixed in the y-direction, as shown in Figure 7.1. The other boundary was displaced at an increasing speed to approximate a constant true-strain rate along the tensile direction of the mesh. Stress and strain components were recorded during simulations for the element indicated with an X in Figure 7.1. Tensile simulations were conducted for constant true-strain rates of 10^{-4} , 3×10^{-4} , 10^{-2} , and $3 \times 10^{-2} \text{ s}^{-1}$ using both the GDTDAM and SDTDAM material models. The simulation results were compared to both experimental data and results obtained using the SDTD and SDTDM1 material models. Appendix C contains an example input file for use in AbaqusTM tensile simulations.

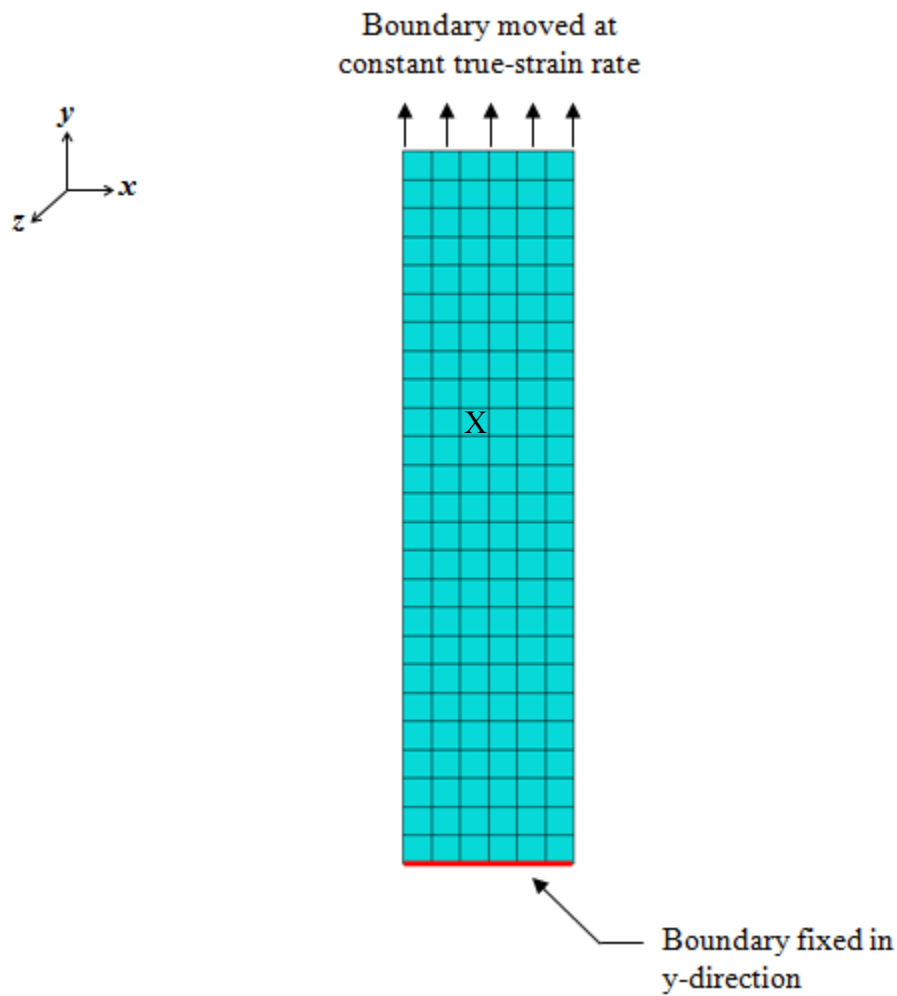


Figure 7.1: The mesh used in Abaqus tensile simulations is shown. The mesh elements are 1 mm on a side with an initial thickness of 2 mm. The X indicates the element for which stresses and strains are output during simulations. The figure is from Ref. 23.

7.2.2. Biaxial Bulge Forming Simulations

In FEM simulations of biaxial gas-pressure bulge tests, both the specimen blank and die were modeled as axisymmetric two-node linear shell (SAX1) elements with an average size of 1.5 mm. Note that the shell elements do not account for thinning

localization at large strains. The axisymmetric blank and die meshes are shown in Figure 7.2 for the University of Texas bulge forming geometry, which has a die inner diameter of 55.4 mm and a die entry radius of 1.5 mm. In the figure, both meshes were revolved 180° around the axis of symmetry to provide better visualization of the blank and die. A second similar pair of meshes was created to model the General Motors bulge forming geometry, which has a die inner diameter of 100 mm and die entry radius of 5 mm. During simulations, the edge node of the blank was fixed, which mimics the effect of the seal bead as it clamps down on the AZ31 sheet blank. Pressure was then applied to the top of the specimen blank, causing it to form downward into the die. The displacement and thickness of the blank element closest to the axis of symmetry were recorded during the simulation. For the University of Texas geometry, simulations were conducted for pressures of 550, 830, and 1100 kPa using both the GDTDAM and SDTDAM material models. At 830 kPa, further simulations were conducted to account for the effects of preheat time on the AZ31 deformation behavior. This was accomplished by replacing time, t , in the GDTDAM model with $t + t_{pre}$, where t_{pre} is a preheat time ranging from 30 to 960 s. For the General Motors geometry, simulations were conducted for pressures of 280 and 520 kPa using both the GDTDAM and SDTDAM material models. For both pressures, further simulations were conducted to account for the effects of initial grain size on the AZ31 deformation behavior. This was accomplished by replacing the initial grain size in the GDTDAM model, $d_o = 8.7 \mu\text{m}$, with the initial grain size of one of the other two tested materials, 6.68 or 19.7 μm . Simulation results were compared to both experimental data and results obtained using the SDTD and SDTDM1 material models.

Appendix C contains example input files for use in Abaqus simulations of the University of Texas and General Motors bulge forming geometries.

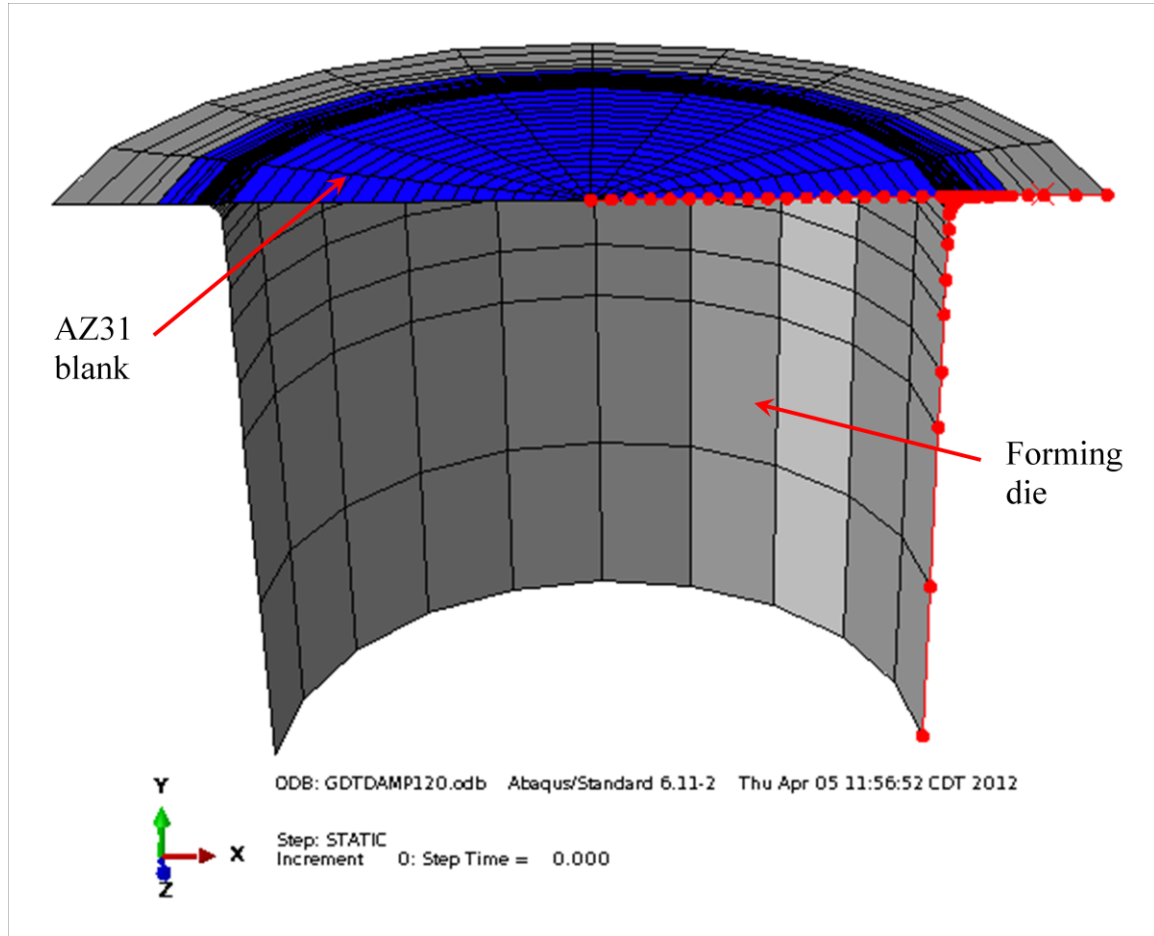


Figure 7.2: The mesh used in Abaqus gas-pressure bulge forming simulations of the University of Texas geometry is shown. The nodes of the axisymmetric sheet blank and forming die meshes are shown as red markers, while the axisymmetric elements are shown as red lines. The axisymmetric mesh is revolved 180° around the axis of symmetry to provide a better visualization of the blank and die. The AZ31 blank is shown in blue, while the forming die is shown in gray.

Chapter 8: Results and Discussion

8.1. MEASURES OF ERROR

FEM simulation results are compared to experimental data to determine the accuracy of material constitutive models under various forming conditions. When comparing simulations to experiments, it is useful to quantify the resulting errors to facilitate subsequent comparisons of the various material models. Two common measures of error are the root-mean-square (RMS) error and the mean-percent-difference (MPD) error. The RMS error is given by

$$x_{RMS} = \sqrt{\frac{1}{n} \sum_{i=1}^n (x_{exp} - x_{sim})^2} \quad (78)$$

where n is the number of comparisons between two data sets, x_{exp} is an experimental measurement from a data set, and x_{sim} is the corresponding simulation prediction. The RMS error provides a quantitative measure of the magnitude difference between experimental data and the corresponding simulation predictions. However, it is always positive, so it does not indicate whether simulation predictions are smaller or larger than experimental measurements. The MPD error is given by

$$x_{MPD} = \frac{1}{n} \sum_{i=1}^n \frac{x_{sim} - x_{exp}}{x_{exp}} \times 100\% \quad (79)$$

where n is the number of comparisons between two data sets, x_{exp} is an experimental measurement from a data set, and x_{sim} is the corresponding simulation prediction. The sign of the MPD error indicates whether simulation predictions are generally smaller or

larger than the corresponding experimental data. However, the MPD error may average individual errors within a data set to approximately zero if some simulation results are smaller than experimental measurements and other simulation results are larger than experimental measurements. Thus, the RMS and MPD errors are both required to meaningfully quantify differences between simulations and experiments.

The primary method of evaluating the ability of a material constitutive model to predict tensile deformation is to compare the stress-strain curves predicted by simulations to the experimental stress-strain data. Results are compared here for true strains ranging from 0 to 0.6. These strains are generally low enough to avoid flow localization (necking), which is not predicted by the material models. Therefore, the RMS and MPD errors were calculated from 100 equally-spaced true strains ranging from 0 to 0.6, such that $n = 100$ in Equations 78 and 79. At each of these strains, x_{exp} is the true stress from experimental data, and x_{sim} is the true stress predicted by simulation. These stresses were obtained through linear interpolation of the experimental data and simulation results so that comparisons could be performed at the equally-spaced true strains.

Two measurements are used to evaluate a material constitutive model's ability to predict biaxial gas pressure bulge forming: dome heights and pole thicknesses. Forming is fastest immediately upon the application of gas pressure and at the end of forming prior to rupture. The increase in forming rate prior to rupture is thought to be caused by the onset of localized thinning and/or damage such as cavitation. These effects, which are not accounted for by the various material models, cause forming to speed up once the dome height becomes approximately 40% of the die diameter. This corresponds to a dome

height of 22 mm for the University of Texas geometry and a dome height of 40 mm for the General Motors geometry. Thus, bulge forming results are compared for forming times ranging from 0 to the time at which experimental dome heights reach these limits. For comparisons involving the University of Texas geometry, the RMS and MPD errors on dome height were calculated from 100 equally-spaced forming times within this range, such that $n = 100$ in Equations 78 and 79. For comparisons involving the General Motors geometry, the RMS and MPD errors were calculated for each experimental measurement within this range. At each forming time, x_{exp} is the dome height or pole thickness calculated from experiment, while x_{sim} is the corresponding dome height or pole thickness predicted by simulation. These values were obtained through linear interpolation so that experimental data and simulation results are compared at the same forming times.

8.2. VARIABILITY AND REPEATABILITY

The measures of error were also used to evaluate the repeatability of experiments conducted during the study. Multiple tensile tests were conducted at 450°C and 10^{-3} s^{-1} to evaluate the variability and repeatability inherent in tensile testing of the AZ31 sheet. Tensile tests should obviously be repeatable. Otherwise, there is little reason to try to predict tensile forming. The additional tensile test results were compared to the data used to create the material constitutive models [42] in this study. A similar comparison was performed at 450°C and 10^{-1} s^{-1} , though with fewer repetitions.

Figure 8.1(a) presents true stress-true strain measurements from five tensile tests at 450°C and 10^{-3} s^{-1} . The data contain some noise from the load cell, which is due to the low loads required for deformation at 10^{-3} s^{-1} . The Voce law, see Equation 49, was fit to each stress-strain curve to smooth out the noise. The Voce law fits for each tensile test are presented in Figure 8.1(b). These curves indicate that there is little variation between tests at 10^{-3} s^{-1} . The MPD between each pair of curves in Figure 8.1(b) was calculated using Equation 79. The maximum RMS error between any two tensile tests is 0.51 MPa, while the maximum absolute value of the MPD between any two tensile tests is 3.8%.

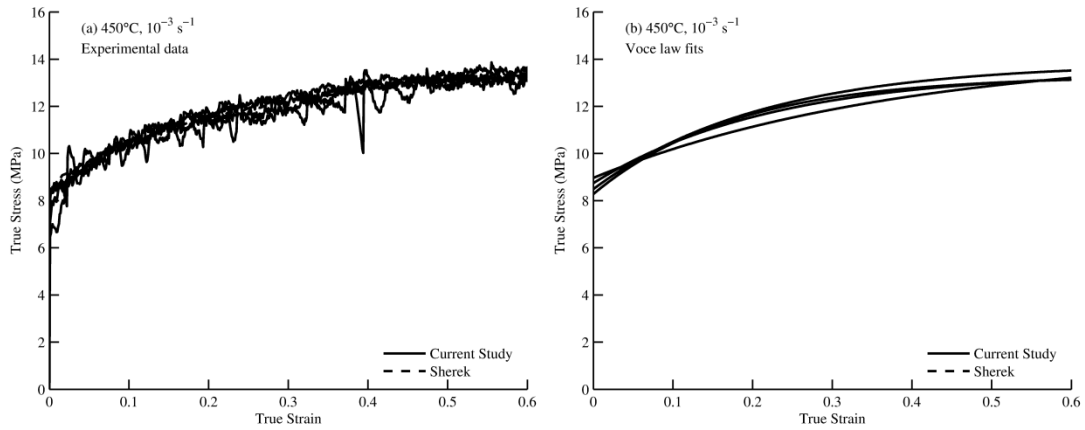


Figure 8.1: True stress (a) data and (b) the corresponding Voce law fits are plotted against true strain for tensile tests at 450°C and 10^{-3} s^{-1} . Solid curves represent data from this study, while dashed curves represent data from a previous study [42].

Figure 8.2 presents true stress-true strain measurements from three tensile tests at 450°C and 10^{-1} s^{-1} . The loads required for deformation at 10^{-1} s^{-1} are large enough that noise from the load cell is minimal. The data indicate that there is little variation between tests at 10^{-1} s^{-1} for true strains less than 0.4. Beyond this strain, flow localization results in

a drop in true stress, though the degree of this drop varies between tests. Flow localization is neglected in this study. Thus, the MPD between each pair of curves in Figure 8.2 was calculated using data at true strains less than 0.4. The maximum RMS error between any two tensile tests is 0.91 MPa, while the maximum absolute value of the MPD between any two tensile tests is 3.4%.

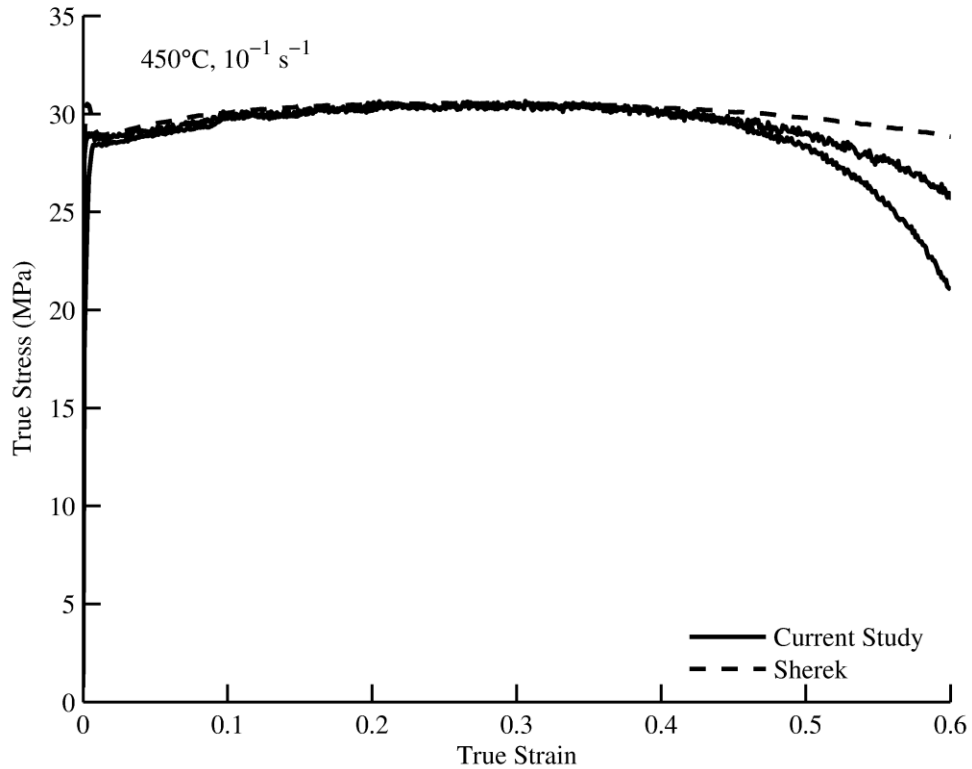


Figure 8.2: True stress is plotted against true strain for tensile tests at 450°C and 10^{-1} s^{-1} . Solid curves represent data from this study, while dashed curves represent data from a previous study [42].

The repeatability of the biaxial gas-pressure bulge tests was also investigated. Predictions of bulge forming are only meaningful if gas-pressure bulge tests are repeatable. Multiple bulge tests were conducted using the University of Texas geometry

at 450°C and 830 kPa, and dome height measurements from the tests were compared to data from a test by Sherek [23]. Two additional tests were conducted at 550 and 1100 kPa, and the dome height measurements from each test were also compared to Sherek's data.

Figure 8.3 presents measurements of dome height versus forming time for the bulge tests conducted at 450°C and 830 kPa. The data indicate that there is little variation between bulge tests. The MPD between each pair of curves in Figure 8.3 was calculated using Equation 79. The maximum RMS error between any two bulge tests is 0.62 mm, while the maximum absolute value of the MPD between any two bulge tests is 4.7%.

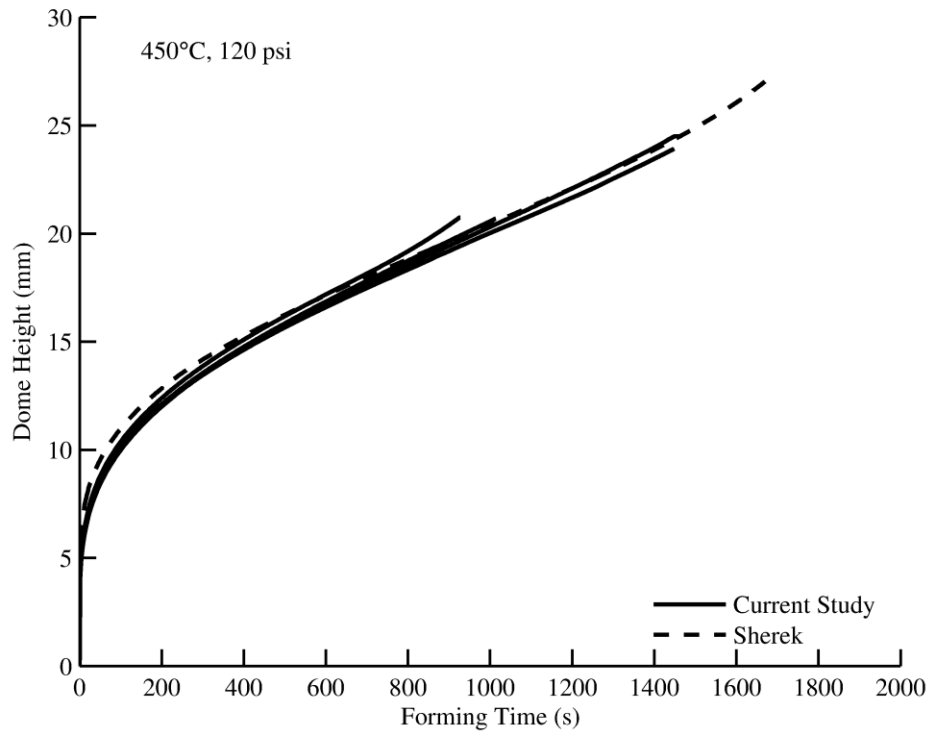


Figure 8.3: Dome height is plotted against forming time for bulge tests run using the University of Texas apparatus at 450°C and 830 kPa. Solid curves represent data from this study, while dashed curves represent data from a previous study [23].

Figure 8.4 presents measurements of dome height versus forming time for the bulge tests conducted at (a) 550 and (b) 1100 kPa. These data also indicate that there is little variation between bulge tests. The MPD between each pair of curves in Figure 8.4 was calculated using Equation 79. The RMS error between the two bulge tests is 0.75 mm at 550 kPa and 0.27 mm at 1100 kPa. The absolute value of the MPD between the two bulge tests is 3.5% at 550 kPa and 0.9% at 1100 kPa.

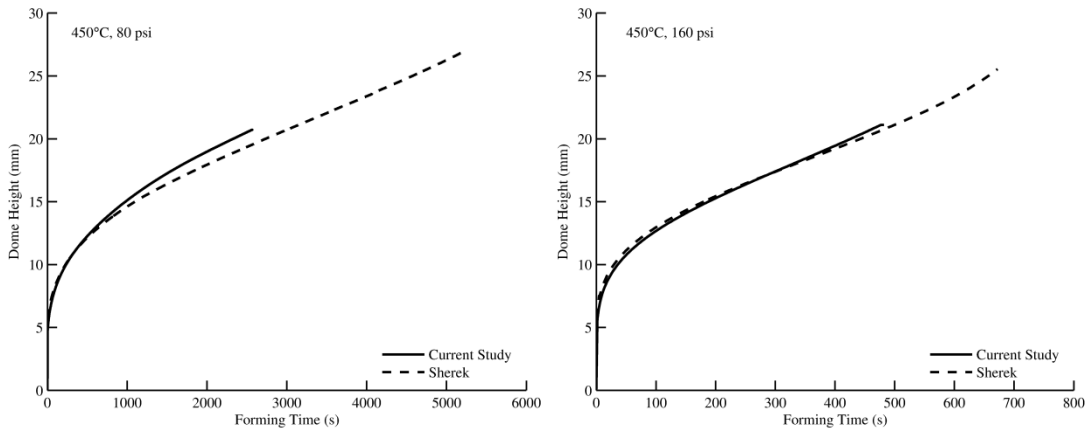


Figure 8.4: Dome height is plotted against forming time for bulge tests run using the University of Texas apparatus at 450°C and (a) 550 kPa or (b) 1100 kPa. Solid curves represent data from this study, while dashed curves represent data from a previous study [23].

These results suggest that the inherent variability of both tensile stress and biaxial dome height measurements is less than 5%. The MPD between simulation results and experimental data should ideally fall within this range. However, the material constitutive models used in simulations only approximate the complex physics of plastic deformation, and even a reasonably accurate material model may occasionally fall outside of this range. For this study, a material model is considered to successfully predict the results of

a particular forming experiment if the absolute value of the MPD is less than 10% (twice the maximum experimental MPD), as a prediction of this accuracy would certainly be useful when designing a forming operation and determining processing parameters.

The results also suggest that the maximum RMS error between tensile tests is approximately 1 MPa. Again, an accurate material model should have an RMS error of less than twice this value, which is 2 MPa. The maximum RMS error between bulge tests is approximately 0.8 mm for the University of Texas apparatus, which suggests that a material model should have an RMS error less than 1.6 mm when predicting forming with the University of Texas geometry. The General Motors bulge test die is approximately 1.8 times as large as the University of Texas bulge test die, which suggests that a material model should have an RMS error less than 2.9 mm when predicting bulge forming with the General Motors geometry.

8.2. TENSILE RESULTS

8.2.1. True Stress-True Strain Curves

Figure 8.5 compares experimental true stress-true strain data from tensile tests at 450°C to simulation results obtained using the SDTD, SDTDM1, SDTDAM, and GDTDAM material models. Comparisons are presented for constant true-strain rates of (a) 10^{-4} , (b) 3×10^{-4} , (c) 10^{-2} , and (d) $3 \times 10^{-2} \text{ s}^{-1}$. For all four strain rates, the experimental data are from Ref. 42. At each strain rate, the RMS and MPD true stress errors were calculated for the SDTD, SDTDM1, SDTDAM, and GDTDAM material models. These errors are presented in Tables 8.1 and 8.2.

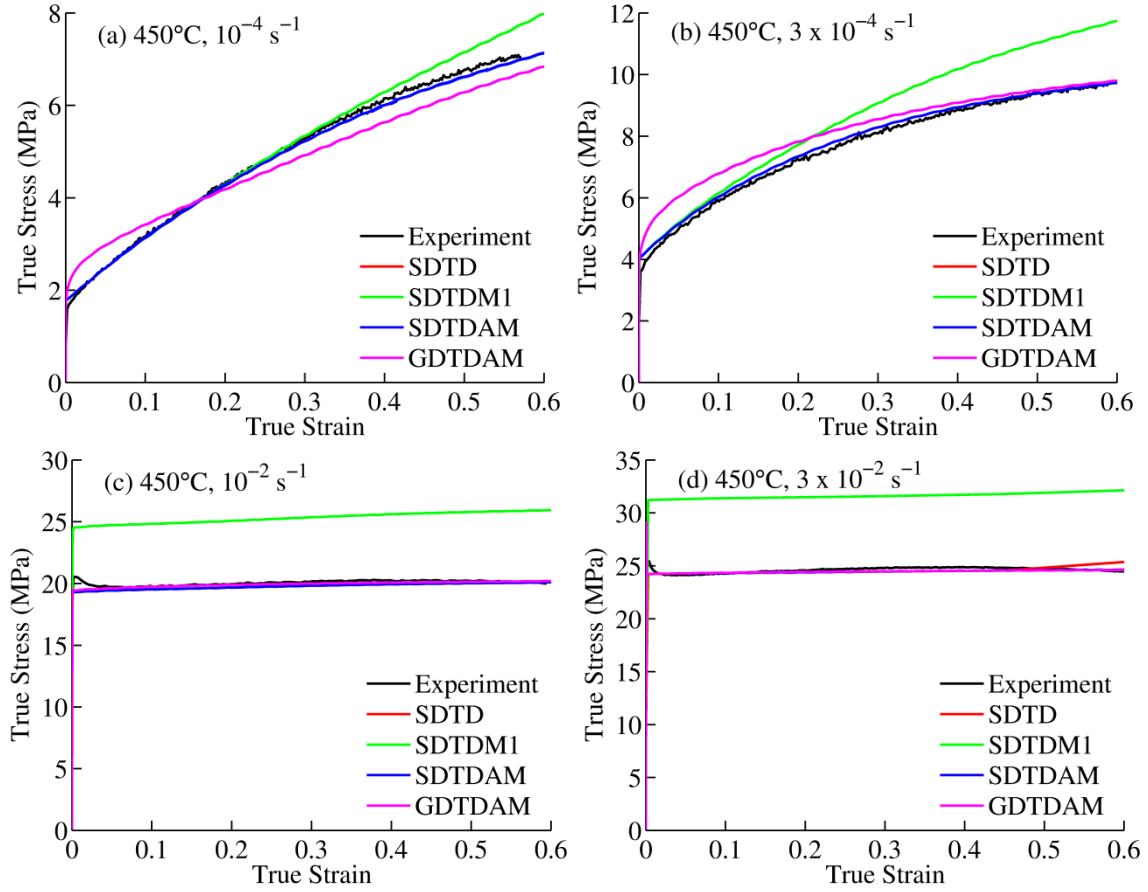


Figure 8.5: True stress is plotted against true strain at 450°C for constant true-strain rates of (a) 10^{-4} , (b) 3×10^{-4} , (c) 10^{-2} , and (d) $3 \times 10^{-2} \text{ s}^{-1}$. Experimental data are from Ref. 42. For all strain rates, the SDTD simulation results are identical to the SDTDAM results.

Table 8.1: The RMS errors on true stresses for the SDTD, SDTDM1, SDTDAM, and GDTDAM material constitutive models are presented. All values are in MPa.

True-Strain Rate (s^{-1})	SDTD	SDTDM1	SDTDAM	GDTDAM
10^{-4}	0.09	0.23	0.09	0.39
3×10^{-4}	0.14	1.11	0.14	0.59
10^{-2}	0.32	5.27	0.32	0.19
3×10^{-2}	0.32	7.02	0.23	0.23

Table 8.2: The MPD errors on true stresses for the SDTD, SDTDM1, SDTDAM, and GDTDAM material constitutive models are presented. All values are percentages.

True-Strain Rate (s^{-1})	SDTD	SDTDM1	SDTDAM	GDTDAM
10^{-4}	-1.2	2.0	-1.1	-0.9
3×10^{-4}	1.8	11.3	1.8	7.8
10^{-2}	-1.4	26.2	-1.4	-0.5
3×10^{-2}	-0.2	28.5	-0.6	-0.6

The comparisons with tensile data reveal that three of the four material constitutive models provide accurate predictions of tensile stress-strain data. The SDTD and SDTDAM stress-strain curves are almost identical. This is expected because the two models only differ in their equivalent stresses. Both the von Mises stress and Hill stress are equal under a uniaxial stress state, see Equation 70. Thus, those two models provide equivalent results. The SDTD and SDTDAM models both agree well with the experimental data for all four strain rates, as both models have RMS errors less than 0.4 MPa and MPD errors with absolute values less than 2%. The GDTDAM model is somewhat less accurate than the SDTD and SDTDAM models at the two slower strain rates, with RMS errors as large as 0.6 MPa and MPD errors as large as 8%. Still, the GDTDAM model, which assumes that GBS creep hardening depends on grain size, is accurate enough to provide further evidence that grain growth is responsible for the observed strain hardening at slow strain rates. The SDTDM1 model provides accurate predictions at the slowest strain rate of $10^{-4} s^{-1}$. As strain rate increases, however, the stresses predicted by the SDTDM1 model become larger than those observed experimentally. The RMS error of the SDTDM1 model increases to approximately 7 MPa, while the MPD error is almost 30% at the fastest strain rate of $3 \times 10^{-2} s^{-1}$. This

indicates that the 1.3 factor in the SDTDM1 model, which was added to provide accurate predictions of biaxial gas-pressure bulge forming, eliminates the ability of the model to reproduce tensile data across the range of relevant strain rates.

8.2.2. R-value Data

In addition to stress-strain data, an accurate material model should also predict the resulting strains in the non-tensile directions. Therefore, R-values from simulations run using the SDTD, SDTDM1, SDTDAM, and GDTDAM material models are compared to the experimental measurements from Figure 6.3. Figure 8.6 presents the R-values as a function of true strain for true-strain rates of 10^{-4} , 3×10^{-4} , 10^{-2} , and $3 \times 10^{-2} \text{ s}^{-1}$. The SDTD and SDTDM1 models both provide identical R-value predictions, and they are plotted as the same dashed line. Similarly, the SDTDAM and GDTDAM models provide identical R-value predictions, and they are plotted as the same solid curves.

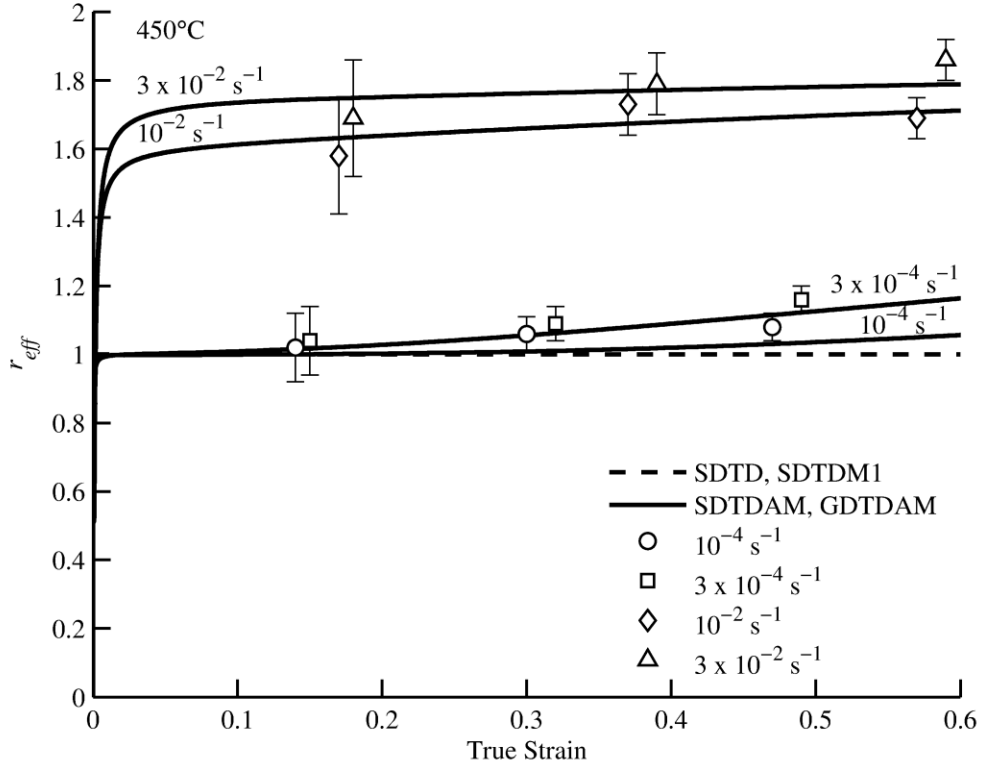


Figure 8.6: Effective R-values, r_{eff} , are plotted against true strain for constant true-strain rates of 10^{-4} , 3×10^{-4} , 10^{-2} , and $3 \times 10^{-2} \text{ s}^{-1}$. Experimental data are plotted as markers. SDTD and SDTDM1 simulation results are plotted as a dashed line for all strain rates. SDTDAM and GDTMAM simulation results are plotted as solid curves for each strain rate.

Figure 8.6 illustrates a key weakness of the SDTD and SDTDM1 material constitutive models. Both the SDTD and SDTDM1 models predict effective R-values of 1.0 for all true-strain rates, as these models do not explicitly address plastic anisotropy. The SDTD and SDTDM1 models use the von Mises stress in calculations, which assumes isotropic deformation. However, Mg AZ31 sheet exhibits anisotropic deformation at the fast strain rates for which DC creep produces deformation, which is illustrated by the experimental data. Although the SDTD material model accurately reproduces

experimental stress-strain curves, it cannot accurately predict normal strains along the short-transverse and long-transverse directions in a tensile coupon. Thus, the SDTD model does not predict r_{eff} . This indicates that the SDTD material model does not predict tensile deformation as accurately as previously thought [23, 42]. Conversely, the SDTDAM and GDTDAM material models accurately reproduce the R-values measured from experiment. Thus, they can accurately predict the full strain tensor resulting from normal anisotropy. This ability represents a significant improvement over previous material models, such as the SDTD and SDTDM1 models. Furthermore, this allows the SDTDAM and GDTDAM models to be applied to any general stress state occurring during deformation at 450°C, a capability beyond previous material models.

8.3. BIAXIAL BULGE FORMING RESULTS

8.3.1. University of Texas Geometry

Figure 8.7 compares experimental dome heights from biaxial gas-pressure bulge tests using the University of Texas geometry to simulation results obtained using the SDTD, SDTDM1, SDTDAM, and GDTDAM material models. Comparisons are presented for gas pressures of (a) 550, (b) 830, and (c) 1100 kPa. At each pressure, the RMS and MPD dome height errors were calculated for the SDTD, SDTDM1, SDTDAM, and GDTDAM material models. These errors are presented in Tables 8.3 and 8.4.

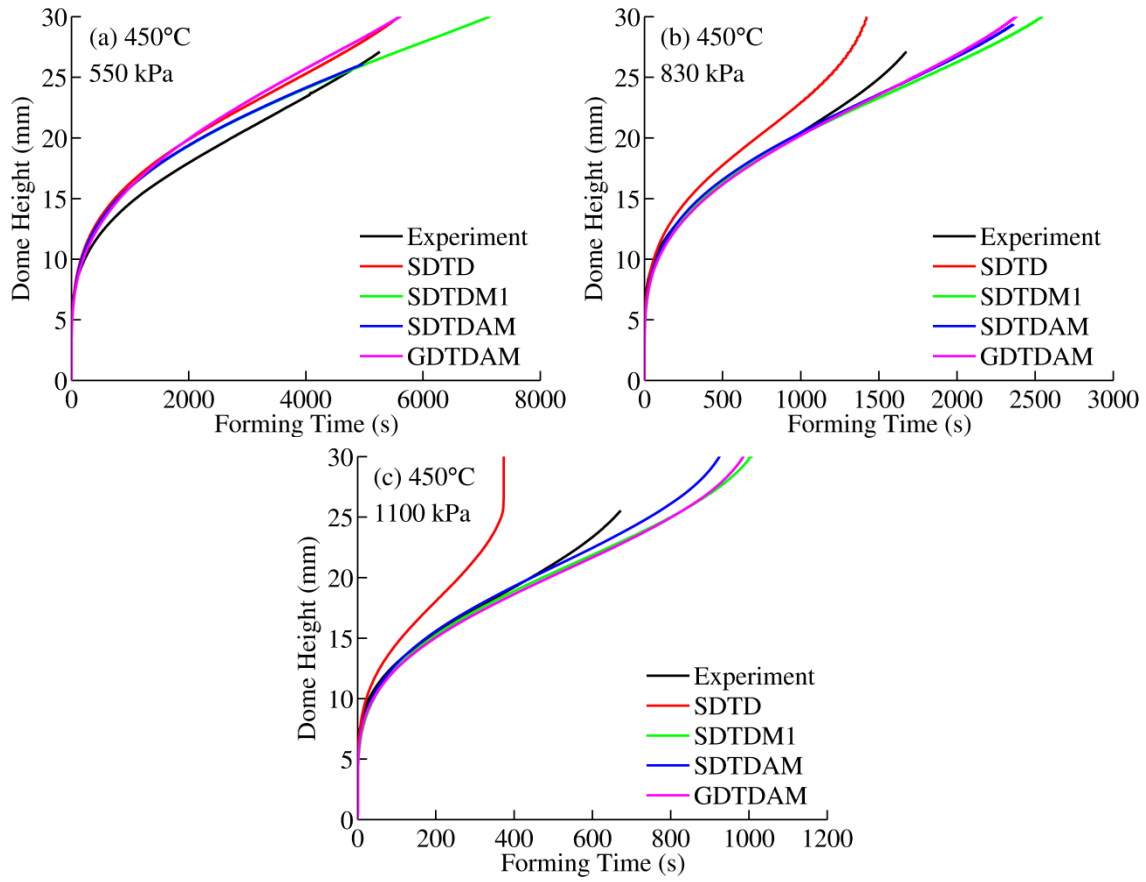


Figure 8.7: Dome height is plotted against forming time at 450°C for gas pressures of (a) 550, (b) 830, and (c) 1100 kPa. Experiments and simulations use the University of Texas geometry.

Table 8.3: The RMS errors on dome heights for the SDTD, SDTDM1, SDTDAM, and GDTDAM material constitutive models are presented. Experiments and simulations were conducted using the University of Texas geometry. All values are in mm.

Gas Pressure (kPa)	SDTD	SDTDM1	SDTDAM	GDTDAM
550	1.7	1.2	1.3	1.6
830	1.5	0.3	0.3	0.4
1100	2.5	0.5	0.3	0.6

Table 8.4: The MPD errors on dome heights for the SDTD, SDTDM1, SDTDAM, and GDTDAM material constitutive models are presented. Experiments and simulations use the University of Texas geometry. All values are percentages.

Gas Pressure (kPa)	SDTD	SDTDM1	SDTDAM	GDTDAM
550	10.4	7.3	7.7	8.6
830	8.0	-1.1	0.1	-2.0
1100	14.7	-2.8	-0.5	-3.8

The gas-pressure bulge test comparisons signify the need to account for the normal anisotropy resulting from DC creep during biaxial forming. At 550 kPa, all material models provide similar predictions of dome height versus forming time. The RMS errors for the SDTDM1, SDTDAM, and GDTDAM models are less than 1.6 mm, while the RMS error for the SDTD model is only slightly larger. Similarly, the MPD errors for the SDTDM1, SDTDAM, and GDTDAM models are all 10% or less, while the MPD error for the SDTD model is only slightly larger. The results from all four material models agree well with those observed experimentally because GBS creep, which is isotropic, dominates deformation. At 830 and 1100 kPa, DC creep begins to play an increased role in deformation. The SDTD model does not account for the anisotropy resulting from DC creep. Thus, the SDTD model predicts faster forming than observed experimentally, especially at 1100 kPa. The MPD error at this pressure is almost 15%. The 1.3 factor in the SDTDM1 model is a crude method of accounting for the anisotropy resulting from DC creep during balanced biaxial deformation, while the SDTDAM and GDTDAM models use the Hill stress and experimentally-determined R-values to account for anisotropy. Thus, all three models agree very well with the experimental

results at 830 and 1100 kPa. For these pressures, the three models have RMS errors less than 0.7 mm and MPD errors with absolute values less than 4%.

8.3.2. General Motors Geometry

Figure 8.8 compares experimental (a) dome heights and (b) pole thicknesses from biaxial gas-pressure bulge tests at 280 kPa using the General Motors geometry to simulation results obtained using the SDTD, SDTDM1, SDTDAM, and GDTDAM material models. Similarly, Figure 8.9 compares experimental (a) dome heights and (b) pole thicknesses from biaxial gas-pressure bulge tests at 520 kPa using the General Motors geometry to simulation results obtained using the SDTD, SDTDM1, SDTDAM, and GDTDAM material models. Tables 8.5 and 8.6 contain the RMS and MPD dome height errors for the two pressures, while Tables 8.7 and 8.8 contain the RMS and MPD pole thickness errors.

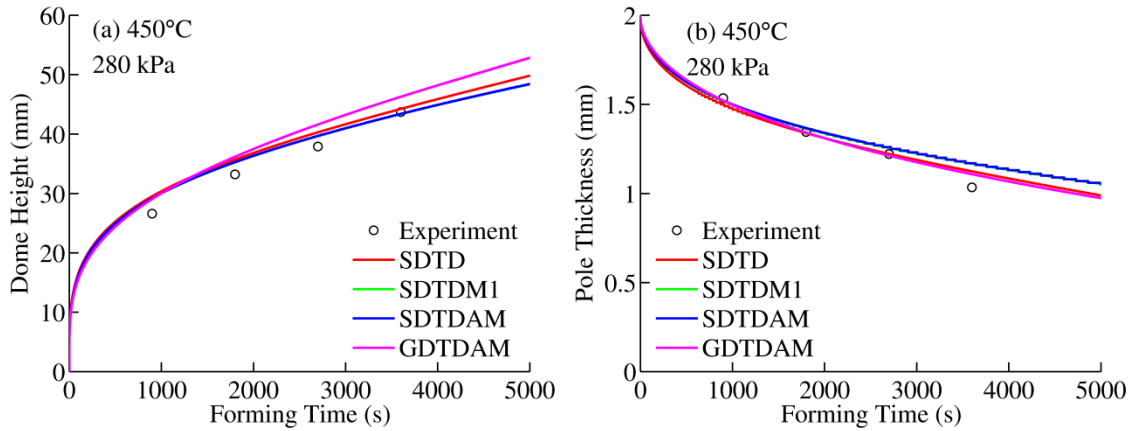


Figure 8.8: (a) Dome height and (b) pole thickness are plotted versus forming time at 450°C and 280 kPa. Experiments and simulations use the General Motors geometry.

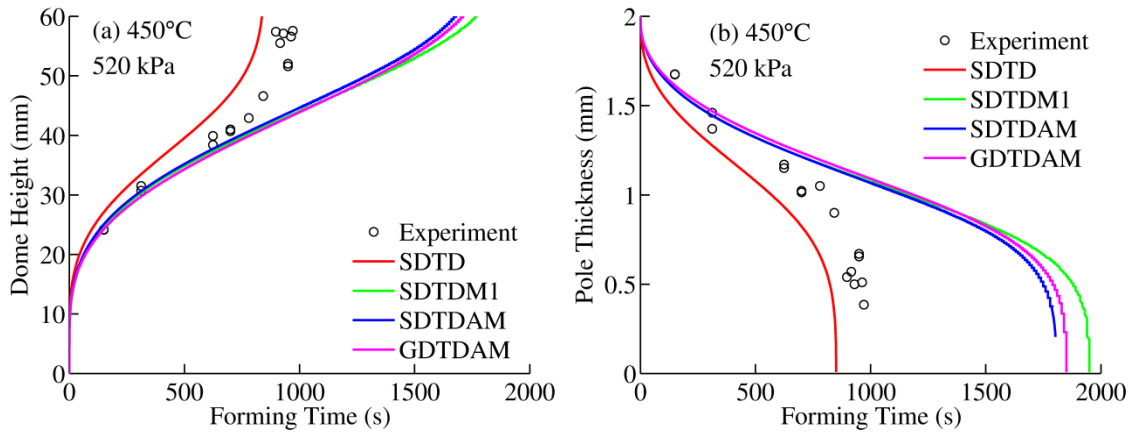


Figure 8.9: (a) Dome height and (b) pole thickness are plotted versus forming time at 450°C and 520 kPa. Experiments and simulations use the General Motors geometry.

Table 8.5: The RMS errors on dome heights for the SDTD, SDTDM1, SDTDAM, and GDTDAM material constitutive models are presented. Experiments and simulations use the General Motors geometry. All values are in mm.

Gas Pressure (kPa)	SDTD	SDTDM1	SDTDAM	GDTDAM
280	2.6	2.2	2.2	3.1
520	3.5	1.3	1.1	1.6

Table 8.6: The MPD errors on dome heights for the SDTD, SDTDM1, SDTDAM, and GDTDAM material constitutive models are presented. Experiments and simulations use the General Motors geometry. All values are percentages.

Gas Pressure (kPa)	SDTD	SDTDM1	SDTDAM	GDTDAM
280	8.3	6.8	6.9	9.3
520	10.6	-1.6	-0.5	-3.3

Table 8.7: The RMS errors on pole thicknesses for the SDTD, SDTDM1, SDTDAM, and GDTDAM material constitutive models are presented. Experiments and simulations use the General Motors geometry. All values are in mm.

Gas Pressure (kPa)	SDTD	SDTDM1	SDTDAM	GDTDAM
280	0.02	0.02	0.03	0.01
520	0.19	0.08	0.08	0.09

Table 8.8: The MPD errors on pole thicknesses for the SDTD, SDTDM1, SDTDAM, and GDTDAM material constitutive models are presented. Experiments and simulations use the General Motors geometry. All values are percentages.

Gas Pressure (kPa)	SDTD	SDTDM1	SDTDAM	GDTDAM
280	-0.9	0.9	1.3	-0.6
520	-13.7	1.7	1.8	3.4

At 280 kPa, all four material models provide similar predictions of both dome height and pole thickness. For dome height, the RMS errors for the SDTD, SDTDM1, and SDTDAM models are less than 2.9 mm, while the RMS error for the GDTDAM model is only slightly larger. The MPD errors are all between 6 and 10%. For pole thickness, the RMS errors are all less than 0.01 mm, while the MPD errors are all less than 1.5%. However, an increase in pressure increases the fraction of strain due to DC creep, which was also observed with the University of Texas geometry. Because DC creep is anisotropic, the SDTD model is less accurate than the other three models at 520 kPa. At this pressure, the SDTD MPD errors for dome height and pole thickness are 10.6 and -13.7% respectively. The other three material models, which account for the anisotropy of the AZ31 sheet, have MPD errors with absolute values less than 4% at 520 kPa. Note that the SDTDM1, SDTDAM, and GDTDAM material models diverge from the experimental data at dome heights greater than 40 mm, see Figure 8.9. This divergence represents the effects of cavitation and/or localized thinning, which cause the forming rate to increase. These effects are not accounted for by the material models, because a formed part that exhibits cavitation damage or localized thinning is likely unfit for service anyway.

8.3.3. Effects of Preheat Time

The above results indicate that the SDTDAM material model is slightly more accurate than the GDTDAM model, especially for tensile predictions at slow strain rates. However, the GDTDAM model does have a significant advantage over strain-dependent material models such as the SDTDAM model. The GDTDAM material model couples GBS creep hardening to the grain size of the material. Thus, the grain size model within the GDTDAM material model can be modified to account for factors that would affect grain size, which in turn affects the deformation behavior of the AZ31 sheet. The strain-dependent models account for hardening in the GBS creep regime with strain-dependent functions that do not have a physical basis. These models cannot be easily modified to account for microstructural changes that would affect GBS creep.

One processing parameter that can affect both grain size and forming behavior is preheat time. Recall that Sherek observed a decrease in the deformation rate during gas-pressure bulge forming as preheat time increases prior to forming [23]. The same effect was observed during this study. Figure 8.10 presents experimental measurements of dome height versus forming time for three biaxial gas-pressure bulge tests run on the University of Texas apparatus. Each test occurred at 450°C and 830 kPa. The only difference between the three tests was the amount of preheat time that the AZ31 blank was exposed to at 450°C prior to the application of gas pressure, which ranged from 30 to 960 s. The data show that the forming time required to reach a particular dome height increases as preheat time increases.

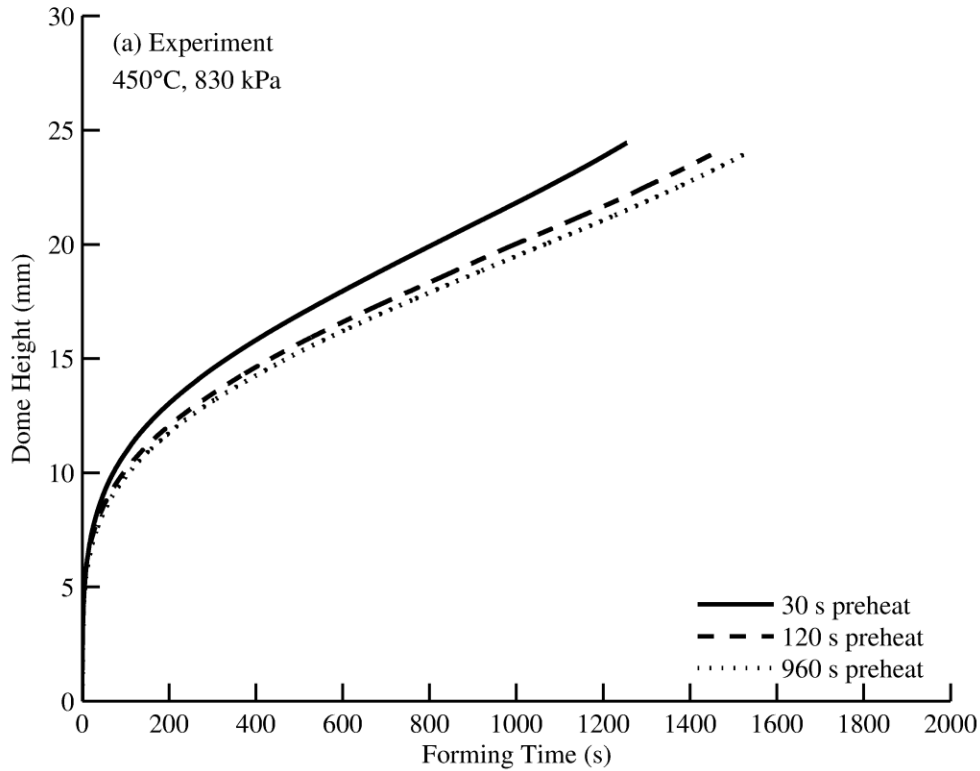


Figure 8.10: Dome height is plotted against forming time for biaxial gas-pressure bulge tests for which only preheat time varied. The experiments use the University of Texas apparatus at 450°C and 830 kPa.

It is hypothesized that the preheat time effect is due to static grain growth, which slows deformation by GBS creep. The GDTDAM material model contains a static grain growth term that calculates the grain size after static grain growth, d_s , as a function of time, t . Therefore, the GDTDAM model can be modified to account for preheat time, t_{pre} , by replacing t with $t + t_{pre}$. This modification increases the time at temperature, t , that the AZ31 blank experiences during simulations, just as preheating increases the time at temperature, t , that the blank experiences during an experiment. Figure 8.11 presents simulation predictions of dome height versus forming time at 450°C and 830 kPa. The

data show that the GDTDAM model predicts the preheat time effect, which is a capability beyond that of the strain-dependent material models.

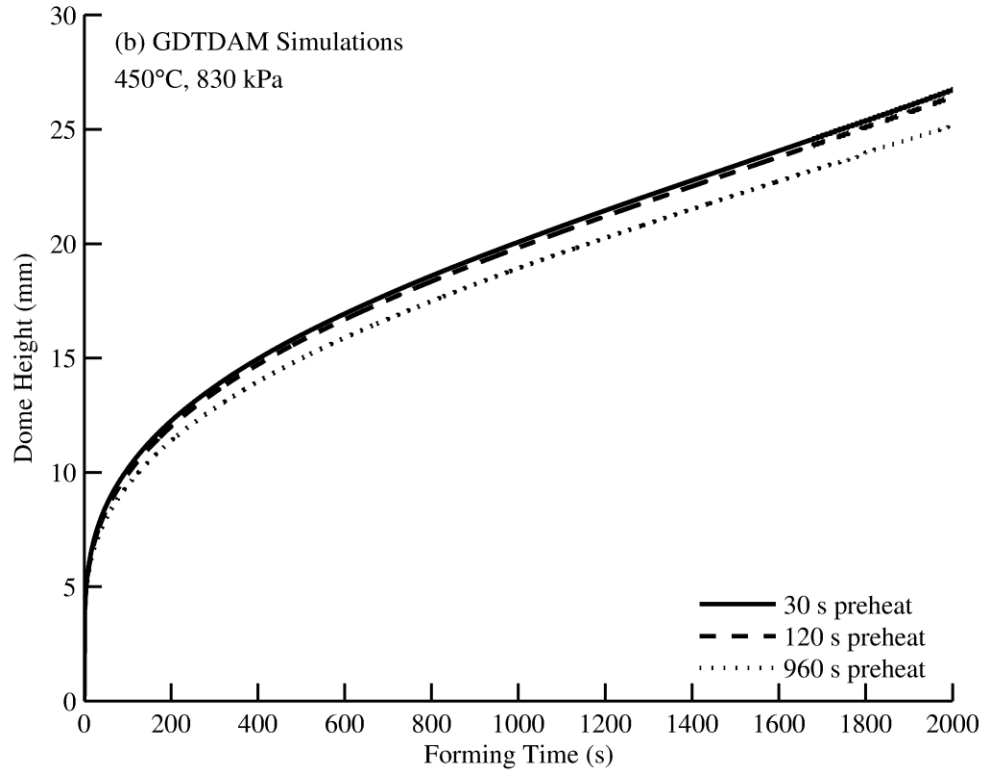


Figure 8.11: Dome height is plotted against forming time for biaxial gas-pressure bulge simulations using the GDTDAM model. All simulations use the University of Texas geometry at 450°C and 830 kPa with only preheat time varying.

Figure 8.12 compares the experimental dome height measurements in Figure 8.10 to the simulation results in Figure 8.11. Comparisons are presented for preheat times of (a) 30, (b) 120, and (c) 960 s. At each preheat time, the RMS and MPD dome height errors were calculated for the GDTDAM material model. These errors are presented in Table 8.9. The results in Figure 8.12 and Table 8.9 indicate that the GDTDAM model accurately predicts the deformation behavior of the AZ31 sheet for various preheat times.

All RMS errors are less than 1.1 mm, while the MPD errors all have absolute values less than 7%. Thus, the GDTDAM material constitutive model provides both qualitative and quantitative predictions of the preheat time effect. Recall that full recrystallization of the AZ31 sheet was observed after 80 s at 450°C, see Figure 4.1. It is possible that the AZ31 sheet did not fully recrystallize after only 30 s at 450°C, which may explain why the error between simulation and experiment is larger for a 30 s preheat than a longer preheat.

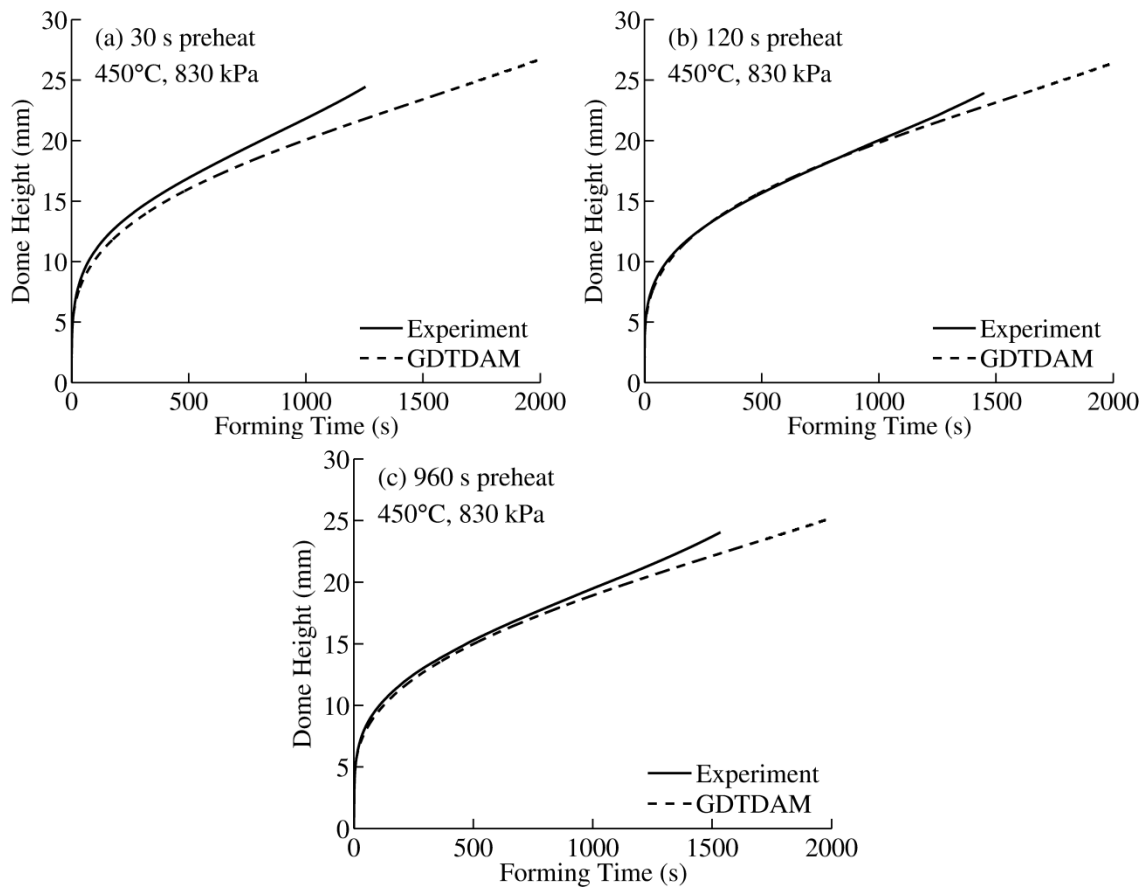


Figure 8.12: Dome height is plotted against forming time at 450°C and 830 kPa for preheat times of (a) 30, (b) 120, and (c) 960 s. Experiments use the University of Texas apparatus, and simulations were conducted using the GDTDAM material model.

Table 8.9: The RMS and MPD errors on dome heights are presented for the GDTDAM material model at 450°C and 830 kPa. Experiments and simulations use the University of Texas geometry, and only preheat time was varied.

Preheat Time (s)	RMS (mm)	MPD (%)
30	1.1	-6.2
120	0.2	-0.5
960	0.5	-2.8

8.3.4. Effects of Initial Grain Size

Because grain size affects GBS creep, it is expected that a change in the initial grain size of the AZ31 sheet material will affect the deformation behavior at 450°C. The grain size of a sheet material is strongly dependent on how it is processed, and different sheet materials, even with the same nominal composition, may have different initial grain sizes. Just as with preheat times, there is no way to easily modify the strain-dependent material constitutive models to account for different initial grain sizes. However, the GDTDAM material model has an initial grain size term, see Equations 48 and 50. The initial grain size, d_o , was estimated to be 8.7 μm for the as-received material. The parameter d_o has physical significance; thus, a new initial grain size can be input into the GDTDAM material model when the initial grain size changes. To investigate this, two new AZ31 sheet materials were created through rolling and annealing processes described in the experimental procedures. The initial grain sizes of the two materials were measured as 6.7 and 19.7 μm , respectively.

Figure 8.13 compares experimental (a) dome heights and (b) pole thicknesses from biaxial gas-pressure bulge tests of these different materials at 280 kPa using the General Motors geometry to simulation results obtained using the GDTDAM material model. Similarly, Figure 8.14 compares experimental (a) dome heights and (b) pole thicknesses from biaxial gas-pressure bulge tests at 520 kPa using the General Motors geometry to simulation results obtained using the GDTDAM material model. At both pressures, experiments and simulations were conducted using the experimentally-measured initial grain sizes of 6.7 and 19.7 μm . Table 8.10 presents the RMS and MPD errors for both dome height and pole thickness at the two pressures of the tests.

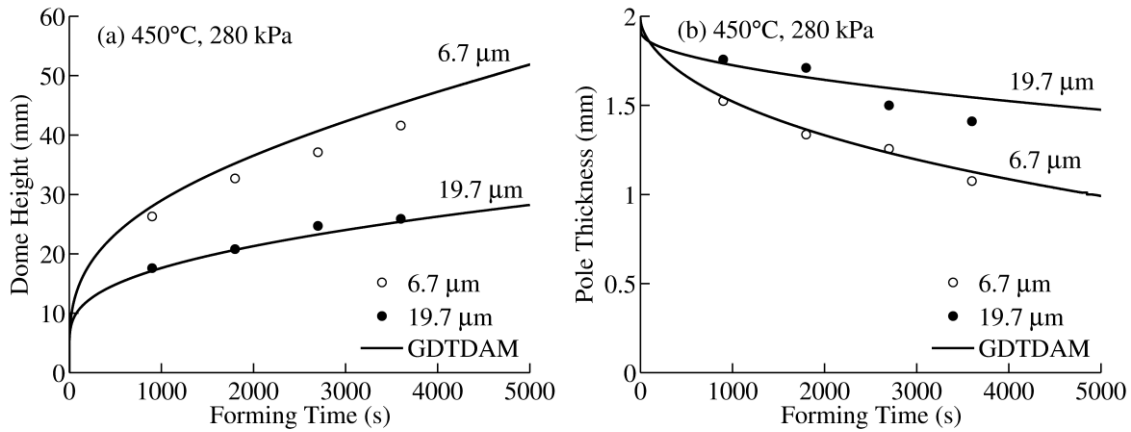


Figure 8.13: (a) Dome height and (b) pole thickness are plotted versus forming time at 450°C and 280 kPa. Experiments use the General Motors apparatus, and simulations were conducted using the GDTDAM material model.

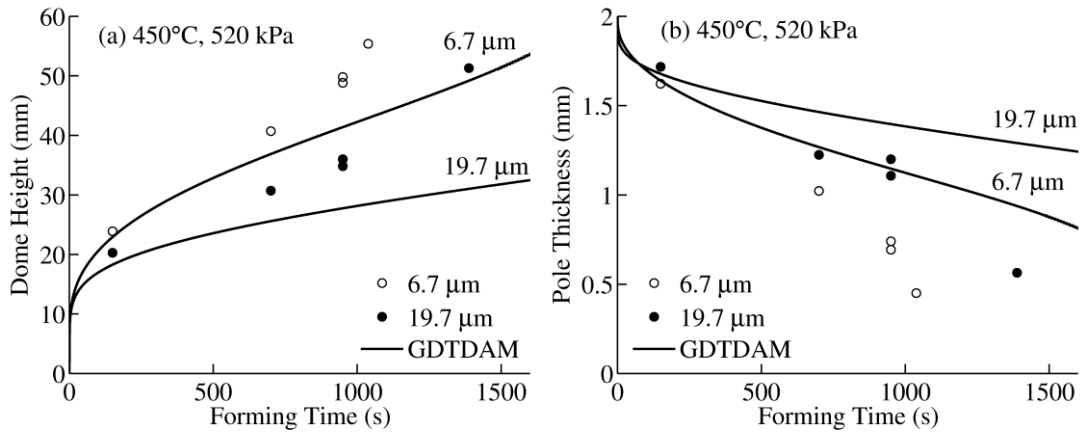


Figure 8.14: (a) Dome height and (b) pole thickness are plotted versus forming time at 450°C and 520 kPa. Experiments use the General Motors apparatus, and simulations were conducted using the GDTDAM material model.

Table 8.10: The RMS and MPD errors on both dome heights and pole thicknesses are presented for the GDTDAM material model at 450°C. Experiments and simulations use the General Motors geometry, and only initial grain size was varied.

Pressure (kPa)	Initial Grain Size (μm)	Dome Height		Pole Thickness	
		RMS (mm)	MPD (%)	RMS (mm)	MPD (%)
280	6.7	2.7	7.9	0.03	0.6
	19.7	0.8	-2.8	0.09	2.9
520	6.7	2.8	-6.8	0.17	12.6
	19.7	6.1	-17.4	0.21	1.6

At 280 kPa, the GDTDAM material model provides accurate predictions of both dome height and pole thickness for the two sheet materials. The MPD errors all have absolute values less than 10% at this pressure, and the RMS dome height errors are less than 2.9 mm. Note that the domes formed from the fine-grained material ($d_o = 6.7 \mu\text{m}$) are more than 10 mm taller than the domes formed from the coarse-grained material ($d_o = 19.7 \mu\text{m}$) for forming times greater than 1500 s. The ability of the GDTDAM model to

predict the deformation behavior of two different sheet materials with these very different forming rates is remarkable. Unfortunately, the GDTDAM model predicts slower forming than experimentally observed in both sheet materials at 520 kPa. This discrepancy could result from the texture of the materials and the resulting plastic anisotropy. The GDTDAM simulations assumed that the anisotropic behavior of the 6.7 and 19.7 μm grain sized materials is the same as the original as-received material. However, the 6.7 and 19.7 μm materials were recrystallized at 350°C. This temperature is lower than the temperature at which the as-received material recrystallizes, 450°C. It is possible that recrystallization at the lower temperature leads to a different texture within the sheet. This texture could be less anisotropic than the texture that develops in the as-received sheet, which would lead to faster forming. Further investigation of this possibility is beyond the scope of this study. However, it should be noted that if the above hypothesis is true, the GDTDAM model can be easily modified to account for the new texture simply by measuring new R-values from tensile specimens, which is much easier than creating a new material constitutive model.

Chapter 9: Conclusions and Future Work

9.1. CONCLUSIONS

Two new material constitutive models describing the deformation behavior of AZ31 sheet at 450°C were created and validated during this investigation. At this temperature, AZ31 deforms by two independent creep mechanisms: GBS creep and DC creep. Grain growth, which affects GBS creep, and anisotropy, which affects DC creep, were studied during the creation of the new material models. AZ31 exhibits both static and dynamic grain growth at 450°C. Static grain growth depends on time at temperature, while dynamic grain growth depends on true strain. Thus, grain growth in the material can be modeled as a function of both time and strain. A grain size model was used to create a grain-size dependent tensile data (GDTD) material constitutive model. This model provides a more physical basis for GBS creep hardening than a previous strain-dependent tensile data (SDTD) material model.

Both the GDTD and SDTD material models were modified to account for the normal anisotropy exhibited by the AZ31 sheet. This anisotropy is mechanism-dependent, such that DC creep is anisotropic while GBS creep is isotropic. An appropriate anisotropic equivalent stress, such as the Hill stress, must be calculated when predicting the deformation behavior of an anisotropic material. The coefficients in the Hill stress formula are functions of R-values measured during tensile tests. The resulting GDTDAM and SDTDAM material models each require two different equivalent stresses because of the mechanism-dependent anisotropy. Both of these models were then

implemented in the finite-element-method software Abaqus and used in simulations. The simulation results were compared to experimental data from both tensile tests and biaxial gas-pressure bulge tests to evaluate the accuracy of the two material models.

Simulation results confirm that the anisotropy of the AZ31 sheet must be accounted for to predict the forming behavior under multiple stress states. Previous material models, such as the SDTD and SDTDM1 models, can only predict forming behavior for one of these stress state. The SDTD model accurately predicts the uniaxial stress-strain behavior of AZ31 at 450°C. However, it cannot accurately predict deformation perpendicular to the tensile direction, nor can it predict biaxial deformation behavior, because it does not account for plastic anisotropy. Conversely, the SDTDM1 model accurately predicts the biaxial deformation of Mg AZ31 at 450°C. However, it cannot predict uniaxial deformation behavior because the 1.3 factor only accounts for anisotropy during biaxial deformation, and does so quite crudely. The anisotropy modification present in the GDTDAM and SDTDAM material models allows for accurate predictions of the plastic deformation of Mg AZ31 sheet at 450°C under both uniaxial and biaxial stress states in the range of thinning up to about 40%, which is typically the range of greatest practical interest for hot gas-pressure forming of automotive panels. This ability represents a significant improvement over the SDTD and SDTDM1 models. Complex stress states develop during the hot forming of automotive body closure panels. The SDTDAM and GDTDAM material models are the only models investigated that can account for the variety of stress states expected in forming practice.

The strain-dependent material models cannot be modified to account for microstructural changes that affect GBS creep, because the strain-dependent functions in these models have no physical basis. However, the GDTDAM model, which models GBS creep hardening as a function of grain size, can be modified to account for the effects of microstructure evolution on deformation behavior. For example, an increase in preheat time prior to forming leads to a decrease in forming rate. The time variable in the GDTDAM model can be advanced by the corresponding preheat time to provide qualitative and quantitative predictions of the preheat time effect. The GDTDAM model can even be modified to predict the deformation behavior of AZ31 sheet materials with different initial grain sizes. This modification is far beyond the capabilities of the strain-dependent material models, and it works especially well when predicting biaxial deformation behavior at low gas pressures, where potential differences in R-values, associated with DC creep, between different materials are of less importance.

9.2. FUTURE WORK

The material constitutive models created during this study provide accurate predictions of AZ31 forming behavior at 450°C. However, they do not provide information about the deformation of AZ31 at other temperatures. It may be advantageous to form automotive and aerospace components at lower temperatures. When parts are formed at high temperature, they may distort when removed quickly from the die [36]. In addition, higher-temperature forming requires a high energy input and may, under some circumstances, produce abnormal grains within the formed part.

Abnormal grains have a deleterious effect on yield strength [95]. A material constitutive model that could predict deformation over a range of temperatures would therefore be useful. For example, it could be used in FEM simulations to determine the optimum temperature for a forming operation. However, such material models require a better understanding of how phenomena such as grain growth and anisotropy vary with temperature, as well as identification of the mechanisms governing deformation over the temperature range of interest. Such work would provide improved predictive capabilities that could be applied to real-world commercial forming operations.

Material constitutive models may be improved through investigations of phenomena such as cavitation that affect deformation at large strains. These phenomena are the likely reason that simulation predictions diverge from experimental data as the material approaches failure. However, it should be noted that cavitation also negatively affects material properties, and a part with as little as 2% cavitation may be unacceptable [96]. Thus, investigation into the effects of severe cavitation damage on deformation behavior may only be of limited usefulness.

The results of this investigation suggest that the SDTDAM and GDTDAM material models can accurately predict deformation under multiple stress states. However, these material models must be shown to predict the forming of the complex components required in automotive and aerospace applications if they are to be fully trusted. Future work should include FEM simulations of the forming of magnesium vehicle closure panels. These simulations represent the final test for the SDTDAM and GDTDAM material constitutive models. If the material models can predict the forming of

actual commercial components, then they will have proven their worth and succeeded in the job for which they were created.

Appendix A: Effects of Specimen Geometry on R-value

During the course of this investigation, R-value measurements were used to quantify the plastic anisotropy of the AZ31 sheet material. It was assumed that the R-values are constants describing anisotropic deformation from a particular measurement at a particular temperature. For this assumption to hold, R-values must not depend on the specimen width-to-thickness ratio. Finite-element-method (FEM) simulations were conducted to investigate whether or not the width-to-thickness ratio has an effect. These simulations utilized two tensile meshes. One is the tensile mesh described in Chapter 7, with a width of 6 mm and thickness of 2 mm, which corresponds to a width-to-thickness ratio of 3. The second mesh was created from the first by reducing the width of the initial mesh by two-thirds. This results in a mesh with a width of 2 mm and a thickness of 2 mm, which corresponds to a width-to-thickness ratio of 1. Each mesh was used in FEM simulations using the SDTD and SDTDAM material models. Simulations were conducted at 10^{-3} s^{-1} to a final true strain of 0.6. The SDTD material model resulted in an R-value of 1.0 for both meshes, as expected for isotropic deformation. The SDTDAM material model resulted in an R-value of 1.38 for both meshes. These results suggest that the specimen width-to-thickness ratio has no effect on measured R-values for uniaxial deformation.

However, specimen geometry can affect R-values measured from tensile specimens. Each tensile specimen has a wider grip at each end of its gage region. This

grip imposes a constraint on the ends of the gage region, which affects the resulting strains near the grip. To mimic this constraint, the nodes at each end of both tensile meshes were fixed such that the width of the specimen cannot decrease at these locations. Simulations were again conducted for a true-strain rate of 10^{-3} s^{-1} to a final true strain of 0.6 using the SDTD and SDTDAM material constitutive models. After completion of the simulations, R-values were obtained from the deformed meshes at various distances from the end of the mesh, which represents the location at which the gage region meets the specimen grips. These R-values are shown in Figure A.1. The figure indicates that R-values measured near the grip may be different from those measured away from the grip. The constraint imposed by the grip on the gage region results in a non-uniaxial stress state near the grip. The distance beyond which constant R-values are measured is approximately equal to the gage width. This indicates that accurate R-values can be measured from a specimen with a gage width of 6 mm, but a much wider specimen could provide inaccurate R-values.

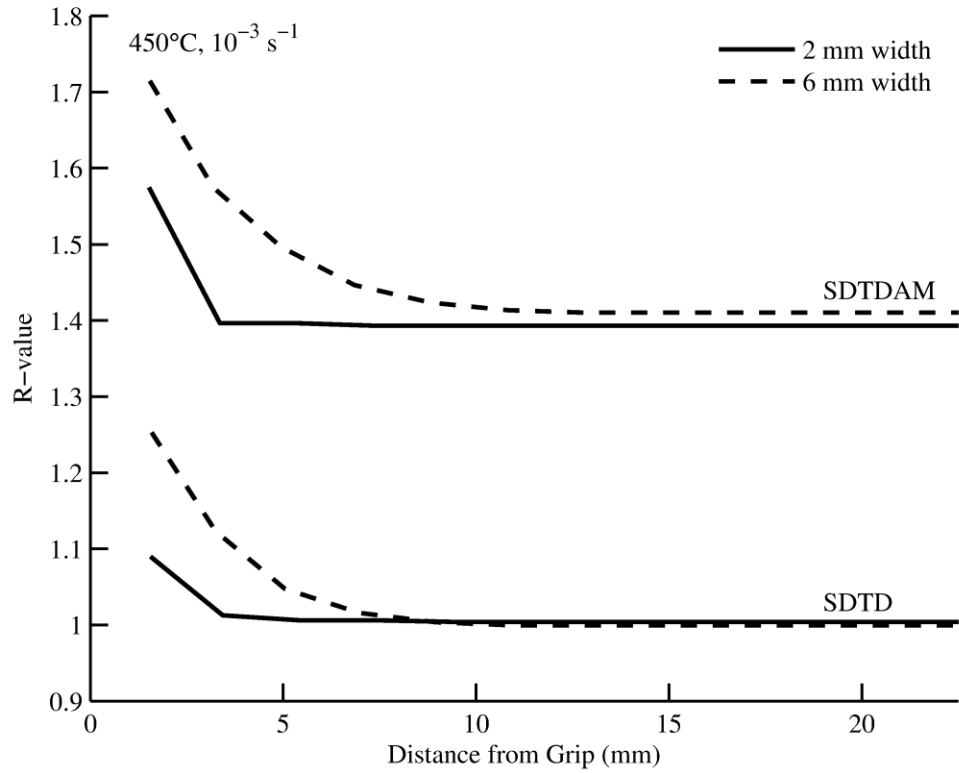


Figure A.1: R-values are plotted against the distance from the end of the tensile mesh, which represents the distance from the grip in an actual tensile test. Simulations were conducted using the SDTD and SDTDAM material models at 10^{-3} s^{-1} to a final true strain of 0.6.

Appendix B: User-Defined Code for Material Constitutive Models

This appendix contains the user-defined functions required to implement the GDTDAM and SDTDAM material constitutive models in the FEM software package AbaqusTM. Each model's code can be used in Abaqus FEM simulations when placed within a computer file named creep.f. Note that the GDTDAM model can be modified to account for changes in preheat time (tpre) and initial grain size (do) by changing the bolded values in the code. All code was written in the programming language Fortran.

GDTDAM MATERIAL CONSTITUTIVE MODEL

```
SUBROUTINE USDFLD(FIELD, STATEV, PNEWDT, DIRECT, T, CELENT,  
1 TIME, DTIME, CMNAME, ORNAME, NFIELD, NSTATV, NOEL, NPT, LAYER,  
2 KSPT, KSTEP, KINC, NDI, NSHR, COORD, JMAC, JMATYP, MATLAYO, LACCFLA)  
C  
    INCLUDE 'ABA_PARAM.INC'  
C  
    CHARACTER*80 CMNAME, ORNAME  
    CHARACTER*3  FLGRAY(15)  
    DIMENSION FIELD(NFIELD), STATEV(NSTATV), DIRECT(3,3),  
1 T(3,3), TIME(2)  
    DIMENSION ARRAY(15), JARRAY(15), JMAC(*), JMATYP(*), COORD(*)  
  
C Get the components of the stress tensor (stored in array ARRAY)  
    CALL GETVRM('S', ARRAY, JARRAY, FLGRAY, JRCD, JMAC, JMATYP, MATLAYO,  
1 LACCFLA)  
  
C Input R-values for creep mechanisms 1 and 2  
    R1 = 1.0  
    R2 = 1.86  
  
C Calculate Hill stress for creep mechanism 1  
C Assumes plane stress and normal anisotropy  
    STATEV(1) = SQRT(1/(1+R1)*ARRAY(2)**2+1/(1+R1)*(-ARRAY(1))**2+  
1 R1/(1+R1)*(ARRAY(1)-ARRAY(2))**2+2*(1+R1/(1+R1))*ARRAY(4)**2)  
  
C Calculate Hill stress for creep mechanism 2  
C Assumes plane stress and normal anisotropy
```



```

STATEV(2) = SQRT(1/(1+R2)*ARRAY(2)**2+1/(1+R2)*(-ARRAY(1))**2+
1 R2/(1+R2)*(ARRAY(1)-ARRAY(2))**2+2*(1+R2/(1+R2))*ARRAY(4)**2)

C Stores the effective R-value as a field variable
C Needed to calculate the appropriate stress ratios in the input
file
FIELD(1)=STATEV(3)

RETURN
END

C
C constitutive equation
C de/dt = A1/d^p*sigma1^n1+A2*sigma2^n2
C A1 = 0.0476
C p = 3.13
C n1 = 1.29
C A2 = 3.12E-10
C n2 = 5.73
C d = ds*exp(0.540*EC(2))
C ds = [8.74^(1/0.0457)+1.07E20*TIME(2)]^0.0457
C
C
SUBROUTINE CREEP(DECRA,DESWA,STATEV,SERD,EC,ESW,P,QTILD,
1 TEMP,DTEMP,PREDEF,DPRED,TIME,DTIME,CMNAME,LEXIMP,LEND,
2 COORDS,NSTATV,NOEL,NPT,LAYER,KSPT,KSTEP,KINC)
C
C INCLUDE 'ABA_PARAM.INC'
C
C CHARACTER*80 CMNAME
C
C DIMENSION DECRA(5),DESWA(5),STATEV(*),PREDEF(*),DPRED(*),
1 TIME(2),EC(2),ESW(2),COORDS(*)

C=====
C===
C-----
C-----
C----- DEFINITION OF CREEP CONSITUTIVE LAW -----
C-----
C----- POWER MODEL -----
C-----
C-----
C=====
C===
C
C VARIABLES TO BE DEFINED :
C -----
C--- In all cases
C DECRA(1) :
```

```

C  DESWA(1)  :
C---  For implicit creep integration (LEXIMP=1, see below)
C  DECRA(2)  :
C  DECRA(3)  :
C  DECRA(4)  :
C  DECRA(5)  :
C  DESWA(2)  :
C  DESWA(3)  :
C  DESWA(4)  :
C  DESWA(5)  :
C
C  VARIABLES THAT CAN BE UPDATED :
C  -----
C  STATEV    : Array containing the user-defined solution-dependent
state variables.
C  SERD      : Magnitude of the strain energy rate density Wdot.
C
C  VARIABLES PASSED IN FOR INFORMATION :
C  -----
C  EC(1)     : Creep 'Ecr' at the start of the increment.
C  EC(2)     : Creep 'Ecr' at the end of the increment.
C  ESW(1)    : Creep 'Esw' at the start of the increment.
C  ESW(2)    : Creep 'Esw' at the end of the increment.
C  P         : Equivalent pressure stress.
C  QTILD     : Mises or Hill equivalent stress.
C  TEMP      : Temperature at the end of the increment.
C  DTEMP     : Increment of temperature during the time increment.
C  PREDEF    : Array containing the values of all of the predefined
variables.
C  DPRED     : An array containing the increments of all of the
predefined variables during the time increment.
C  TIME(1)   : Value of step time at the end of the increment.
C  TIME(2)   : Value of total time at the end of the increment.
C  DTIME     : Time increment.
C  CMNAME    : Material name given on the *MATERIAL option.
C  LEXIMP    : Explicit/implicit flag.
C  LEND      : Start/end of increment flag.
C  COORDS(3) : An array containing the current coordinates of this
point.
C  NSTATV    : Number of solution-dependent state variables
associated with this material.
C  NOEL      : Element number.
C  NPT       : Integration point number.
C  LAYER     : Layer number (for composite shells and layered
solids).
C  KSPT      : Section point number within the current layer.
C  KSTEP     : Step number.
C  KINC      : Increment number.
C

```

```

C-----
---+
C-----
---+
C----- DECLARATIONS -----
---*
C-----
---+
      PARAMETER (dzero=1.D-20)
C
C-----
---+
C-----
---+
C----- BEGINNING OF EXECUTABLE CODE -----
---*
C-----
---+
C-----
---+
C
      A1 = 0.0476
      dn1 = 1.29
      A2 = 3.12D-10
      dn2 = 5.73
      do = 8.74
      tpre = 0.0
      davg = ((do**(1/0.0457)+1.07D20*(TIME(2)+tpre))**0.0457)
1 *EXP(0.540*EC(2))
      dp = 3.13
C-----
---+
C----- Metal creep: Equivalent (uniaxial) deviatoric creep strain
increment.

DECRA(1)=(A1/(davg**dp)*STATEV(1)**dn1+A2*STATEV(2)**dn2)*DTIME
C-----
---+
C----- Metal creep: Derivative
C----- DECRA(2): D(de^cr)/D(e^cr)
C----- DECRA(5): D(de^cr)/D(q)

C Calculate the appropriate derivatives of the creep strain
increment
      IF(LEXIMP.EQ.1) THEN
      DdDe = ((do**(1/0.0457)+1.07D20*(TIME(2)+tpre))**(-0.9543))
1 *0.0457*1.07D20*EXP(0.540*EC(2)) / (DECRA(1)/DTIME)
2 + ((do**(1/0.0457)+1.07D20*(TIME(2)+tpre))**0.0457)
3 *EXP(0.540*EC(2))
      DECRA(2)=-dp*A1*davg**(-dp-1)*STATEV(1)**dn1*DdDe

```

```

    DECRA(5)=(dn1*A1/(davg**dp)*STATEV(1)**(dn1-1.D0)+
1 dn2*A2*STATEV(2)**(dn2-1.D0))*DTIME

    END IF

C Input R-values for creep mechanisms 1 and 2
    R1 = 1.0
    R2 = 1.86

C Calculate the effective R-value
C Based on the ratio of mechanism 2 strain rate to total strain rate
    SRR=(A2*STATEV(2)**dn2)/
1 (A1/(davg**dp)*STATEV(1)**dn1+A2*STATEV(2)**dn2)
    STATEV(3)=((R2/(1+R2)-R1/(1+R1))*SRR+R1/(1+R1))/
1 ((1/(1+R2)-1/(1+R1))*SRR+1/(1+R1))

    RETURN
    END

```

SDTDAM MATERIAL CONSTITUTIVE MODEL

```

    SUBROUTINE USDFLD(FIELD,STATEV,PNEWDT,DIRECT,T,CELENT,
1 TIME,DTIME,CMNAME,ORNAME,NFIELD,NSTATV,NOEL,NPT,LAYER,
2 KSPT,KSTEP,KINC,NDI,NSHR,COORD,JMAC,JMATYP,MATLAYO,LACCFLA)
C
    INCLUDE 'ABA_PARAM.INC'
C
    CHARACTER*80 CMNAME,ORNAME
    CHARACTER*3 FLGRAY(15)
    DIMENSION FIELD(NFIELD),STATEV(NSTATV),DIRECT(3,3),
1 T(3,3),TIME(2)
    DIMENSION ARRAY(15),JARRAY(15),JMAC(*),JMATYP(*),COORD(*)

C Get the components of the stress tensor (stored in array ARRAY)
    CALL GETVRM('S',ARRAY,JARRAY,FLGRAY,JRCD,JMAC,JMATYP,MATLAYO,
1 LACCFLA)

C Input R-values for creep mechanisms 1 and 2
    R1 = 1.0
    R2 = 1.87

C Calculate Hill stress for creep mechanism 1
C Assumes plane stress and normal anisotropy
    STATEV(1) = SQRT(1/(1+R1)*ARRAY(2)**2+1/(1+R1)*(-ARRAY(1))**2+
1 R1/(1+R1)*(ARRAY(1)-ARRAY(2))**2+2*(1+R1/(1+R1))*ARRAY(4)**2)

C Calculate Hill stress for creep mechanism 2
C Assumes plane stress and normal anisotropy

```

```

STATEV(2) = SQRT(1/(1+R2)*ARRAY(2)**2+1/(1+R2)*(-ARRAY(1))**2+
1 R2/(1+R2)*(ARRAY(1)-ARRAY(2))**2+2*(1+R2/(1+R2))*ARRAY(4)**2)

C Stores the effective R-value as a field variable
C Needed to calculate the appropriate stress ratios in the input
file
FIELD(1)=STATEV(3)

RETURN
END

C
C constitutive equation
C de/dt = A1(e)*sigma1^n1(e)+A2*sigma2^n2
C A1(e) = exp(-9.97333-12.5909e+17.8488e^2-11.0985e^3)
C n1(3) = 1.3325+0.667476tanh(4.6266e)
C
C
SUBROUTINE CREEP(DECRA,DESWA,STATEV,SERD,EC,ESW,P,QTILD,
1 TEMP,DTEMP,PRED,DPRED,TIME,DTIME,CMNAME,LEXIMP,LEND,
2 COORDS,NSTATV,NOEL,NPT,LAYER,KSPT,KSTEP,KINC)
C
INCLUDE 'ABA_PARAM.INC'
C
CHARACTER*80 CMNAME
C
DIMENSION DECRA(5),DESWA(5),STATEV(*),PRED(*),DPRED(*),
1 TIME(2),EC(2),ESW(2),COORDS(*)

C=====
C====
C-----
C-----
C----- DEFINITION OF CREEP CONSITUTIVE LAW -----
C-----
C----- POWER MODEL -----
C-----
C-----
C=====
C====
C
C VARIABLES TO BE DEFINED :
C -----
C--- In all cases
C DECRA(1) :
C DESWA(1) :
C--- For implicit creep integration (LEXIMP=1, see below)
C DECRA(2) :
C DECRA(3) :
C DECRA(4) :

```

```

C  DECRA(5)  :
C  DESWA(2)  :
C  DESWA(3)  :
C  DESWA(4)  :
C  DESWA(5)  :
C
C  VARIABLES THAT CAN BE UPDATED :
C  -----
C  STATEV    : Array containing the user-defined solution-dependent
state variables.
C  SERD      : Magnitude of the strain energy rate density Wdot.
C
C  VARIABLES PASSED IN FOR INFORMATION :
C  -----
C  EC(1)     : Creep 'Ecr' at the start of the increment.
C  EC(2)     : Creep 'Ecr' at the end of the increment.
C  ESW(1)    : Creep 'Esw' at the start of the increment.
C  ESW(2)    : Creep 'Esw' at the end of the increment.
C  P         : Equivalent pressure stress.
C  QTILD     : Mises or Hill equivalent stress.
C  TEMP      : Temperature at the end of the increment.
C  DTEMP     : Increment of temperature during the time increment.
C  PREDEF    : Array containing the values of all of the predefined
variables.
C  DPRED     : An array containing the increments of all of the
predefined variables during the time increment.
C  TIME(1)   : Value of step time at the end of the increment.
C  TIME(2)   : Value of total time at the end of the increment.
C  DTIME     : Time increment.
C  CMNAME    : Material name given on the *MATERIAL option.
C  LEXIMP    : Explicit/implicit flag.
C  LEND      : Start/end of increment flag.
C  COORDS(3) : An array containing the current coordinates of this
point.
C  NSTATV    : Number of solution-dependent state variables
associated with this material.
C  NOEL      : Element number.
C  NPT       : Integration point number.
C  LAYER     : Layer number (for composite shells and layered
solids).
C  KSPT      : Section point number within the current layer.
C  KSTEP     : Step number.
C  KINC      : Increment number.
C
C-----
---+
C-----
---+
C-----  DECLARATIONS  -----
---*

```

```

C-----
---+
      PARAMETER (dzero=1.D-20)
C
C-----
---+
C-----
---+
C----- BEGINNING OF EXECUTABLE CODE -----
---*
C-----
---+
C-----
---+
C
      A1 = exp(-9.9733-12.5909*EC(2)+17.8488*EC(2)**2-
11.0985*EC(2)**3)
      dn1 = 1.3325+0.667476*tanh(4.6266*EC(2))
      A2 = 5.9D-10
      dn2 = 5.53
C-----
---+
C----- Metal creep: Equivalent (uniaxial) deviatoric creep strain
increment.
      DECRA(1)=(A1*STATEV(1)**dn1+A2*STATEV(2)**dn2)*DTIME
C-----
---+
C----- Metal creep: Derivative
C----- DECRA(2): D(de^cr)/D(e^cr)
C----- DECRA(5): D(de^cr)/D(q)

C Calculate the appropriate derivatives of the creep strain
increment
      IF(LEXIMP.EQ.1) THEN
        DA1De = A1*(-12.5909+2*17.8488*EC(2)-3*11.0985*EC(2)**2)
        Ddn1De = 0.667476*4.6266*(1.D0-tanh(4.6266*EC(2))**2)
        DECRA(2)=(DA1De+A1*log(STATEV(1)+dzero)*Ddn1De)*
1 STATEV(1)**dn1*DTIME
        DECRA(5)=(dn1*A1*STATEV(1)**(dn1-1.D0)+
1 dn2*A2*STATEV(2)**(dn2-1.D0))*DTIME

      END IF

C Input R-values for creep mechanisms 1 and 2
      R1 = 1.0
      R2 = 1.87

C Calculate the effective R-value
C Based on the ratio of mechanism 2 strain rate to total strain rate
      SRR=(A2*STATEV(2)**dn2)/(A1*STATEV(1)**dn1+A2*STATEV(2)**dn2)

```

```
STATEV(3)=( (R2/(1+R2)-R1/(1+R1))*SRR+R1/(1+R1))/  
1  ((1/(1+R2)-1/(1+R1))*SRR+1/(1+R1))
```

```
RETURN
```

```
END
```


Appendix C: Abaqus Input Files

This appendix contains example input files used to simulate tensile forming and biaxial gas-pressure bulge forming in the FEM software package AbaqusTM. The example tensile input file assumes a true-strain rate of 10^{-4} s^{-1} , the example University of Texas bulge forming input file assumes a pressure of 830 kPa, and the example General Motors bulge forming input file assumes a pressure of 520 kPa. However, these files can be easily modified to predict forming at different true-strain rates or gas pressures.

EXAMPLE TENSILE INPUT FILE

```
*NODE
1      ,      0      ,      0      ,      0
2      ,      1      ,      0      ,      0
3      ,      2      ,      0      ,      0
4      ,      3      ,      0      ,      0
5      ,      4      ,      0      ,      0
6      ,      5      ,      0      ,      0
7      ,      6      ,      0      ,      0
8      ,      0      ,      1      ,      0
9      ,      1      ,      1      ,      0
10     ,      2      ,      1      ,      0
11     ,      3      ,      1      ,      0
12     ,      4      ,      1      ,      0
13     ,      5      ,      1      ,      0
14     ,      6      ,      1      ,      0
15     ,      0      ,      2      ,      0
16     ,      1      ,      2      ,      0
17     ,      2      ,      2      ,      0
18     ,      3      ,      2      ,      0
19     ,      4      ,      2      ,      0
20     ,      5      ,      2      ,      0
21     ,      6      ,      2      ,      0
22     ,      0      ,      3      ,      0
23     ,      1      ,      3      ,      0
24     ,      2      ,      3      ,      0
25     ,      3      ,      3      ,      0
26     ,      4      ,      3      ,      0
```

27	,	5	,	3	,	0
28	,	6	,	3	,	0
29	,	0	,	4	,	0
30	,	1	,	4	,	0
31	,	2	,	4	,	0
32	,	3	,	4	,	0
33	,	4	,	4	,	0
34	,	5	,	4	,	0
35	,	6	,	4	,	0
36	,	0	,	5	,	0
37	,	1	,	5	,	0
38	,	2	,	5	,	0
39	,	3	,	5	,	0
40	,	4	,	5	,	0
41	,	5	,	5	,	0
42	,	6	,	5	,	0
43	,	0	,	6	,	0
44	,	1	,	6	,	0
45	,	2	,	6	,	0
46	,	3	,	6	,	0
47	,	4	,	6	,	0
48	,	5	,	6	,	0
49	,	6	,	6	,	0
50	,	0	,	7	,	0
51	,	1	,	7	,	0
52	,	2	,	7	,	0
53	,	3	,	7	,	0
54	,	4	,	7	,	0
55	,	5	,	7	,	0
56	,	6	,	7	,	0
57	,	0	,	8	,	0
58	,	1	,	8	,	0
59	,	2	,	8	,	0
60	,	3	,	8	,	0
61	,	4	,	8	,	0
62	,	5	,	8	,	0
63	,	6	,	8	,	0
64	,	0	,	9	,	0
65	,	1	,	9	,	0
66	,	2	,	9	,	0
67	,	3	,	9	,	0
68	,	4	,	9	,	0
69	,	5	,	9	,	0
70	,	6	,	9	,	0
71	,	0	,	10	,	0
72	,	1	,	10	,	0
73	,	2	,	10	,	0
74	,	3	,	10	,	0
75	,	4	,	10	,	0
76	,	5	,	10	,	0

77	,	6	,	10	,	0
78	,	0	,	11	,	0
79	,	1	,	11	,	0
80	,	2	,	11	,	0
81	,	3	,	11	,	0
82	,	4	,	11	,	0
83	,	5	,	11	,	0
84	,	6	,	11	,	0
85	,	0	,	12	,	0
86	,	1	,	12	,	0
87	,	2	,	12	,	0
88	,	3	,	12	,	0
89	,	4	,	12	,	0
90	,	5	,	12	,	0
91	,	6	,	12	,	0
92	,	0	,	13	,	0
93	,	1	,	13	,	0
94	,	2	,	13	,	0
95	,	3	,	13	,	0
96	,	4	,	13	,	0
97	,	5	,	13	,	0
98	,	6	,	13	,	0
99	,	0	,	14	,	0
100	,	1	,	14	,	0
101	,	2	,	14	,	0
102	,	3	,	14	,	0
103	,	4	,	14	,	0
104	,	5	,	14	,	0
105	,	6	,	14	,	0
106	,	0	,	15	,	0
107	,	1	,	15	,	0
108	,	2	,	15	,	0
109	,	3	,	15	,	0
110	,	4	,	15	,	0
111	,	5	,	15	,	0
112	,	6	,	15	,	0
113	,	0	,	16	,	0
114	,	1	,	16	,	0
115	,	2	,	16	,	0
116	,	3	,	16	,	0
117	,	4	,	16	,	0
118	,	5	,	16	,	0
119	,	6	,	16	,	0
120	,	0	,	17	,	0
121	,	1	,	17	,	0
122	,	2	,	17	,	0
123	,	3	,	17	,	0
124	,	4	,	17	,	0
125	,	5	,	17	,	0
126	,	6	,	17	,	0

127	,	0	,	18	,	0
128	,	1	,	18	,	0
129	,	2	,	18	,	0
130	,	3	,	18	,	0
131	,	4	,	18	,	0
132	,	5	,	18	,	0
133	,	6	,	18	,	0
134	,	0	,	19	,	0
135	,	1	,	19	,	0
136	,	2	,	19	,	0
137	,	3	,	19	,	0
138	,	4	,	19	,	0
139	,	5	,	19	,	0
140	,	6	,	19	,	0
141	,	0	,	20	,	0
142	,	1	,	20	,	0
143	,	2	,	20	,	0
144	,	3	,	20	,	0
145	,	4	,	20	,	0
146	,	5	,	20	,	0
147	,	6	,	20	,	0
148	,	0	,	21	,	0
149	,	1	,	21	,	0
150	,	2	,	21	,	0
151	,	3	,	21	,	0
152	,	4	,	21	,	0
153	,	5	,	21	,	0
154	,	6	,	21	,	0
155	,	0	,	22	,	0
156	,	1	,	22	,	0
157	,	2	,	22	,	0
158	,	3	,	22	,	0
159	,	4	,	22	,	0
160	,	5	,	22	,	0
161	,	6	,	22	,	0
162	,	0	,	23	,	0
163	,	1	,	23	,	0
164	,	2	,	23	,	0
165	,	3	,	23	,	0
166	,	4	,	23	,	0
167	,	5	,	23	,	0
168	,	6	,	23	,	0
169	,	0	,	24	,	0
170	,	1	,	24	,	0
171	,	2	,	24	,	0
172	,	3	,	24	,	0
173	,	4	,	24	,	0
174	,	5	,	24	,	0
175	,	6	,	24	,	0
176	,	0	,	25	,	0

177	,	1	,	25	,	0
178	,	2	,	25	,	0
179	,	3	,	25	,	0
180	,	4	,	25	,	0
181	,	5	,	25	,	0
182	,	6	,	25	,	0
*ELEMENT, TYPE=M3D4, ELSET=SHEET						
1	,	1	,	8	,	9
2	,	2	,	9	,	10
3	,	3	,	10	,	11
4	,	4	,	11	,	12
5	,	5	,	12	,	13
6	,	6	,	13	,	14
7	,	8	,	15	,	16
8	,	9	,	16	,	17
9	,	10	,	17	,	18
10	,	11	,	18	,	19
11	,	12	,	19	,	20
12	,	13	,	20	,	21
13	,	15	,	22	,	23
14	,	16	,	23	,	24
15	,	17	,	24	,	25
16	,	18	,	25	,	26
17	,	19	,	26	,	27
18	,	20	,	27	,	28
19	,	22	,	29	,	30
20	,	23	,	30	,	31
21	,	24	,	31	,	32
22	,	25	,	32	,	33
23	,	26	,	33	,	34
24	,	27	,	34	,	35
25	,	29	,	36	,	37
26	,	30	,	37	,	38
27	,	31	,	38	,	39
28	,	32	,	39	,	40
29	,	33	,	40	,	41
30	,	34	,	41	,	42
31	,	36	,	43	,	44
32	,	37	,	44	,	45
33	,	38	,	45	,	46
34	,	39	,	46	,	47
35	,	40	,	47	,	48
36	,	41	,	48	,	49
37	,	43	,	50	,	51
38	,	44	,	51	,	52
39	,	45	,	52	,	53
40	,	46	,	53	,	54
41	,	47	,	54	,	55
42	,	48	,	55	,	56
43	,	50	,	57	,	58

44	,	51	,	58	,	59	,	52
45	,	52	,	59	,	60	,	53
46	,	53	,	60	,	61	,	54
47	,	54	,	61	,	62	,	55
48	,	55	,	62	,	63	,	56
49	,	57	,	64	,	65	,	58
50	,	58	,	65	,	66	,	59
51	,	59	,	66	,	67	,	60
52	,	60	,	67	,	68	,	61
53	,	61	,	68	,	69	,	62
54	,	62	,	69	,	70	,	63
55	,	64	,	71	,	72	,	65
56	,	65	,	72	,	73	,	66
57	,	66	,	73	,	74	,	67
58	,	67	,	74	,	75	,	68
59	,	68	,	75	,	76	,	69
60	,	69	,	76	,	77	,	70
61	,	71	,	78	,	79	,	72
62	,	72	,	79	,	80	,	73
63	,	73	,	80	,	81	,	74
64	,	74	,	81	,	82	,	75
65	,	75	,	82	,	83	,	76
66	,	76	,	83	,	84	,	77
67	,	78	,	85	,	86	,	79
68	,	79	,	86	,	87	,	80
69	,	80	,	87	,	88	,	81
70	,	81	,	88	,	89	,	82
71	,	82	,	89	,	90	,	83
72	,	83	,	90	,	91	,	84
73	,	85	,	92	,	93	,	86
74	,	86	,	93	,	94	,	87
75	,	87	,	94	,	95	,	88
76	,	88	,	95	,	96	,	89
77	,	89	,	96	,	97	,	90
78	,	90	,	97	,	98	,	91
79	,	92	,	99	,	100	,	93
80	,	93	,	100	,	101	,	94
81	,	94	,	101	,	102	,	95
82	,	95	,	102	,	103	,	96
83	,	96	,	103	,	104	,	97
84	,	97	,	104	,	105	,	98
85	,	99	,	106	,	107	,	100
86	,	100	,	107	,	108	,	101
87	,	101	,	108	,	109	,	102
88	,	102	,	109	,	110	,	103
89	,	103	,	110	,	111	,	104
90	,	104	,	111	,	112	,	105
91	,	106	,	113	,	114	,	107
92	,	107	,	114	,	115	,	108
93	,	108	,	115	,	116	,	109

94	,	109	,	116	,	117	,	110
95	,	110	,	117	,	118	,	111
96	,	111	,	118	,	119	,	112
97	,	113	,	120	,	121	,	114
98	,	114	,	121	,	122	,	115
99	,	115	,	122	,	123	,	116
100	,	116	,	123	,	124	,	117
101	,	117	,	124	,	125	,	118
102	,	118	,	125	,	126	,	119
103	,	120	,	127	,	128	,	121
104	,	121	,	128	,	129	,	122
105	,	122	,	129	,	130	,	123
106	,	123	,	130	,	131	,	124
107	,	124	,	131	,	132	,	125
108	,	125	,	132	,	133	,	126
109	,	127	,	134	,	135	,	128
110	,	128	,	135	,	136	,	129
111	,	129	,	136	,	137	,	130
112	,	130	,	137	,	138	,	131
113	,	131	,	138	,	139	,	132
114	,	132	,	139	,	140	,	133
115	,	134	,	141	,	142	,	135
116	,	135	,	142	,	143	,	136
117	,	136	,	143	,	144	,	137
118	,	137	,	144	,	145	,	138
119	,	138	,	145	,	146	,	139
120	,	139	,	146	,	147	,	140
121	,	141	,	148	,	149	,	142
122	,	142	,	149	,	150	,	143
123	,	143	,	150	,	151	,	144
124	,	144	,	151	,	152	,	145
125	,	145	,	152	,	153	,	146
126	,	146	,	153	,	154	,	147
127	,	148	,	155	,	156	,	149
128	,	149	,	156	,	157	,	150
129	,	150	,	157	,	158	,	151
130	,	151	,	158	,	159	,	152
131	,	152	,	159	,	160	,	153
132	,	153	,	160	,	161	,	154
133	,	155	,	162	,	163	,	156
134	,	156	,	163	,	164	,	157
135	,	157	,	164	,	165	,	158
136	,	158	,	165	,	166	,	159
137	,	159	,	166	,	167	,	160
138	,	160	,	167	,	168	,	161
139	,	162	,	169	,	170	,	163
140	,	163	,	170	,	171	,	164
141	,	164	,	171	,	172	,	165
142	,	165	,	172	,	173	,	166
143	,	166	,	173	,	174	,	167

```

144 ,      167 ,      174 ,      175 ,      168
145 ,      169 ,      176 ,      177 ,      170
146 ,      170 ,      177 ,      178 ,      171
147 ,      171 ,      178 ,      179 ,      172
148 ,      172 ,      179 ,      180 ,      173
149 ,      173 ,      180 ,      181 ,      174
150 ,      174 ,      181 ,      182 ,      175
*MEMBRANE SECTION,      ELSET = SHEET,      MATERIAL = AZ31
2.0 ,
*NSET, NSET=ALLNODES
1, 2, 3, 4, 5,
6, 7, 8, 9, 10
11, 12, 13, 14, 15,
16, 17, 18, 19, 20
21, 22, 23, 24, 25,
26, 27, 28, 29, 30
31, 32, 33, 34, 35,
36, 37, 38, 39, 40
41, 42, 43, 44, 45,
46, 47, 48, 49, 50
51, 52, 53, 54, 55,
56, 57, 58, 59, 60
61, 62, 63, 64, 65,
66, 67, 68, 69, 70
71, 72, 73, 74, 75,
76, 77, 78, 79, 80
81, 82, 83, 84, 85,
86, 87, 88, 89, 90
91, 92, 93, 94, 95,
96, 97, 98, 99, 100
101, 102, 103, 104, 105,
106, 107, 108, 109, 110
111, 112, 113, 114, 115,
116, 117, 118, 119, 120
121, 122, 123, 124, 125,
126, 127, 128, 129, 130
131, 132, 133, 134, 135,
136, 137, 138, 139, 140
141, 142, 143, 144, 145,
146, 147, 148, 149, 150,
151, 152, 153, 154, 155,
156, 157, 158, 159, 160,
161, 162, 163, 164, 165,
166, 167, 168, 169, 170,
171, 172, 173, 174, 175,
176, 177, 178, 179, 180,
181, 182
*NSET,      NSET=EDGENODES
1, 2, 3, 4, 5, 6, 7
*NSET,      NSET=DISPNODES

```



```

176, 177, 178, 179, 180, 181, 182
*NSET,          NSET=POLENODE
179
*NSET, NSET=MIDEDGE
4
*ELSET,          ELSET=MID
93
*NSET,          NSET=NREF
4
*ELSET,          ELSET=poleelement1
148
*SURFACE,        NAME=SHEET_SURF
SHEET,          SPOS
**
*MATERIAL,        NAME=AZ31
*ELASTIC
32281,          0.33
*CREEP,          LAW=USER
**1.8838E-8,      4.,    0.
*POTENTIAL, DEPENDENCIES=1
1.0, 1.0, 1.000, 1.000, 1.0, 1.0, 0.0, 1.0
1.0, 1.0, 1.025, 0.992, 1.0, 1.0, 0.0, 1.1
1.0, 1.0, 1.049, 0.985, 1.0, 1.0, 0.0, 1.2
1.0, 1.0, 1.072, 0.979, 1.0, 1.0, 0.0, 1.3
1.0, 1.0, 1.095, 0.973, 1.0, 1.0, 0.0, 1.4
1.0, 1.0, 1.118, 0.968, 1.0, 1.0, 0.0, 1.5
1.0, 1.0, 1.140, 0.964, 1.0, 1.0, 0.0, 1.6
1.0, 1.0, 1.162, 0.959, 1.0, 1.0, 0.0, 1.7
1.0, 1.0, 1.183, 0.956, 1.0, 1.0, 0.0, 1.8
1.0, 1.0, 1.204, 0.952, 1.0, 1.0, 0.0, 1.9
1.0, 1.0, 1.225, 0.949, 1.0, 1.0, 0.0, 2.0
1.0, 1.0, 1.245, 0.946, 1.0, 1.0, 0.0, 2.1
1.0, 1.0, 1.265, 0.943, 1.0, 1.0, 0.0, 2.2
1.0, 1.0, 1.285, 0.940, 1.0, 1.0, 0.0, 2.3
1.0, 1.0, 1.304, 0.938, 1.0, 1.0, 0.0, 2.4
*USER DEFINED FIELD
*DEPVAR
3
**-----**
**-----**
**
**-----**
**-----**
**-----**
**
** BOUNDARY CONDITIONS
**
*BOUNDARY, TYPE=DISPLACEMENT

```

```

EDGENODES, 2,
*BOUNDARY, TYPE=DISPLACEMENT
ALLNODES, 3,
*BOUNDARY, TYPE=DISPLACEMENT
MIDEDGE, 1,
**-----**
**-----**
**
** INITIAL CONDITIONS
**
**INITIAL CONDITIONS, TYPE=FIELD, VARIABLE=1
**SHEET, 1.86
**INITIAL CONDITIONS, TYPE=SOLUTION
SHEET, 0.0, 0.0, 1.86
**INITIAL CONDITIONS, TYPE=STRESS, UNBALANCED STRESS=STEP
SHEET, 0.1, 0.1
**-----**
**-----**
** STEP ANALYSIS
**-----**
**-----**
**STEP, NAME=STATIC, NLGEOM=YES, UNSYMM=YES
**STATIC
**1.E-04, 1.0,
**-----**
**BOUNDARY, TYPE=VELOCITY
**DISPNODES, 2, 2, 0.0075
**-----**
**MONITOR, DOF=3, NODE=SHEET.SHEET.4
**-----**
**OUTPUT, FIELD, FREQUENCY=1
**ELEMENT OUTPUT, ELSET=SHEET
**LE, S, STH, ER, CE
**NODE OUTPUT
**COORD, U, RF
**Output, history, FREQUENCY=1
**Node Output, NSET=POLENODE
**U1, U2, U3
**Element Output, elset=poleelement1
**STH, ER
**Node PRINT, FREQUENCY=1, nset=POLENODE
**U1, U2, U3
**EL PRINT, FREQUENCY=1, elset=poleelement1
**S, LE, ER
**EL PRINT, FREQUENCY=1, elset=poleelement1
**STH
**END STEP
**-----**
**-----**
**STEP, NAME=CREEP, NLGEOM=YES, UNSYMM=YES, INC=50000

```

```

*VISCO, CETOL=0.005
0.0005, 6500, 0.00001 , 1.0
*AMPLITUDE, NAME=velocity, DEFINITION=SMOOTH STEP
0, .0025, 250, .002563, 500, .002628, 750, .002695,
1000, .002763, 1250, .002833, 1500, .002905, 1750, .002978,
2000, .003054, 2250, .003131, 2500, .003210, 2750, .003291,
3000, .003375, 3250, .003460, 3500, .003548, 3750, .003638,
4000, .003730, 4250, .003824, 4500, .003921, 4750, .00402,
5000, .004122, 5250, .004226, 5500, .004333, 5750, .004443,
6000, .004555
*BOUNDARY, TYPE=VELOCITY, AMPLITUDE=velocity
DISPNODES, 2, 2, 1
**-----**
**MONITOR, DOF=3, NODE=SHEET.SHEET.4
**-----**
*OUTPUT, FIELD, TIME INTERVAL=60
*ELEMENT OUTPUT, ELSET=SHEET
LE, S, STH, ER, CE
*NODE OUTPUT
COORD, U, RF
*Output, history, FREQUENCY=1
*Node Output, NSET=POLENODE
U1, U2, U3
*Element Output, elset=poleelement1
S, E, ER
*NODE PRINT, FREQUENCY=1, nset=POLENODE
U1, U2, U3
*EL PRINT, FREQUENCY=1, elset=MID
S, E
*NODE PRINT, FREQUENCY=1, nset=MIDEDGE
U2
*EL PRINT, FREQUENCY=1, elset=poleelement1
S, LE, ER
*EL PRINT, FREQUENCY=1, elset=poleelement1
STH
*END STEP
**-----**
**-----**

```

EXAMPLE UNIVERSITY OF TEXAS BULGE FORMING INPUT FILE

```

*NODE
1, 40, 0
2, 37.5, 0
3, 35, 0
4, 33.75, 0
5, 32.5, 0
6, 30.8425, 0
7, 29.185, 0
8, 28.98921, -0.01283

```

9	,	28.79677143	,	-0.051111
10	,	28.61097	,	-0.11418
11	,	28.435	,	-0.200962
12	,	28.27186	,	-0.30997
13	,	28.12433983	,	-0.43934
14	,	27.99497	,	-0.58686
15	,	27.8859619	,	-0.75
16	,	27.79918	,	-0.92597
17	,	27.73611126	,	-1.111771
18	,	27.69783	,	-1.30421
19	,	27.685	,	-1.5
20	,	27.685	,	-2.75
21	,	27.685	,	-4
22	,	27.685	,	-7
23	,	27.685	,	-10
24	,	27.685	,	-15
25	,	27.685	,	-20
26	,	27.685	,	-35
27	,	27.685	,	-50
55000	,	0	,	0
55001	,	1.5	,	0
55002	,	3	,	0
55003	,	4.5	,	0
55004	,	6	,	0
55005	,	7.5	,	0
55006	,	9	,	0
55007	,	10.5	,	0
55008	,	12	,	0
55009	,	13.5	,	0
55010	,	15	,	0
55011	,	16.5	,	0
55012	,	18	,	0
55013	,	19.5	,	0
55014	,	21	,	0
55015	,	22.5	,	0
55016	,	24	,	0
55017	,	25.5	,	0
55018	,	27	,	0
55119	,	27.15	,	0
55120	,	27.3	,	0
55121	,	27.45	,	0
55122	,	27.6	,	0
55123	,	27.75	,	0
55124	,	27.9	,	0
55125	,	28.05	,	0
55126	,	28.2	,	0
55127	,	28.35	,	0
55128	,	28.5	,	0
55129	,	28.7	,	0
55130	,	28.9	,	0

55131	,	29.05	,	0	
55132	,	29.2	,	0	
55133	,	29.35	,	0	
55134	,	29.5	,	0	
55135	,	29.65	,	0	
55136	,	29.8	,	0	
55137	,	30.475	,	0	0
55138	,	30.75	,	0	
55139	,	31.575	,	0	0
55140	,	32.4	,	0	
*ELEMENT, TYPE=SAX1, ELSET=SHEET					
5000	,	55000	,	55001	
5001	,	55001	,	55002	
5002	,	55002	,	55003	
5003	,	55003	,	55004	
5004	,	55004	,	55005	
5005	,	55005	,	55006	
5006	,	55006	,	55007	
5007	,	55007	,	55008	
5008	,	55008	,	55009	
5009	,	55009	,	55010	
5010	,	55010	,	55011	
5011	,	55011	,	55012	
5012	,	55012	,	55013	
5013	,	55013	,	55014	
5014	,	55014	,	55015	
5015	,	55015	,	55016	
5016	,	55016	,	55017	
5017	,	55017	,	55018	
5018	,	55018	,	55119	
5119	,	55119	,	55120	
5120	,	55120	,	55121	
5121	,	55121	,	55122	
5122	,	55122	,	55123	
5123	,	55123	,	55124	
5124	,	55124	,	55125	
5125	,	55125	,	55126	
5126	,	55126	,	55127	
5127	,	55127	,	55128	
5128	,	55128	,	55129	
5129	,	55129	,	55130	
5130	,	55130	,	55131	
5131	,	55131	,	55132	
5132	,	55132	,	55133	
5133	,	55133	,	55134	
5134	,	55134	,	55135	
5135	,	55135	,	55136	
5136	,	55136	,	55137	
5137	,	55137	,	55138	
5138	,	55138	,	55139	

```

5139 ,      55139 ,      55140
*ELEMENT,   TYPE=SAX1, ELSET=DIE
1001 ,      27      ,      26
1002 ,      26      ,      25
1003 ,      25      ,      24
1004 ,      24      ,      23
1005 ,      23      ,      22
1006 ,      22      ,      21
1007 ,      21      ,      20
1008 ,      20      ,      19
1009 ,      19      ,      18
1010 ,      18      ,      17
1011 ,      17      ,      16
1012 ,      16      ,      15
1013 ,      15      ,      14
1014 ,      14      ,      13
1015 ,      13      ,      12
1016 ,      12      ,      11
1017 ,      11      ,      10
1018 ,      10      ,      9
1019 ,      9       ,      8
1020 ,      8       ,      7
1021 ,      7       ,      6
1022 ,      6       ,      5
1023 ,      5       ,      4
1024 ,      4       ,      3
1025 ,      3       ,      2
1026 ,      2       ,      1
*SHELL SECTION, ELSET = SHEET, MATERIAL = AZ31
2.0 ,
*SHELL SECTION, ELSET = DIE, MATERIAL = AZ31
2.0 ,
*RIGID BODY, REF NODE = NREF, ELSET = DIE
*NSET, NSET=EDGENODES
55140
*NSET, NSET=POLENODE
55000
*NSET, NSET=NREF
3
*ELSET, ELSET=poleelement1
5000
*SURFACE, TYPE=ELEMENT, NAME=DIE_SURF
DIE, SPOS
*SURFACE, NAME=SHEET_SURF
SHEET, SPOS
**
*MATERIAL, NAME=AZ31
*ELASTIC
32281, 0.33
*CREEP, LAW=USER

```

```

**1.8838E-8,      4.,    0.
*POTENTIAL, DEPENDENCIES=1
1.0, 1.0, 1.000, 1.000, 1.0, 1.0, 0.0, 1.0
1.0, 1.0, 1.025, 0.992, 1.0, 1.0, 0.0, 1.1
1.0, 1.0, 1.049, 0.985, 1.0, 1.0, 0.0, 1.2
1.0, 1.0, 1.072, 0.979, 1.0, 1.0, 0.0, 1.3
1.0, 1.0, 1.095, 0.973, 1.0, 1.0, 0.0, 1.4
1.0, 1.0, 1.118, 0.968, 1.0, 1.0, 0.0, 1.5
1.0, 1.0, 1.140, 0.964, 1.0, 1.0, 0.0, 1.6
1.0, 1.0, 1.162, 0.959, 1.0, 1.0, 0.0, 1.7
1.0, 1.0, 1.183, 0.956, 1.0, 1.0, 0.0, 1.8
1.0, 1.0, 1.204, 0.952, 1.0, 1.0, 0.0, 1.9
1.0, 1.0, 1.225, 0.949, 1.0, 1.0, 0.0, 2.0
1.0, 1.0, 1.245, 0.946, 1.0, 1.0, 0.0, 2.1
1.0, 1.0, 1.265, 0.943, 1.0, 1.0, 0.0, 2.2
1.0, 1.0, 1.285, 0.940, 1.0, 1.0, 0.0, 2.3
1.0, 1.0, 1.304, 0.938, 1.0, 1.0, 0.0, 2.4
*USER DEFINED FIELD
*DEPVAR
3
**-----**
**-----**
**
** INTERACTION PROPERTIES
**
*CONTACT PAIR, INTERACTION=DIE_CONT, SMOOTH=0.2
SHEET_SURF, DIE_SURF
*SURFACE INTERACTION, NAME=DIE_CONT
**-----**
**-----**
**-----**
**
** BOUNDARY CONDITIONS
**
*BOUNDARY, TYPE=DISPLACEMENT
NREF,      1, 6,
EDGENODES, 1, 2
POLENODE,  1
**-----**
**-----**
**
** INITIAL CONDITIONS
**
**INITIAL CONDITIONS, TYPE=FIELD, VARIABLE=1
**SHEET, 1.86
*INITIAL CONDITIONS, TYPE=SOLUTION
SHEET, 0.0, 0.0, 1.86
*INITIAL CONDITIONS, TYPE=STRESS, UNBALANCED STRESS=STEP
SHEET, 0.1, 0.1
**-----**

```

```

**-----**
** STEP ANALYSIS
**-----**
**-----**
*STEP, NAME=STATIC,NLGEOM=YES,UNSYMM=NO
*STATIC
1.E-04,1.0,
**-----**
*DLOAD
SHEET, P, -0.827371
**SHEET, P, 0.827371
**-----**
**MONITOR,DOF=3,NODE=SHEET.SHEET.4
**-----**
*OUTPUT,FIELD,FREQUENCY=4
*ELEMENT OUTPUT,ELSET=SHEET
LE,S,STH,ER,CE
*NODE OUTPUT
COORD, U, RF
*Output, history,FREQUENCY=1
*Node Output, NSET=POLENODE
U1,U2,U3
*Element Output, elset=poleelement1
STH, ER
*Node PRINT,FREQUENCY=1,nset=POLENODE
U2
*EL PRINT,FREQUENCY=1,elset=poleelement1
S, LE, ER
*EL PRINT,FREQUENCY=1,elset=poleelement1
STH
*END STEP
**-----**
**-----**
*STEP, NAME=CREEP,NLGEOM=YES,UNSYMM=NO,INC=50000
*VISCO, CETOL=0.005
0.00005, 10000.0, 0.0000001 , 2.0
**DLOAD
**SHEET, P, -0.28958
**SHEET, P, 0.28958
**-----**
**MONITOR,DOF=3,NODE=SHEET.SHEET.4
**-----**
*OUTPUT,FIELD,TIME INTERVAL=2
*ELEMENT OUTPUT,ELSET=SHEET
LE,S,STH,ER,CE
*NODE OUTPUT
COORD, U, RF
*Output, history,FREQUENCY=3
*Node Output, NSET=POLENODE
U1,U2,U3

```



```

*Element Output,elset=poleelement1
STH, ER
*NODE PRINT,FREQUENCY=3,nset=POLENODE
U2
*EL PRINT,FREQUENCY=3,elset=poleelement1
S, LE, ER
*EL PRINT,FREQUENCY=3,elset=poleelement1
STH
*END STEP
**-----**

```

EXAMPLE GENERAL MOTORS BULGE FORMING INPUT FILE

```

*NODE
1      ,      70      ,      0
2      ,      68      ,      0
3      ,      66      ,      0
4      ,      64      ,      0
5      ,      62      ,      0
6      ,      60      ,      0
7      ,      58      ,      0
8      ,      56      ,      0
9      ,      55      ,      0
59     ,      54.7819  ,      -0.00476
60     ,      54.56422 ,      -0.01903
61     ,      54.34737 ,      -0.04278
62     ,      54.13176 ,      -0.07596
63     ,      53.9178  ,      -0.11852
64     ,      53.7059  ,      -0.17037
65     ,      53.49647 ,      -0.23142
66     ,      53.2899  ,      -0.30154
67     ,      53.08658 ,      -0.3806
68     ,      52.88691 ,      -0.46846
69     ,      52.69126 ,      -0.56495
70     ,      52.5     ,      -0.66987
71     ,      52.3135  ,      -0.78304
72     ,      52.13212 ,      -0.90424
73     ,      51.95619 ,      -1.03323
74     ,      51.78606 ,      -1.16978
75     ,      51.62205 ,      -1.31361
76     ,      51.46447 ,      -1.46447
77     ,      51.31361 ,      -1.62205
78     ,      51.16978 ,      -1.78606
79     ,      51.03323 ,      -1.95619
80     ,      50.90424 ,      -2.13212
81     ,      50.78304 ,      -2.3135
82     ,      50.66987 ,      -2.5
83     ,      50.56495 ,      -2.69126
84     ,      50.46846 ,      -2.88691
85     ,      50.3806  ,      -3.08658

```

86	,	50.30154	,	-3.2899
87	,	50.23142	,	-3.49647
88	,	50.17037	,	-3.7059
89	,	50.11852	,	-3.9178
90	,	50.07596	,	-4.13176
91	,	50.04278	,	-4.34737
92	,	50.01903	,	-4.56422
93	,	50.00476	,	-4.7819
94	,	50	,	-5
95	,	50	,	-6
96	,	50	,	-7
97	,	50	,	-8
98	,	50	,	-10
99	,	50	,	-15
100	,	50	,	-20
101	,	50	,	-30
102	,	50	,	-40
103	,	50	,	-50
104	,	50	,	-60
55000	,	0	,	0
55001	,	1.5	,	0
55002	,	3	,	0
55003	,	4.5	,	0
55004	,	6	,	0
55005	,	7.5	,	0
55006	,	9	,	0
55007	,	10.5	,	0
55008	,	12	,	0
55009	,	13.5	,	0
55010	,	15	,	0
55011	,	16.5	,	0
55012	,	18	,	0
55013	,	19.5	,	0
55014	,	21	,	0
55015	,	22.5	,	0
55016	,	24	,	0
55017	,	25.5	,	0
55018	,	27	,	0
55019	,	28.5	,	0
55020	,	30	,	0
55021	,	31.5	,	0
55022	,	33	,	0
55023	,	34.5	,	0
55024	,	36	,	0
55025	,	37.5	,	0
55026	,	39	,	0
55027	,	40.5	,	0
55028	,	42	,	0
55029	,	43.5	,	0
55030	,	45	,	0

55131 ,	45.2	,	0
55132 ,	45.4	,	0
55133 ,	45.6	,	0
55134 ,	45.8	,	0
55135 ,	46	,	0
55136 ,	46.2	,	0
55137 ,	46.4	,	0
55138 ,	46.6	,	0
55139 ,	46.8	,	0
55140 ,	47	,	0
55141 ,	47.2	,	0
55142 ,	47.4	,	0
55143 ,	47.6	,	0
55144 ,	47.8	,	0
55145 ,	48	,	0
55146 ,	48.2	,	0
55147 ,	48.4	,	0
55148 ,	48.6	,	0
55149 ,	48.8	,	0
55150 ,	49	,	0
55151 ,	49.2	,	0
55152 ,	49.4	,	0
55153 ,	49.6	,	0
55154 ,	49.8	,	0
55155 ,	50	,	0
55156 ,	50.2	,	0
55157 ,	50.4	,	0
55158 ,	50.6	,	0
55159 ,	50.8	,	0
55160 ,	51	,	0
55161 ,	51.2	,	0
55162 ,	51.4	,	0
55163 ,	51.6	,	0
55164 ,	51.8	,	0
55165 ,	52	,	0
55166 ,	52.2	,	0
55167 ,	52.4	,	0
55168 ,	52.6	,	0
55169 ,	52.8	,	0
55170 ,	53	,	0
55171 ,	53.2	,	0
55172 ,	53.4	,	0
55173 ,	53.6	,	0
55174 ,	53.8	,	0
55175 ,	54	,	0
55176 ,	54.2	,	0
55177 ,	54.4	,	0
55178 ,	54.6	,	0
55179 ,	54.8	,	0
55180 ,	55	,	0

55181	,	56	,	0
55182	,	58	,	0
55183	,	60	,	0
55184	,	62	,	0
55185	,	64	,	0
55186	,	66	,	0
*ELEMENT,		TYPE=SAX1,		ELSET=SHEET
5000	,	55000	,	55001
5001	,	55001	,	55002
5002	,	55002	,	55003
5003	,	55003	,	55004
5004	,	55004	,	55005
5005	,	55005	,	55006
5006	,	55006	,	55007
5007	,	55007	,	55008
5008	,	55008	,	55009
5009	,	55009	,	55010
5010	,	55010	,	55011
5011	,	55011	,	55012
5012	,	55012	,	55013
5013	,	55013	,	55014
5014	,	55014	,	55015
5015	,	55015	,	55016
5016	,	55016	,	55017
5017	,	55017	,	55018
5018	,	55018	,	55019
5019	,	55019	,	55020
5020	,	55020	,	55021
5021	,	55021	,	55022
5022	,	55022	,	55023
5023	,	55023	,	55024
5024	,	55024	,	55025
5025	,	55025	,	55026
5026	,	55026	,	55027
5027	,	55027	,	55028
5028	,	55028	,	55029
5029	,	55029	,	55030
5030	,	55030	,	55131
5131	,	55131	,	55132
5132	,	55132	,	55133
5133	,	55133	,	55134
5134	,	55134	,	55135
5135	,	55135	,	55136
5136	,	55136	,	55137
5137	,	55137	,	55138
5138	,	55138	,	55139
5139	,	55139	,	55140
5140	,	55140	,	55141
5141	,	55141	,	55142
5142	,	55142	,	55143

5143	,	55143	,	55144
5144	,	55144	,	55145
5145	,	55145	,	55146
5146	,	55146	,	55147
5147	,	55147	,	55148
5148	,	55148	,	55149
5149	,	55149	,	55150
5150	,	55150	,	55151
5151	,	55151	,	55152
5152	,	55152	,	55153
5153	,	55153	,	55154
5154	,	55154	,	55155
5155	,	55155	,	55156
5156	,	55156	,	55157
5157	,	55157	,	55158
5158	,	55158	,	55159
5159	,	55159	,	55160
5160	,	55160	,	55161
5161	,	55161	,	55162
5162	,	55162	,	55163
5163	,	55163	,	55164
5164	,	55164	,	55165
5165	,	55165	,	55166
5166	,	55166	,	55167
5167	,	55167	,	55168
5168	,	55168	,	55169
5169	,	55169	,	55170
5170	,	55170	,	55171
5171	,	55171	,	55172
5172	,	55172	,	55173
5173	,	55173	,	55174
5174	,	55174	,	55175
5175	,	55175	,	55176
5176	,	55176	,	55177
5177	,	55177	,	55178
5178	,	55178	,	55179
5179	,	55179	,	55180
5180	,	55180	,	55181
5181	,	55181	,	55182
5182	,	55182	,	55183
5183	,	55183	,	55184
5184	,	55184	,	55185
5185	,	55185	,	55186
*ELEMENT, TYPE=SAX1, ELSET=DIE				
1001	,	104	,	103
1002	,	103	,	102
1003	,	102	,	101
1004	,	101	,	100
1005	,	100	,	99
1006	,	99	,	98

1007	,	98	,	97
1008	,	97	,	96
1009	,	96	,	95
1010	,	95	,	94
1011	,	94	,	93
1012	,	93	,	92
1013	,	92	,	91
1014	,	91	,	90
1015	,	90	,	89
1016	,	89	,	88
1017	,	88	,	87
1018	,	87	,	86
1019	,	86	,	85
1020	,	85	,	84
1021	,	84	,	83
1022	,	83	,	82
1023	,	82	,	81
1024	,	81	,	80
1025	,	80	,	79
1026	,	79	,	78
1027	,	78	,	77
1028	,	77	,	76
1029	,	76	,	75
1030	,	75	,	74
1031	,	74	,	73
1032	,	73	,	72
1033	,	72	,	71
1034	,	71	,	70
1035	,	70	,	69
1036	,	69	,	68
1037	,	68	,	67
1038	,	67	,	66
1039	,	66	,	65
1040	,	65	,	64
1041	,	64	,	63
1042	,	63	,	62
1043	,	62	,	61
1044	,	61	,	60
1045	,	60	,	59
1095	,	59	,	9
1096	,	9	,	8
1097	,	8	,	7
1098	,	7	,	6
1099	,	6	,	5
1100	,	5	,	4
1101	,	4	,	3
1102	,	3	,	2
1103	,	2	,	1

*SHELL SECTION, ELSET = SHEET, MATERIAL = AZ31
2.0 ,

```

*SHELL SECTION,      ELSET = DIE,      MATERIAL = AZ31
2.0 ,
*RIGID BODY,          REF NODE = NREF, ELSET = DIE
*NSET,                NSET=EDGENODES
55186
*NSET,                NSET=POLENODE
55000
*NSET,                NSET=NREF
3
*ELSET,              ELSET=poleelement1
5000
*SURFACE,            TYPE=ELEMENT,      NAME=DIE_SURF
DIE, SPOS
*SURFACE,            NAME=SHEET_SURF
SHEET, SPOS
**
*MATERIAL,           NAME=AZ31
*ELASTIC
32281,              0.33
*CREEP,              LAW=USER
**1.8838E-8,         4., 0.
*POTENTIAL, DEPENDENCIES=1
1.0, 1.0, 1.000, 1.000, 1.0, 1.0, 0.0, 1.0
1.0, 1.0, 1.025, 0.992, 1.0, 1.0, 0.0, 1.1
1.0, 1.0, 1.049, 0.985, 1.0, 1.0, 0.0, 1.2
1.0, 1.0, 1.072, 0.979, 1.0, 1.0, 0.0, 1.3
1.0, 1.0, 1.095, 0.973, 1.0, 1.0, 0.0, 1.4
1.0, 1.0, 1.118, 0.968, 1.0, 1.0, 0.0, 1.5
1.0, 1.0, 1.140, 0.964, 1.0, 1.0, 0.0, 1.6
1.0, 1.0, 1.162, 0.959, 1.0, 1.0, 0.0, 1.7
1.0, 1.0, 1.183, 0.956, 1.0, 1.0, 0.0, 1.8
1.0, 1.0, 1.204, 0.952, 1.0, 1.0, 0.0, 1.9
1.0, 1.0, 1.225, 0.949, 1.0, 1.0, 0.0, 2.0
1.0, 1.0, 1.245, 0.946, 1.0, 1.0, 0.0, 2.1
1.0, 1.0, 1.265, 0.943, 1.0, 1.0, 0.0, 2.2
1.0, 1.0, 1.285, 0.940, 1.0, 1.0, 0.0, 2.3
1.0, 1.0, 1.304, 0.938, 1.0, 1.0, 0.0, 2.4
*USER DEFINED FIELD
*DEPVAR
3
**-----**
**-----**
**
** INTERACTION PROPERTIES
**
*CONTACT PAIR, INTERACTION=DIE_CONT,SMOOTH=0.2
SHEET_SURF, DIE_SURF
*SURFACE INTERACTION, NAME=DIE_CONT
**-----**
**-----**

```

```

**-----**
**
** BOUNDARY CONDITIONS
**
*BOUNDARY,TYPE=DISPLACEMENT
NREF,      1,  6,
EDGENODES,  1,  2
POLENODE,   1
**-----**
**-----**
**
** INITIAL CONDITIONS
**
**INITIAL CONDITIONS, TYPE=FIELD, VARIABLE=1
**SHEET, 1.86
*INITIAL CONDITIONS, TYPE=SOLUTION
SHEET, 0.0, 0.0, 1.86
*INITIAL CONDITIONS, TYPE=STRESS, UNBALANCED STRESS=STEP
SHEET, 0.1, 0.1
**-----**
**-----**
** STEP ANALYSIS
**-----**
**-----**
*STEP, NAME=STATIC,NLGEOM=YES,UNSYMM=NO
*STATIC
1.E-05,1.0,1.E-8
**-----**
*DLOAD
SHEET, P, -0.517107
**SHEET, P, 0.827371
**-----**
**MONITOR,DOF=3,NODE=SHEET.SHEET.4
**-----**
*OUTPUT,FIELD,FREQUENCY=4
*ELEMENT OUTPUT,ELSET=SHEET
LE,S,STH,ER,CE
*NODE OUTPUT
COORD, U, RF
*Output, history,FREQUENCY=1
*Node Output, NSET=POLENODE
U1,U2,U3
*Element Output, elset=poleelement1
STH, ER
*Node PRINT,FREQUENCY=1,nset=POLENODE
U2
*EL PRINT,FREQUENCY=1,elset=poleelement1
S, LE, ER
*EL PRINT,FREQUENCY=1,elset=poleelement1
STH

```



```

*END STEP
**-----**
**-----**
*STEP, NAME=CREEP,NLGEOM=YES,UNSYMM=NO,INC=50000
*VISCO, CETOL=0.005
0.000005, 10000.0, 0.00000001 , 2.0
**DLOAD
**SHEET, P, -0.28958
**SHEET, P, 0.28958
**-----**
**MONITOR,DOF=3,NODE=SHEET.SHEET.4
**-----**
*OUTPUT, FIELD, TIME INTERVAL=2
*ELEMENT OUTPUT, ELSET=SHEET
LE, S, STH, ER, CE
*NODE OUTPUT
COORD, U, RF
*Output, history, FREQUENCY=3
*Node Output, NSET=POLENODE
U1, U2, U3
*Element Output, elset=poleelement1
STH, ER
*NODE PRINT, FREQUENCY=3, nset=POLENODE
U2
*EL PRINT, FREQUENCY=3, elset=poleelement1
S, LE, ER
*EL PRINT, FREQUENCY=3, elset=poleelement1
STH
*END STEP
**-----**

```

References

1. L.H. Pomeroy: *Automotive Engineering*, 1922, vol. XI, no. 6, pp. 508-519.
2. G.S. Cole, A.M. Sherman: *Mater. Char.*, 1995, vol. 35, pp. 3-9.
3. J.J. Lee, S.P. Lukachko, I.A. Waitz, A. Schafer: *Annual Review of Energy and the Environment*, 2001, vol. 26, pp. 167-200.
4. A.I. Taub: *MRS Bulletin*, 2006, vol. 31, pp. 336-343.
5. A.I. Taub, P.E. Krajewski, A.A. Luo, J.N. Owens: *JOM*, 2007, vol. 59, no. 2, pp. 48-57.
6. D. Eliezer, E. Aghion, F.H. Froes: *Adv. Perform Mater.*, 1998, vol. 5, pp. 201-212.
7. M.M. Avedesian, H. Baker: *Magnesium and Magnesium Alloys*, Materials Park: ASM International, 1999, pg. iv.
8. E. Aghion, B. Bronfin, D. Eliezer: *J. Mater. Process. Tech.*, 2001, vol. 117, pp. 381-385.
9. B.L. Mordike, T. Ebert: *Mater. Sci. Eng. A*, 2001, vol. 302, pp. 37-45.
10. M. Easton, A. Beer, M. Barnett, C. Davies, G. Dunlop, Y. Durandet, S. Blacket, T. Hilditch, P. Beggs: *JOM*, 2008, vol. 60, no. 11, pp. 57-62.
11. M.K. Kulekci: *Int. J. Adv. Manuf. Technol.*, 2008, vol. 39, pp. 851-865.
12. I.J. Polmear: *Mater. Sci. Tech.*, 1994, vol. 10, pp. 1-16.
13. M.W. Toaz, E.J. Ripling: *J. Met.*, 1956, vol. 8, pp. 936-946.

14. P.E. Krajewski: in *Magnesium Technology*, H.I. Kaplan, ed., TMS, Warrendale, PA, 2002, pp. 169-174.
15. R. Verma, L.G. Hector, Jr., P.E. Krajewski, E.M. Taleff: *JOM*, 2009, vol. 61, no. 8, pp. 29-37.
16. ASM: *Metals Handbook, Vol. 20*, Materials Park, OH, 2002.
17. A.A. Luo: *JOM*, 2002, vol. 54, no. 2, pp. 42-48.
18. T. Nakagawa: *Annals of the CIRP*, 1993, vol. 42, no. 2, pp. 717-22.
19. H. Hayashi, T. Nakagawa: *J. Mater. Process. Tech.*, 1994, vol. 46, pp. 455-87.
20. G.B. Burger, A.K. Gupta, P.W. Jeffrey, D.J. Lloyd: *Mater. Charact.*, 1995, vol. 35, pp. 23-39.
21. R. Smerd, S. Winkler, C. Salisbury, M. Worswick, D. Lloyd, M. Finn: *Int. J. Impact Eng.*, 2005, vol. 32, pp. 541-60.
22. G.I. Taylor: *J. Inst. Metals*, 1938, vol. 62, pp. 307-24.
23. P.A. Sherek: "Simulation and Experimental Investigation of Hot Gas-Pressure Forming for Light-Alloy Sheet Material," Thesis, Mechanical Engineering, The University of Texas at Austin, 2009.
24. R.E. Reed-Hill, W.D. Robertson: *Acta Metall.*, 1957, vol. 5, pp. 728-737.
25. P.W. Flynn, J. Mote, J.E. Dorn: *Transactions of the Metallurgical Society of AIME*, 1961, vol. 221, pp. 1148-54.
26. H. Yoshinaga, R. Horiuchi: *Trans. Japan Inst. Metals*, 1963, vol. 4, pp. 1-8.
27. T. Obara, H. Yoshinga, S. Morozumi: *Acta Metall.*, 1973, vol. 21, pp. 845-53.

28. M.H. Yoo, J.R. Morris, K.M. Ho, S.R. Agnew: *Metall. Mater. Trans. A*, 2002, vol. 33, pp. 813-22.
29. M.R. Barnett: *Metall. Mater. Trans. A*, 2003, vol. 34, pp. 1799-1805.
30. J.A. Yasi, L.G. Hector, Jr., D.R. Trinkle: *Acta Mater.*, 2011, vol. 59, pp. 5652-60.
31. G.C. Cornfield, R.H. Johnson: *Int. J. Mech. Sci.*, 1970, vol. 12, pp. 479-90.
32. A.K. Ghosh, C.H. Hamilton: *Metall. Trans. A*, 1982, vol. 13, pp. 733-43.
33. F.I. Saunders, P.E. Krajewski, E.F. Ryntz, J.G. Schroth: *U.S. Patent 5974847*, 1999.
34. A.J. Barnes: *J. Mater. Eng. Perform.*, 2007, vol. 16, pp. 440-54.
35. M.S. Rashid, C. Kim, E.F. Ryntz, F.I. Saunders, R. Verma, S. Kim: *U.S. Patent 6253588*, 2001.
36. J.G. Schroth: in *Advances in Superplasticity and Superplastic Forming*, E.M. Taleff, P.A. Friedman, P.E. Krajewski, R.S. Mishra, J.G. Schroth, eds., TMS, Warrendale, PA, 2004, pp. 9-20.
37. P.E. Krajewski, J.G. Schroth: *Mater. Sci. Forum*, 2007, vol. 551-552, pp. 3-12.
38. M.-A. Kulas, W.P. Green, E.M. Taleff, P.E. Krajewski, T.R. McNelley: *Metall. Mater. Trans. A*, 2005, vol. 36, pp. 1240-61.
39. J.-K. Chang, E.M. Taleff, P.E. Krajewski: *Metall. Mater. Trans. A*, 2009, vol. 40, pp. 3128-37.
40. R. Panicker, A.H. Chokshi, R.K. Mishra, R. Verma, P.E. Krajewski: *Acta Mater.*, 2009, vol. 57, pp. 3683-93.

41. E.M. Taleff, L.G. Hector, Jr., R. Verma, P.E. Krajewski, J.-K. Chang: *J. Mater. Eng. Perform.*, 2010, vol. 19, pp. 488-94.
42. P.A. Sherek, A.J. Carpenter, L.G. Hector, Jr., P.E. Krajewski, J.T. Carter, J. Lasceski, E.M. Taleff: in *Magnesium Technology 2012*, S.N. Mathaudhu, ed., 2012, TMS, Warrendale, PA, in press.
43. H.-K. Kim, W.-J. Kim: *J. Mater. Sci.*, 2007, vol. 42, pp. 6171-76.
44. I.A. Maksoud, H. Ahmed, J. Rödel: *Mater. Sci. Eng. A*, 2009, vol. 504, pp. 40-48.
45. S. Spigarelli, M. El Mehtedi: *Mater. Sci. Eng. A*, 2010, vol. 527, pp. 5708-14.
46. C. Bruni, L. Donati, M. El Mehtedi, M. Simoncini: *Key Eng. Mater.*, 2008, vol. 367, pp. 87-94.
47. K.E. Tello, A.P. Gerlich, P.F. Mendez: *Sci. Technol. Weld. Joi.*, 2010, vol. 15, no. 3, pp. 260-66.
48. M.K. Khraisheh, F.K. Abu-Farha, M.A. Nazzal, K.J. Weinmann: *Annals of the CIRP*, 2006, vol. 55, no. 1, pp. 233-36.
49. F.K. Abu-Farha, M.K. Khraisheh: *Adv. Eng. Mater.*, 2007, vol. 9, no. 9, pp. 777-83.
50. F.K. Abu-Farha: "Integrated Approach to the Superplastic Forming of Magnesium Alloys," Dissertation, Engineering, The University of Kentucky, 2007.
51. F.K. Abu-Farha, N.A. Rawashdeh, M.K. Khraisheh: *Mater. Sci. Forum*, 2007, vols. 551-552, pp. 219-24.

52. F.K. Abu-Farha, M.K. Khraisheh: *J. Mater. Eng. Perform.*, 2007, vol. 16, pp. 192-99.
53. G. Palumbo, D. Sorgente, L. Tricarico, S.H. Zhang, W.T. Zheng, L.X. Zhou, L.M. Ren: *Mater. Sci. Forum*, 2007, vol. 551-552, pp. 317-22.
54. A.-W. El-Morsy, K. Manabe, H. Nishimura: *Mater. Trans.*, 2002, vol. 43, pp. 2443-48.
55. G. Giuliano, S. Franchitti: *Int. J. Mach. Tool Manu.*, 2008, vol. 48, pp. 1519-22.
56. O.D. Sherby, P.M. Burke: *Progr. Mater. Sci.*, 1968, vol. 13, pp. 325-90.
57. T.G. Nieh, J. Wadsworth and O.D. Sherby: *Superplasticity in Metals and Ceramics*, Cambridge: Cambridge University Press, 1997, pp. 43-72.
58. Dassault Systèmes: Abaqus FEA 6.10, Vélizy-Villacoublay, France, 2010.
59. ASM International: *Metals Handbook, Vol. 2*, Materials Park, OH, 2002.
60. R.R. Craig, Jr.: *Mechanics of Materials*, 3rd ed., Hoboken: John Wiley & Sons, 2011, pp. 37-45.
61. W. Köster: *Z. Metallkd.*, 1948, vol. 39, pp. 1-9.
62. H. Watanabe, T. Mukai, M. Sugioka, K. Ishikawa: *Scr. Mater.*, 2004, vol. 51, pp. 291-295.
63. C. Dotson, R. Harlow, R.L. Thompson: *Fundamentals of Dimensional Metrology*, Albany: Thomson Learning, 2003, p. 141.
64. J. Hu, Z. Marciniak, J. Duncan: *Mechanics of Sheet Metal Forming*, Oxford: Butterworth-Heinemann, Jordan Hill, 2002, pp. 8-11.

65. ASTM International: *E517-00 – Standard Test Method for Plastic Strain Ratio r for Sheet Metal*, West Conshohocken, 2000.
66. R.S. Figliola, D.E. Beasley: *Theory and Design for Mechanical Measurements*, 2nd ed., New York: John Wiley & Sons, 1995, pp. 177-182.
67. W. Rasband: ImageJ, Bethesda: National Institutes of Health, 2011.
68. ASTM International: *E112-96 - Standard Test Methods for Determining Average Grain Size*, West Conshohocken, 1996.
69. R.V. Moller: “Design and Fabrication of an Instrument to Test the Mechanical Behavior of Aluminum Alloy Sheets during High-Temperature Gas-Pressure Blow Forming,” Thesis, Mechanical Engineering, The University of Texas at Austin, 2008.
70. F.J. Humphreys, M. Hatherly: *Recrystallization and Related Annealing Phenomena*, Oxford: Elsevier, 2004, pp. 134-135.
71. J. Burke, D. Turnbull: *Prog. Metal Phys.*, 1952, vol. 3, pp. 220-292.
72. F.J. Humphreys, M. Hatherly: *Recrystallization and Related Annealing Phenomena*, Oxford: Elsevier, 2004, pp. 335-336.
73. D.S. Wilkinson, C.H. Cáceres: *Acta Metall.*, 1984, vol. 32, pp. 1335-1345.
74. D.S. Wilkinson, C.H. Cáceres: *J. Mater. Sci. Lett.*, 1984, vol. 3, pp. 395-399.
75. J.R. Seidensticker, M.J. Mayo: *Scr. Mater.*, 1998, vol. 38, pp. 1091-1100.
76. E. Sato, K. Kuribayashi, R. Horiuchi: *J. Japan. Inst. Metals*, 1988, vol. 52, pp. 1043-1050.

77. B.-N. Kim, K. Hiraga, Y. Sakka, B.-W. Ahn: *Acta Mater.*, 1999, vol. 47, pp. 3433-3439.
78. Wolfram Research, Inc.: *Mathematica 8*, Champaign, IL, 2011.
79. E. Voce: *Metallurgica*, 1955, vol. 51, pp. 219-220.
80. M.R. Barnett, A. Ghaderi, I. Sabirov, B. Hutchinson: *Scr. Mater.*, 2009, vol. 61, pp. 277-280.
81. R. von Mises: *Nachr. Math. Phys.*, 1913, vol. 1, pp. 582-592.
82. R. Hill: *The Mathematical Theory of Plasticity*, New York: Oxford University Press, 1950.
83. F. Barlat, J. Lian: *Int. J. Plasticity*, 1989, vol. 5, pp. 51-66.
84. B. Plunkett, O. Cazacu, R.A. Levensohn, F. Barlat: *Acta Mater.*, 2006, vol. 54, pp. 4159-4169.
85. B. Plunkett, O. Cazacu, F. Barlat: *Int. J. Plasticity*, 2008, vol. 24, pp. 847-866.
86. R.R. Craig, Jr.: *Mechanics of Materials*, 3rd ed., Hoboken: John Wiley & Sons, 2011, pp. 542-544.
87. Dassault Systèmes: *Abaqus Analysis User's Manual*, Vélizy-Villacoublay, France, 2010, retrieved from <https://www.sharcnet.ca/Software/Abaqus610/Documentation/docs/v6.10/books/usb/default.htm> on April 5, 2012.
88. F. Dunne, N. Petrinic: *Introduction to Computational Plasticity*, New York: Oxford University Press, 2005, pp. 38-42.
89. H. Yoshinaga, R. Horiuchi: *Trans. Japan Inst. Metals*, 1963, vol. 5, pp. 14-21.

90. E. Yukutake, J. Kaneko, M. Sugamata: *Mater. Trans.*, 2003, vol. 44, no. 4, pp. 452-457.
91. M.R. Barnett, M.D. Nave, C.J. Bettles: *Mater. Sci. Eng. A*, 2004, vol. 386, pp. 205-211.
92. S.R. Agnew, Ö Duygulu: *Int. J. Plasticity*, 2005, vol. 21, pp. 1161-93.
93. J.A. Del Valle, M.T. Pérez-Prado, O.A. Ruano: *Metall. Mater. Trans. A*, 2005, vol. 36, pp. 1427-38.
94. J.W. Backus: FORTRAN 77, Armonk: IBM, 1978.
95. A.J. Carpenter: "The Effects of Processing Conditions on Static Abnormal Grain Growth in Al-Mg Alloy AA5182," Thesis, Mechanical Engineering, The University of Texas at Austin, 2011.
96. J. R Bradley and J. E. Carsley: in *Advances in Superplasticity and Superplastic Forming*, E. M. Taleff, P.A. Friedman, P. E. Krajewski, R. S. Mishra, and J.G. Schroth, eds., 2004, TMS, Warrendale, PA, pp. 149-157

Vita

Alexander James Carpenter was born in Anchorage, AK on December 13, 1985. After living in Alaska (twice), Ohio, and Pennsylvania, his family moved to Texas, where he graduated from Leander High School ranked 3rd in his graduating class in May 2004. After high school, he enrolled at The University of Texas at Austin, where he majored in Mechanical Engineering

After obtaining a Bachelor of Science degree in Mechanical Engineering in May 2008, he enrolled at the Graduate School at The University of Texas at Austin. As a graduate student, he assisted in teaching a materials processing lab class and obtained a Master of Science in Engineering degree. His master's thesis is a study of static abnormal grain growth after the high-temperature deformation of aluminum AA5182 sheet. During the summer of 2010, he interned at the General Motors Technical Center in Warren, MI, where he studied the hot gas-pressure forming of magnesium sheet. He plans to work in industry after graduation.

Permanent address: 827 Celosia

San Antonio, TX 78245

This dissertation was typed by the author.